

<https://doi.org/10.15388/vu.thesis.118>

<https://orcid.org/0000-0002-3093-6673>

VILNIUS UNIVERSITY

CENTER FOR NATURAL SCIENCES AND TECHNOLOGY

Ignas

STASEVIČIUS

# Cascaded Nonlinearity Influence to Femtosecond Optical Parametric Oscillator Characteristics

**DOCTORAL DISSERTATION**

Natural Sciences,

Physics (N 002)

---

VILNIUS 2020

This dissertation was written between 2015 and 2020 at Vilnius University, Laser Research Center.

The research was supported by MITA and Research Council of Lithuania.

**Academic supervisor:**

**Prof. Dr. Mikas Vengris** (Vilnius University, Natural Sciences, Physics, N 002).

<https://doi.org/10.15388/vu.thesis.118>

<https://orcid.org/0000-0002-3093-6673>

VILNIAUS UNIVERSITETAS

FIZINIŲ IR TECHNOLOGIJOS MOKSLŲ CENTRAS

Ignas

STASEVIČIUS

# Pakopinio netiesiškumo įtaka femtosekundinio optinio parametrinio osciliatoriaus charakteristikoms

**DAKTARO DISERTACIJA**

Gamtos mokslai,

Fizika (N 002)

---

VILNIUS 2020

Disertacija rengta 2015– 2020 metais Vilniaus universitete, Lazerinių tyrimų centre. Mokslinius tyrimus rėmė Lietuvos mokslų taryba ir MITA.

**Mokslinis vadovas:**

**Prof. dr. Mikas Vengris** (Vilniaus universitetas, gamtos mokslai, fizika, N 002).

## Acknowledgments

Once I gave a try to generate a femtosecond OPO and it took me to years long journey through the “wild” of physics I could not imagine existing beforehand. This was not the easiest of the journeys – demanding, but rewarding with the moments of revelation. And this could not be even started without a supportive and enthusiastic people which I have met on my way.

First of all, I would like to thank my family – my parents Sigitas and Dalia, my wife Dominyka, my child Vincas, my brother Rokas and sister Viltė and everyone else who believed that achieving something as crazy as this could be a normal goal to pursue.

I would like to thank the colleagues at “Light Conversion” – especially Romualdas Danielius and Linas Giniunas. Linas was the one who led me to the first encounter with the femtosecond OPO. Romas was the one who showed me what it takes to do something well and I was really lucky to be able to work with him. Overall, it is safe to say that without “Light Conversion” there would not be this thesis and understanding of physical peculiarities brought with it.

Last but not least, I would like to thank my supervisor Mikas Vengris. He was an example of optimist and enthusiast who did not wave away all the strange suggestions and questions which I have presented. His support was one of the motivations to carry out the research of the OPO presented in this thesis.

To conclude, I would like to quote Isaac Newton – standing on the shoulders of giants makes any task feasible. And I was really lucky to be able to stride this journey on the shoulders of the giants.

# Contents

|   |    |
|---|----|
| Contents.....   | 6  |
| 1 Introduction.....   | 9  |
| 1.1 Motivation.....   | 13 |
| 1.2 Novelty and relevance.....                                    | 14 |
| 1.3 Practical gain.....   | 15 |
| 1.4 Thesis statements.....  | 16 |
| 1.5 Approbation.....  | 17 |
| 1.6 Author's contribution.....                                    | 19 |
| 1.7 Co-author's contribution.....                                 | 20 |
| 2 Introduction to femtosecond OPOs.....                           | 21 |
| 2.1 Nonlinear optics and third order nonlinear susceptibility ... | 22 |
| 2.1.1 Introduction to nonlinear optics.....                       | 22 |
| 2.1.2 Third order nonlinear susceptibility.....                   | 26 |
| 2.2 Coupled wave equations for ultrashort pulses.....             | 35 |
| 2.2.1 Plane and monochromatic wave model.....                     | 39 |
| 2.2.2 Plane wave and pulse model.....                             | 40 |
| 2.2.3 Beam and monochromatic wave model.....                      | 42 |
| 2.2.4 Beam and pulse model.....                                   | 45 |
| 2.3 Cascaded Nonlinearity.....                                    | 47 |
| 2.4 Time domain solitons in OPO.....                              | 53 |
| 2.5 OPO resonator stability.....                                  | 56 |
| 3 OPO with negative GDD.....                                      | 61 |
| 3.1 Experimental procedures.....                                  | 62 |
| 3.2 Results and discussion.....                                   | 65 |
| 3.3 Summary.....  | 72 |
| 4 OPO with negative GDD and CQN.....                              | 73 |
| 4.1 Experimental procedures.....                                  | 74 |
| 4.2 Results and discussion.....                                   | 77 |
| 4.3 Summary.....  | 90 |
| 5 OPO with positive GDD and CQN.....                              | 91 |
| 5.1 Experimental procedures.....                                  | 93 |
| 5.2 Results and discussion.....                                   | 96 |
| 5.2.1 Single nonlinear crystal scheme with DFG CQN.....           | 96 |

|       |   |     |
|-------|---|-----|
| 5.2.2 | Double nonlinear crystal scheme with SHG CQN.....                             | 98  |
| 5.2.3 | Wavelength tuning with DFG and SHG CQN.....                                   | 103 |
| 5.3   | Summary.....  | 110 |
| 6     | Soliton formation effects with GDD compensated CQN.....                       | 111 |
| 6.1   | Experimental procedures .....   | 113 |
| 6.2   | Results and discussion .....  | 114 |
| 6.2.1 | CQN tuning by crystal rotation with fixed cavity GDD<br>114                   |     |
| 6.2.2 | CQN tuning by central wavelength change with varying<br>intracavity GDD ..... | 117 |
| 6.2.3 | CQN tuning spectral and time-domain behaviour.....                            | 125 |
| 6.3   | Summary.....  | 130 |
| 7     | Spatial domain CQN effects.....   | 131 |
| 7.1   | Experimental procedures .....   | 132 |
| 7.2   | Results and discussion .....  | 137 |
| 7.3   | Summary.....  | 150 |
| 8     | Applications of the assembled OPO.....  | 151 |
| 8.1   | Nonlinear microscopy.....   | 152 |
| 8.1.1 | Experimental procedures.....  | 153 |
| 8.1.2 | Results and discussion.....   | 155 |
| 8.1.3 | Summary .....   | 159 |
| 8.2   | Two-photon polymerization .....   | 160 |
| 8.2.1 | Experimental procedures.....  | 161 |
| 8.2.2 | Results and discussion.....   | 162 |
| 8.2.3 | Summary .....   | 165 |
| 8.3   | Two-photon optogenetics .....   | 166 |
| 8.3.1 | Experimental procedures.....  | 168 |
| 8.3.2 | Results and discussion.....   | 171 |
| 8.3.3 | Summary .....   | 178 |
| 9     | Conclusions .....   | 179 |
| 10    | References .....  | 180 |
| 11    | List of publications.....   | 190 |

## Acronyms

OPO – Optical parametric oscillator

OPA – Optical parametric amplifier

SPM – Self-phase modulation

BBO –  $\beta$ -Barium Borate ( $\text{BaB}_2\text{O}_4$ )

LBO - Lithium triborate ( $\text{LiB}_3\text{O}_5$ )

XPM – Cross-phase modulation

SHG – Second harmonic generation

DFG – Difference frequency generation

CQN - Cascaded quadratic nonlinearity

GVD – Group velocity dispersion ( $\text{fs}^2/\text{mm}$ )

GDD – Group delay dispersion ( $\text{fs}^2$ )

NIR - Near infrared region (0.75 - 1.4  $\mu\text{m}$ )

CW – Continuous wave

Yb: KGW – Ytterbium doped Potassium Gadolinium Tungstate

Ti: Sa – Titanium sapphire ( $\text{Ti}^{3+}:\text{Al}_2\text{O}_3$ )

# 1 Introduction

The first experimental demonstration of optical parametric oscillator was demonstrated in 1965 by Giordmaine and R. C. Miller [1]. As 55 years have passed, many flavours of the device and the physical effects governing its behavior were investigated. The OPOs were shown to be capable of tuning from near-ultraviolet [2, 3] to mid-infrared [4, 5] emitting from continuous wave [6, 7] to few-cycle femtosecond pulse durations [8, 9], with average powers reaching up to 30 W [10]. The commercial systems are also widely available being a competitive alternative to conventional lasers when wavelength tuning is required. Naturally, a question arises - how can another dissertation contribute to the field so well explored? Intuitively, as nonlinearity is very low in free-space laser resonators, the power scaling of femtosecond pulse duration OPO output should be relatively easy to achieve. But the Ytterbium based femtosecond laser oscillators used as pump sources for OPOs have reached the peak power levels which lead to observable nonlinear effects in femtosecond optical parametric oscillators [11 - 14]. The intrinsic optical nonlinearity of the crystals used in OPOs leads to well-known time and spatial domain phenomena like self-phase modulation and spatial defocusing. Inside the resonator, multiple passes of the pulse and beam lead to convergence to steady-state time and spatial domain solutions which are influenced by minute changes of the nonlinearity. In time domain these steady state solutions lead to pulses which may exhibit soliton-like behaviour if compensated by the linear dispersion. In spatial domain, these solutions lead to beams which has resonator mode's parameters, influenced by the resonator stability.

The mentioned effects are well investigated in solid state laser femtosecond oscillators [15 - 17], and the knowledge can be transferred to explain the optical parametric oscillators. However, the things start being scientifically challenging if one considers the optical parametric amplification under a phase mismatch  $\Delta k$ . Small phase mismatch value induces cascaded quadratic nonlinearity (CQN). The CQN is a nonlinear process, whereby a wave experiences a nonlinear conversion to a different frequency and a subsequent back-conversion to the original frequency. These processes arise from quadratic nonlinearity, like second harmonic generation or parametric amplification, occurring twice. While the frequency of the light remains *unchanged after* this process is over, it *does differ* during the intermediate state. The intermediate frequency wave travels at different velocity until it is back-converted to the original frequency. As a net result, the wave experiences an effective phase shift (delay), compared to purely linear propagation. This process is equivalent

to the propagation in the medium with nonlinear refractive index proportional to  $d_{\text{eff}}^2 / \Delta k$  (where  $d_{\text{eff}}$  is an effective crystal nonlinear coefficient, originating from  $\chi^{(2)}$  nonlinearity), hence allowing to control the sign of the nonlinearity by changing the detuning [18]. This cascaded nonlinearity is superimposed on the intrinsic electronic material nonlinearity, thereby influencing all the aforementioned time and spatial domain effects. The magnitude of the cascaded nonlinearity can be ten times larger than intrinsic electronic nonlinearity [19].

Previous work in the field include pioneering work by DeSalvo *et al.* showing that cascaded nonlinearities induce effective nonlinearity which is proportional to the  $d_{\text{eff}}^2 / \Delta k$  [18]. Gale *et al.* have shown that this effective nonlinearity can be measured using Z-scan setup and expressed as crystal angle dependent  $n_2$  [19]. Šuminas *et al.* demonstrated approaches exploiting cascaded nonlinearities without a resonator: spatiotemporal light bullet generation and supercontinuum generation [21, 22]. Gale *et al.* and Laenen *et al.* have shown experimental observation and analysis of soliton formation of resonating signal or idler pulse in OPO under influence of cascaded nonlinearity [19, 23]. Negative and positive CQN was exploited in a comb generation [24- 26], CW pumped optical parametric oscillators [28] and ultrafast laser oscillators with varying levels of pulse energies [29 - 33]. Nevertheless, a more detailed understanding of CQN impact to femtosecond optical parametric oscillators is still lacking and this was one of the major motivations to perform this dissertation's study.

The cascaded nonlinear effects can be ignored if phase mismatch is zero. But operating the device under vanishing phase mismatch is not a trivial task, as a number of effects contribute to it – the pulse spectral components have varying phase mismatch because of finite acceptance bandwidth of the crystal; large beam divergences are limited by crystal acceptance angle; crystal temperature changes are limited by crystal acceptance temperature, all defined in [20]. So, ideally, the cascaded nonlinear effects could be ignored if all three – acceptance bandwidth, acceptance angle and acceptance temperature - are larger than the experimental variations. Unfortunately, no practical devices are feasible that operate under such ideal conditions, and the effects of cascaded nonlinearity are always evident to a smaller or larger extent. Furthermore, if gain bandwidth allows, the preferred method of wavelength tuning is the variation of synchronous pumping condition by simultaneous resonator length and wavelength change, while keeping the crystal angle fixed. This leads to operation at a small phase mismatch, which increases at the edges of the tuning curve [34] and the impact of the CQN effects grows near the

limits of the tuning curve. Other effects limiting the peak power scaling are damage of the optical components [35] and thermal effects if the absorption is high enough [36]. In our investigated wavelength ranges and peak power levels, the nonlinear effects are dominating the thermal ones as the LBO and BBO bandgap is respectively  $\sim 3.2$  and  $\sim 2.7$  larger [37] than the 515 nm pump photon energy and no nonlinear components damage was observed through the experiments. Therefore, the cascaded nonlinearity is one of the main effects hindering the further peak power scaling of the optical parametric oscillators. The peak power limiting effects of the cascaded nonlinearity under phase mismatched operation are demonstrated in the chapters 3 and 4 of this dissertation. The influence of the spatial domain focusing / defocusing caused by cascaded nonlinearity are discussed in the chapter 7 of this dissertation.

Cascaded quadratic nonlinearities are not always bad news, though. They can be considered not only as a hindrance, but also as an invaluable tool. The CQN can be tuned by changing the phase mismatch and its sign can be varied from positive to negative. Negative nonlinearity is an unusual phenomenon as naturally this can only be accessed in electron plasma and materials with incident wavelengths below single-photon absorption and above two-photon absorption resonances, which would lead to large absorption losses by free carriers [38]. Thermal defocusing is also observed in liquids and gasses [39]. The negative cascaded nonlinearity can be exploited for the compensation of a positive linear dispersion of the resonator that tends to broaden the light pulse being amplified. With the two effects cancelling each other out, a unique wavelength-tunable device can be constructed, generating soliton-like pulses in a resonator with positive group delay dispersion, as demonstrated in chapter 5 and chapter 6 of this dissertation. What is more, complex interplay between different nonlinearities and the feedback inherent in OPO resonator produces interesting nonlinear dynamics, leading to complex spatiotemporal light structures, solitons, oscillations and chaos. This leads to a very interesting field of research.

Another point to consider is the power scaling motivation from the application's point of view. Femtosecond optical parametric oscillators are devices with a unique combination of characteristics: short pulse durations, broad wavelength tunability and high pulse repetition rate [27]. These parameters lead to applications where fast, wavelength selective and nonlinearly excitable physical processes are observed. The main applications favoring such set of parameters are two photon microscopy and two photon polymerization. In both of these applications, the beam is usually coupled to high numerical aperture objective, which inevitably has losses, especially when broader wavelength tuning range is

considered. What is more, faster scanning speeds require larger pulse energies to decrease the pixel dwell times [40]. Both these requirements lead to the need of an increased peak power of the optical parametric oscillator output. The practical application requires device with small footprint, which for a wavelength tunable device is usually limited by an intracavity prism pair. In order to operate without a prism pair, a positive resonator group delay dispersion can be compensated with negative cascaded nonlinearity, which was experimentally demonstrated in this dissertation. The experimental applications of the assembled and transportable optical parametric oscillator are discussed in chapter 8 of this dissertation.

## 1.1 Motivation

The current state-of-the-art in the field of science and technology concerning ultrafast OPOs, and the challenges of power scaling arising with the development of novel high-power pump sources dictate the following main goal of this dissertation:

Explore the effects of cascaded quadratic nonlinearities in OPOs pumped by high power near-infrared lasers; devise new methods of controlling and exploiting these nonlinearities to enable the scaling the power of OPOs and open new areas of their applications.

To achieve this goal, the research effort was sub-divided in the following tasks:

- Understanding of the cascaded nonlinear processes hindering the peak power scaling of the OPO.
- Exploitation of the negative cascaded nonlinear processes for generation of unique soliton-like pulses from positive GDD resonator.
- Assembly of a transportable femtosecond optical parametric oscillator prototype to test it in the field at leading laboratories in applications of nonlinear microscopy, 2-photon polymerization and 2-photon optogenetics.

## 1.2 Novelty and relevance

The main novel scientific contribution of this dissertation is a number of effects and applications that, to our knowledge, were demonstrated here for the first time.

- The influence of the SHG- and DFG-induced cascaded nonlinearity on the operation of femtosecond optical parametric oscillator was investigated.
- Soliton-like pulses were demonstrated and higher order soliton formation effects were investigated in femtosecond optical parametric oscillator with positive cavity group delay dispersion and negative cascaded nonlinearity.
- Spatial defocusing caused by cascaded nonlinearity caused influence to the femtosecond optical parametric oscillator mode formation was investigated.
- First demonstration of optogenetic application of the developed double-wavelength OPO prototype was performed, where all-optical simultaneous imaging of neural activity using calcium indicator GCaMP was combined with the excitation of opsin C1V1 was performed in mice *in-vivo*.

### **1.3 Practical gain**

A number of scientific contributions led to further understanding of the effects observable in high power femtosecond oscillators. These findings help to understand the spatial and time domain nonlinearity induced peculiarities when output power is scaled to higher values with higher power pump oscillators. Based on these results, a working prototype of a femtosecond optical parametric oscillator was assembled and transported to several application labs (in Lithuania, United Kingdom, Germany) for validation purposes.

## 1.4 Thesis statements

- Cascaded nonlinearity induced effective cubic nonlinearity can be used to compensate (resonating pulse quality of  $\Delta\nu\Delta\tau\sim 0.44$ ) or amplify (resonating pulse quality of  $\Delta\nu\Delta\tau\sim 3$ ) the self-phase modulation effects inherent in high power femtosecond optical parametric oscillators with both signs of intracavity dispersion.
- The quadratic nonlinearity of a second SHG signal crystal inserted into an OPO cavity can be employed to induce tunable negative nonlinearity (for BBO up to  $n_2\sim -15 \times 10^{-20} \text{ m}^2/\text{W}$ ) for positive group delay dispersion compensation (up to  $GDD\sim 5000 \text{ fs}^2$ ) and allow soliton formation (with pulse quality of  $\Delta\nu\Delta\tau\sim 0.44$ ). Using this approach, the conversion efficiency (OPO crystal angle) and nonlinearity tuning (SHG crystal angle) can be independently adjusted.
- Large cascaded-nonlinearity-induced phase shifts lead to the generation of higher order solitons (up to the 3<sup>rd</sup> order), exhibiting oscillatory behaviour (periods vary from 11 to 18 resonator roundtrips) unless perturbed by the 3<sup>rd</sup> order of the nonlinear dispersion.
- Cascaded nonlinearity with up to  $20 \text{ GW}/\text{cm}^2$  intensity in the 2.5 mm length LBO crystal induces nonlinear spatial focusing (dioptric power up to  $D\sim 33 \text{ m}^{-1}$ ) or defocusing (dioptric power up to  $D\sim -9 \text{ m}^{-1}$ ) which is strong enough to drive the resonator out of the stability if it is set to operate close (within less than 5 % of the whole stability range) to the linear stability limits.
- Femtosecond optical parametric oscillator wavelength tunable in the ranges of 700 – 950 nm or 950 - 1300 nm is a practical and versatile laser source suitable for applications in nonlinear microscopy, optogenetics and 3D direct laser writing.

## 1.5 Approbation

The results of the thesis were presented in the following peer-reviewed scientific publications:

P1. K. Stankevičiūtė, I. Pipinytė, I. Stasevičius, J. Vengelis, G. Valiulis, R. Grigonis, M. Vengris, M. Bardauskas, L. Giniunas, O. Balachninaite, R.C. Eckardt, V. Sirutkaitis, „Femtosecond optical parametric oscillators synchronously pumped by Yb:KGW oscillator“, *Lithuanian Journal of Physics*, Vol. 53, No. 1, 41–56 (2013).

P2. J. Vengelis, I. Stasevičius, K. Stankevičiūtė, V. Jarutis, R. Grigonis, M. Vengris, V. Sirutkaitis, „Characteristics of optical parametric oscillators synchronously pumped by second harmonic of femtosecond Yb:KGW laser“, *Optics Communications* 338, 277–287 (2015).

P3. K. Ivanauskiene, I. Stasevicius, M. Vengris, V. Sirutkaitis, “Pulse-to-pulse instabilities in synchronously pumped femtosecond optical parametric oscillator”, *J. Opt. Soc. Am. B* 36 (1), 131-139 (2019).

P4. I. Stasevicius, G. Martynaitis, M. Vengris, “Cascaded nonlinearities in high-power femtosecond optical parametric oscillator”, *J. Opt. Soc. Am. B* 37 (3), 721-729 (2020).

P5. I. Stasevicius, M. Vengris, „Exploiting optical nonlinearities for group delay dispersion compensation in femtosecond optical parametric oscillators“, *Optics Express* 28 (18), 26122-26136 (2020).

P6. I. Stasevicius, M. Vengris, „Controlled soliton formation in femtosecond optical parametric oscillator with positive group delay dispersion“, *J. Opt. Soc. Am. B* 37 (10), 2956-2967 (2020).

P7. I. Stasevicius, M. Vengris, „Cascaded nonlinearity induced spatial domain effects in high power femtosecond optical parametric oscillator“, *Opt. Express* 28 (22), 33490-33503 (2020)

The author has presented the results of the thesis at the following scientific conferences:

C1. I. Stasevicius, M. Vengris, R. Danielius, „Development of simple and robust femtosecond optical parametric oscillator for multiphoton imaging“, „Photonics West“, USA, San Francisco, 2017.

C2. I. Stasevicius, M. Vengris, „Simple and robust femtosecond optical parametric oscillator for multiphoton imaging“, „Focus On Microscopy“, France, Bordeaux, 2017.

C3. I. Stasevicius, G. Martynaitis, M. Vengris, „Cascaded nonlinearity influence to high power femtosecond optical parametric oscillator“, „Photonics West“, USA, San Francisco, 2020.

The results of the thesis presented by the co-authors at the scientific conferences:

CO1. V. Purlys, D. Gailevicius, I. Stasevicius, V. Voiciuk, S. Vaisiunas, R. Gadonas, „Influence of Laser Wavelength for Direct Laser Writing Thresholds“, „CLEO“, Germany, Munich, 2017

CO2. Ting Fu, Isabelle Arnoux, Jan Döring, Hirofumi Watari, Ignas Stasevicius, Albrecht Stroh, „Navigating the translational roadblock: Towards highly specific and effective all-optical interrogations of neural circuits“, „FENS 2020 Virtual Forum“, online conference, 2020.

## **1.6 Author's contribution**

The author has designed and implemented all the experimental setups and performed the measurements presented in P5 - P7. The author participated in the setup of experiments and the measurements presented in P1, P2 and P4. The author has written a Matlab code and performed numerical simulations of the experimental results presented in P2 - P7. The author assembled a transportable prototype of the OPO and took part in the 2 photon imaging experiments presented in CO2. The author assembled a transportable prototype of the OPO which was used in the experiments presented in CO1. The author prepared manuscripts of P4 - P7 and took part in the preparation of manuscripts of P1 - P3.

## 1.7 Co-author's contribution

- Dr. Mikas Vengris helped to interpret the experimental results and was heavily involved in proof-reading the manuscripts P3 - P7. In one way or another, Mikas was involved in all the parts presented in the thesis.
- Dr. Vygantas Jarutis provided help and shared insights regarding the numerical simulation code of coupled optical parametric amplification equations presented in P2. All the simulations done by the author in P3 - P7 relied on the successful implementation of that code.
- Dr. Romualdas Danielius and Dr. Linas Giniūnas initiated and helped the development of the experimental setups into transportable prototype which could be tested in the field applications presented in CO1 and CO2.
- Dr. Karolina Stankevičiūtė and Dr. Julius Vengelis assembled the experimental schemes in P1 – P3, have done majority of measurements and helped to discuss the experimental results.
- Giedrius Martynaitis assembled a part of the experimental scheme presented in P4 and helped exploring various OPO peculiarities during investigation.
- Dr. Vytautas Purlys, Dr. Darius Gailevicius, Dr. Vlada Voiciuk, Saulius Vaisiunas have done a majority of the experimental work described in CO2, from the optical scheme assembly and experiment automatization to the 2P polymerization experiment and interpretation of the results.
- Dr. Roaldas Gadonas and dr. Vytautas Purlys devised the variable wavelength 2 photon photopolymerization experiment which was presented in CO1.
- Dr. Ting Fou, Dr. Isabelle Arnoux, Hirofumi Watari have done a majority of experimental work described in CO2, from mouse viral injections to 2 photon imaging experiments and interpretation of the data.
- Prof. Albrecht Stroh devised the two-photon all optical neurogenetics experiment which was realised and presented in CO2.

## 2 Introduction to femtosecond OPOs

Femtosecond optical parametric oscillator is an optical parametric amplifier consisting of a nonlinear crystal placed inside a resonator, usually pumped with oscillators having low pulse energy ( $\sim 50$  nJ) and high repetition rate ( $\sim 100$  MHz). Low pump pulse energies lead to small single pass gain for even weaker signal wave. The use of the resonator recirculating signal wave enables efficient signal power build up and pump energy extraction. Amplified signal beam is resonated while undepleted pump is provided for every cavity roundtrip. The amplification is efficient if the repetition rates of the pump and resonating signal pulse are the same, hence satisfying the synchronous pumping condition.

Locking the pulse inside the resonator leads to time and spatial domain effects not observed in a single pass OPA – in time domain the interplay between dispersion and cavity nonlinearity leads to a stable soliton-like pulse. In spatial domain, the interplay between cavity nonlinearity and linear cavity stability leads to stable (or not) cavity spatial mode. The cavity nonlinearity consists of intrinsic material nonlinearity and an additional OPA induced cascaded nonlinearity part. In order to understand these effects, numerical simulation stands out as invaluable tool.

As such, following chapter introduces to the five main concepts critical to the understanding of optical parametric oscillators:

- Introduction to nonlinear optics and third order nonlinear susceptibility.
- Coupled wave equations for the ultrashort pulses.
- Cascaded nonlinearity.
- Soliton pulses.
- Resonator modes and stability.

## 2.1 Nonlinear optics and third order nonlinear susceptibility

### 2.1.1 Introduction to nonlinear optics

The effects of the nonlinear optics are pronounced when material's response to an incident electric field has a nonlinear dependence on the electric field strength. In order to understand the origin of the nonlinearity, a closer look into microscopic material nonlinear polarization  $P(t)$  is needed. At low intensity limit, the material's response is linear:

$$P(t) = \varepsilon_0 \chi^{(1)} E(t). \quad (2.1)$$

The quantities  $P(t)$  and  $E(t)$  are the vectors of nonlinear polarization and electric field strength respectively,  $\chi^{(1)}$  is the linear susceptibility,  $\varepsilon_0$  is vacuum permittivity. The nonlinear response of a material to a strong incident optical electric field can be described similarly: the polarization vector is expanded in power series in the field strength  $E(t)$  with coefficients describing the order of nonlinear polarization effect:

$$\begin{aligned} P(t) &= \varepsilon_0 \chi^{(1)} E(t) + \varepsilon_0 \chi^{(2)} E^2(t) + \varepsilon_0 \chi^{(3)} E^3(t) + \dots \\ &= P^{(1)}(t) + P^{(2)}(t) + P^{(3)}(t) + \dots \end{aligned} \quad (2.2)$$

The quantities  $\chi^{(2)}$  and  $\chi^{(3)}$  are the second and third order nonlinear optical susceptibilities. The assumption is made that the material response is instantaneous, there is no absorption and dispersion. The quantities  $P(t)^{(2)}$  and  $P(t)^{(3)}$  are called second and third order nonlinear polarization terms respectively. Due to symmetry reasons,  $\chi^{(2)}$  processes can only occur in non-centrosymmetric media, such as crystals or interfaces between different materials. In the meantime,  $\chi^{(3)}$  processes can occur both for centrosymmetric and non-centrosymmetric materials (centrosymmetric solid state materials, liquids, gases and plasma). The comparison

of the expansion series terms allows evaluating the approximate order of susceptibilities. The second term of the power series expansion, the polarization vector  $P(t)^{(2)}$  should be comparable to the first order polarization vector  $P(t)^{(1)}$  when incident electric field strength is close to the atomic electric field between valence electrons and nuclei. For hydrogen atom, this electric field can be evaluated as

$$E_{at} = \frac{e}{4\pi\epsilon_0 a^2}, \quad (2.3)$$

where  $e$  – electron's charge,  $a = 4\pi\epsilon_0 \hbar^2 / me^2$  is Bohr's radius. Inserting the constants, the electric field strength which acts on electron in orbital is  $E_{at} = 5.1 \times 10^{11}$  V/m. Thus, it could be expected that the second-order susceptibility  $\chi^{(2)}$  should be of an order of  $\chi^{(1)} / E_{at}$ :

$$\chi^{(2)} \sim \chi^{(1)} / E_{at} \sim 2 \times 10^{-12} \text{ m/V}.$$

In the same way  $\chi^{(3)}$  should be of a similar order as  $\chi^{(1)} / E_{at}^2$ :

$$\chi^{(3)} \sim \chi^{(1)} / E_{at}^2 \sim 4 \times 10^{-24} \text{ m}^2/\text{V}^2.$$

These values are close to the ones experimentally observed in the most common optical materials [41, 42].

When strong electric field is incident in the material, nonlinear polarization acts as a source of newly generated electromagnetic field that can have new frequencies. This result stems from Maxwell's equations, where incident and emitted fields are coupled through the nonlinear term:

$$\nabla^2 E - \frac{n^2}{c^2} \frac{\partial^2 E}{\partial t^2} = \frac{1}{\epsilon_0 c^2} \frac{\partial^2 P_{NL}}{\partial t^2}, \quad (2.4)$$

where  $P_{NL}$  is nonlinear polarization,  $n$  – refractive index and  $c$  is light velocity in vacuum. When the second derivative of nonlinear polarization  $\frac{\partial^2 P_{NL}}{\partial t^2}$  is non-zero, the charge carriers inside the medium are subjected to the electric force. They get

accelerated and according to Larmor theorem, the transverse electric field component is emitted as an electromagnetic wave [43].

In order to find the solutions to this equation, several approximations can be made. First of all, the waves are assumed to be plane and monochromatic. The spatial effects such as the walk-off of extraordinary beam are ignored. Let us investigate the case of sum frequency generation, when two fields with frequencies  $\omega_1$  and  $\omega_2$  arrive at the nonlinear medium. By plugging two plane waves with such frequencies into the expression for quadratic polarization, it follows obvious, that the source term in Eq. 2.4 will contain zero frequency, as well as  $2\omega_1$ ,  $2\omega_2$ ,  $\omega_1 + \omega_2$  and  $\omega_1 - \omega_2$ . Let us look further at the sum frequency  $\omega_3 = \omega_1 + \omega_2$ . An electric field of sum frequency wave can be defined as:

$$\vec{E}_3(z, t) = E_3 e^{i(k_3 z - \omega_3 t)} + c.c., \quad (2.5)$$

where  $E_3$  is electric field amplitude and  $k_3 = n_3 \omega_3 / c$  is a wave vector. If a nonlinear driving term of equation (2.4) is small, a solution of wave equation will be similar to the one defined in (2.5). Similarly, the driving nonlinear polarization term can be defined as:

$$\vec{P}_3(z, t) = P_3 e^{-i\omega_3 t} + c.c.. \quad (2.6)$$

The sum frequency nonlinear polarization component can be expressed as:

$$P_3 = 4 \varepsilon_0 d_{eff} E_1 E_2, \quad (2.7)$$

where  $d_{eff}$  is an effective nonlinearity, which depends on the interaction geometry and the properties of the nonlinear crystal. In anisotropic medium, the nonlinear susceptibility  $\chi^{(2)}$  is a tensor with components defined as  $d_{ijk} = \frac{\chi^{(2)}_{ijk}}{2}$ , an effective nonlinearity  $d_{eff}$  can be calculated if interacting polarizations and geometry are known. The fields of the incident beams can be defined as:

$$E_i(z, t) = E_i e^{i(k_i z - \omega_i t)} + c.c., \quad (2.8)$$

where  $i = 1, 2$  for both incident fields. The nonlinear polarization amplitude can be defined as:

$$P_3 = 4 \varepsilon_0 d_{eff} E_1 E_2 e^{i(k_1+k_2)z} . \quad (2.9)$$

Both of these expressions can be inserted into the nonlinear wave equation (2.4). Calculating the derivatives and using the slowly varying amplitude approach, we arrive at the equation for the amplitude of sum frequency wave:

$$\frac{d E_3}{d z} = \frac{2i d_{eff} \omega_3^2}{k_3 c^2} E_1 E_2 e^{i(k_3-k_1-k_2)z} . \quad (2.10)$$

This equation allows the following conclusions: a) the sum frequency amplitude depends on the amplitudes of the incident fields  $E_1$  and  $E_2$ , effective nonlinearity and a harmonic term  $e^{i(k_3-k_1-k_2)z}$ . The difference of the wavevectors is defined as  $\Delta k = k_3 - k_2 - k_1$ . The equation also shows that after some propagation distance with non-zero  $\Delta k$ , the nonlinear polarization created wave will have a phase opposite to the phase of the nonlinear polarization. This nonlinear polarization would then create a wave out of phase with the initially propagating wave, and their destructive interference would decrease the amplitude of the total propagating wave. In order to prevent this effect, the nonlinear polarization should propagate with a same phase velocity as a newly created electric field. According to the energy conservation law, the frequency of the created wave is a sum of interacting frequencies. So matching of the phase velocities requires matching of the wave vectors, leading to these phase matching conditions [44]:

$$\omega_3 = \omega_1 + \omega_2 , \quad (2.11)$$

$$\vec{k}_3 = \vec{k}_1 + \vec{k}_2 . \quad (2.12)$$

Continuing the analysis of (2.10) equation, we define a nonlinear coefficient indicating the strength of the nonlinear coupling:

$$\sigma_j = \frac{2 d_{eff} \omega_j^2}{k_j c^2} . \quad (2.13)$$

The three wave coupled nonlinear equations can then be defined as:

$$\frac{d E_1}{d z} = -i\sigma_1 E_3 E_2^* e^{-i\Delta k z}, \quad (2.14)$$

$$\frac{d E_2}{d z} = -i\sigma_2 E_3 E_1^* e^{-i\Delta k z}, \quad (2.15)$$

$$\frac{d E_3}{d z} = -i\sigma_3 E_1 E_2 e^{i\Delta k z}. \quad (2.16)$$

The equations (2.15) and (2.16) are derived in the same way with a difference frequency generation component of the nonlinear polarization leading to new frequencies  $\omega_1 = \omega_3 - \omega_2$  and  $\omega_2 = \omega_3 - \omega_1$  and corresponding nonlinear coefficients  $\sigma$  [41, 42].

The equations (2.14) to (2.16) form a backbone of nonlinear optics, being of extreme importance to explanation of OPA process, which is inherent in OPO as well.

### 2.1.2 Third order nonlinear susceptibility

Third order nonlinear susceptibility is of a paramount importance to the understanding of the operation of the OPO and to the applications of the assembled device. Operation of the OPO is influenced by the real part of the third order nonlinear susceptibility - nonlinear refractive index. It can arise from purely third order effects, or be a combination of third order susceptibility and the cascaded quadratic nonlinearity. The applications of the assembled OPO also rely on the imaginary part of the third order susceptibility, which describes two-photon absorption in a sample under intense electric field illumination. Understanding the origin of this effect leads to more effective nonlinear microscopy and nonlinear photopolymerization techniques. Similarly to the real part, the imaginary part of the third order susceptibility is an analogous to the imaginary part of the effective cascaded nonlinearity which is responsible for the generation of the second harmonic (which acts as the intensity dependent losses of the fundamental light, in the same way as in two photon absorption case) [45].

To simplify the derivation of real and imaginary parts of third order susceptibility, the centrosymmetric medium is investigated with  $\chi^{(2)} = 0$ . The polarization in such medium can be expressed as:

$$P(E(\omega)) = P^{(1)} + P^{(3)} = \varepsilon_0 \left( \chi^{(1)} + 3\chi^{(3)} |E(\omega)|^2 \right) E(\omega), \quad (2.17)$$

where  $P^{(1)}$  and  $P^{(3)}$  are linear and third order polarizations, respectively. The linear and third order susceptibilities are  $\chi^{(1)}$  and  $\chi^{(3)}$ . They can be separated to real and imaginary parts as follows:

$$\chi^{(1)} = \chi_R^{(1)} + i\chi_I^{(1)}, \quad (2.18)$$

$$\chi^{(3)} = \chi_R^{(3)} + i\chi_I^{(3)}, \quad (2.19)$$

where  $\chi_R^{(1)}$  and  $\chi_R^{(3)}$  are real part and directly related to the refraction.  $\chi_I^{(1)}$  and  $\chi_I^{(3)}$  are imaginary parts and related to absorption.

Nonlinear refraction is induced by the real part of polarization vector, the total polarization of the material system is according to (2.17) equation:

$$P_R(E(\omega)) = P_R^{(1)} + P_R^{(3)} = \varepsilon_0 \left( \chi_R^{(1)} + 3\chi_R^{(3)} |E(\omega)|^2 \right) E(\omega). \quad (2.20)$$

The electric displacement vector:

$$D = \varepsilon_0 E + P = \varepsilon_0 \left( 1 + \chi_R^{(1)} + 3\chi_R^{(3)} |E(\omega)|^2 \right) E(\omega). \quad (2.21)$$

According to  $D = \varepsilon E$ , the total permittivity is:

$$\varepsilon = \varepsilon_0 \left( 1 + \chi_R^{(1)} + 3\chi_R^{(3)} |E(\omega)|^2 \right). \quad (2.22)$$

The refractive index is defined as:

$$n = \sqrt{\varepsilon_r \mu_r}, \quad (2.23)$$

where  $\mu_r$  is relative permeability and generally equals to 1 for non-magnetic materials. Inserting formula (2.22) into (2.23) yields:

$$n = \sqrt{1 + \chi_R^{(1)} + 3\chi_R^{(3)} |E(\omega)|^2}. \quad (2.24)$$

The linear refractive index is given by:

$$n_0^2 = 1 + \chi_R^{(1)}. \quad (2.25)$$

Using equation (2.25) formula (2.24) can be rewritten as:

$$n = n_0 \left( 1 + \frac{3\chi_R^{(3)} |E(\omega)|^2}{n_0^2} \right)^{\frac{1}{2}}. \quad (2.26)$$

Using Taylor series expansion, the refractive index formula can be expressed as:

$$n \sim n_0 + \frac{3\chi_R^{(3)} |E(\omega)|^2}{2n_0}. \quad (2.27)$$

Intensity-dependent refractive index can then be defined as:

$$n = n_0 + \Delta n = n_0 + n_2 I, \quad (2.28)$$

where  $n_2$  is nonlinear refraction index and light intensity  $I$  is defined as follows:

$$I = \frac{1}{2} \varepsilon_0 c n_0 \langle E \rangle^2. \quad (2.29)$$

Substituting formula (2.29) to (2.27) one obtains:

$$n \sim n_0 + \frac{3\chi_R^{(3)} I}{\varepsilon_0 c n_0^2}. \quad (2.30)$$

According to formula (2.28), the nonlinear refraction index  $n_2$  is written as:

$$n_2 = \frac{3\chi_R^{(3)}}{\varepsilon_0 c n_0^2}. \quad (2.31)$$

Different physical mechanisms can cause different  $n_2$  values, with values ranging from  $\sim 10^{-20} \frac{m^2}{W}$  (electronic polarization) to  $\sim 10^{-10} \frac{m^2}{W}$  (thermal effects). The nonlinear refractive index is a source of self-phase modulation which distorts the spectrum and temporal / spectral phase in femtosecond optical parametric oscillators. The equation (2.31) shows that the origin of the nonlinear refractive index is the real part of the third order susceptibility.

Following the same procedure as carried out with a real part of polarization, an imaginary part of polarization is given by:

$$P_I(E(\omega)) = P_I^{(1)} + P_I^{(3)} = \varepsilon_0 \left( \chi_I^{(1)} + 3\chi_I^{(3)} |E(\omega)|^2 \right) E(\omega). \quad (2.32)$$

Applying the slowly varying-envelope approximation to an isotropic medium, one has:

$$\frac{dE}{dz} = -\frac{i\omega}{2\varepsilon_0 n_0} P_I. \quad (2.33)$$

Substituting formulas (2.29) and (2.32) into formula (2.33), one has:

$$\frac{dE}{dz} = -\left( \frac{\omega}{2cn_0} \chi_I^{(1)} + \frac{3\omega}{\varepsilon_0 c^2 n_0^2} \chi_I^{(3)} I \right) E. \quad (2.34)$$

Linear absorption coefficient can be defined as:

$$\frac{\alpha}{2} = \frac{\alpha_0}{2} + \frac{\Delta\alpha}{2} = \frac{\omega}{2cn_0} \chi_I^{(1)} + \frac{3\omega}{\varepsilon_0 c^2 n_0^2} \chi_I^{(3)} I. \quad (2.35)$$

Formula (2.34) can be rewritten as:

$$\frac{dE}{dz} = -\frac{\alpha}{2}E. \quad (2.36)$$

And the solution to the equation (2.36) is given by:

$$E = E_0 e^{(-\frac{\alpha}{2}L)}. \quad (2.37)$$

Thus,  $\alpha_0$  is defined as a linear absorption coefficient and  $\Delta\alpha$  is nonlinearity-induced intensity dependent absorption coefficient change and is given by:

$$\Delta\alpha = \beta I, \quad (2.38)$$

where  $\beta$  is nonlinear absorption coefficient and is defined as:

$$\beta = \frac{\omega}{\epsilon_0 c^2 n_0^2} \chi_1^{(3)}. \quad (2.39)$$

The light goes through the nonlinear material and the intensity decreases with the traveling distance  $z$  inside the material. This intensity decay can be rewritten as:

$$\frac{dI}{dz} = -\alpha_0 I - \beta I^2. \quad (2.40)$$

This is the master equation which governs the intensity change when nonlinear absorption takes place. Femtosecond pulses have intensities large enough to make the  $\beta I^2$  factor non-negligible. This leads to the plethora of applications based on multiphoton absorption such as two photon microscopy or two photon polymerization [41, 46].

To investigate frequency response of the second and third order nonlinear susceptibilities, let us use the Lorentz model of the atom, where the atom is treated as a harmonic oscillator. This model is known to provide a very good description of the linear optical properties of nonmetallic solids. Lorentz model is easily extended to describe wavelength-dependent first, second or third order nonlinear susceptibility of the material. For that, we add the nonlinearity in the restoring force exerted on the

electron. For the case of non-centrosymmetric media ( $a \neq 0$ ), the equation of motion of the electron coordinate  $x$  is written as:

$$\frac{d^2x}{dt^2} + 2\gamma \frac{dx}{dt} + \omega_0^2 x + ax^2 + bx^3 = -\frac{eE(t)}{m}. \quad (2.41)$$

The applied electric field is given by  $E(t)$ , the charge of electron is  $e$ , the damping force is of the form  $2m\gamma \frac{dx}{dt}$ . Terms  $ax^2 + bx^3$  are responsible for second and third order nonlinearity of the system, where  $a$  and  $b$  are constants of nonlinearity. The resonant frequency of the bound electron is denoted  $\omega_0$ . The applied electric field is of the form:

$$E(t) = E_0 e^{-i\omega t} + c.c.. \quad (2.42)$$

The nonlinear differential equation is called Duffing oscillator and is used to model damped and driven oscillators. Direct solving of differential equation (2.41) gives the amplitude response to the applied electric field with the frequency  $\omega$ . Setting the terms  $a$  and  $b$  to zero yields the response curve of classical harmonic oscillator, whereas non-zero  $a$  and  $b$  yield the response curve of anaharmonic oscillator. Both are shown in Fig. 2.1.

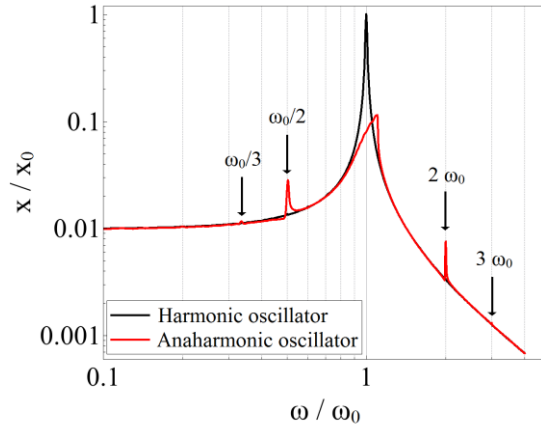


Fig. 2.1. Bound electron amplitude  $x$  dependence on frequency of the applied electric field (divided by bound electron resonance frequency  $\omega_0$ ) of classical harmonic oscillator (black curve) and anharmonic oscillator (red curve).

As can be seen in Fig. 2.1, anharmonic oscillator shows material response at harmonic and subharmonic frequencies  $0.5 \omega_0$ ,  $0.33 \omega_0$  and  $2 \omega_0$ ,  $3 \omega_0$ , indicative of two / three photon absorption and second / third harmonic generation.

Approximate solution to equation (2.41) can be obtained by means of perturbation expansion. Using definition of polarization ( $N$  is the number of dipoles):

$$P = Nxe , \quad (2.43)$$

Linear, the second and the third order nonlinear susceptibilities can then be derived:

$$\chi_{ij}^{(1)} = \frac{1}{\varepsilon_0} \left( \frac{dP_i}{dE_j} \right)_{E=0} , \quad (2.44)$$

$$\chi_{ijk}^{(2)} = \frac{1}{2\varepsilon_0} \left( \frac{d^2P_i}{dE_j dE_k} \right)_{E=0} , \quad (2.45)$$

$$\chi_{ijkl}^{(3)} = \frac{1}{6\epsilon_0} \left( \frac{d^3 P_i}{dE_j dE_k dE_l} \right)_{E=0}. \quad (2.46)$$

Using these derivations, nonlinear susceptibility frequency response can be defined as:

$$\chi^{(1)}(\omega_1) = \frac{Ne^2 / m}{D(\omega_1)}, \quad (2.47)$$

$$\chi^{(2)}(2\omega_1, \omega_1, \omega_1) = \frac{N(e^3 / m^2) a}{D(2\omega_1) D^2(\omega_1)}, \quad (2.48)$$

$$\chi^{(3)}(3\omega_1, \omega_1, \omega_1, \omega_1) = \frac{N(e^4 / 3m^3) b}{D(3\omega_1) D^3(\omega_1)}, \quad (2.49)$$

where complex denominator function is:

$$D(\omega_j) = \omega_0^2 - \omega_j^2 - 2i\omega_j\gamma. \quad (2.50)$$

Frequency-dependent susceptibility functions (2.47) - (2.49) are plotted in Fig. 2.2:

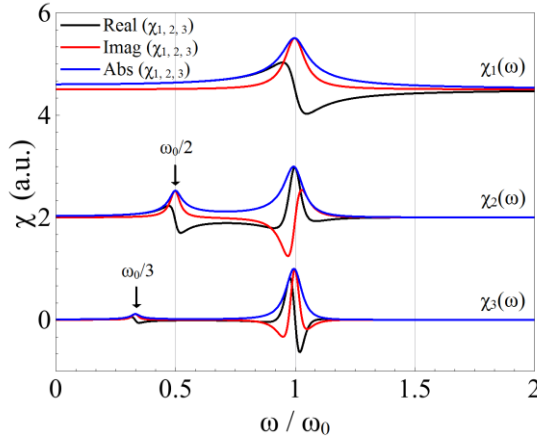


Fig. 2.2. First, second and third order susceptibility real, imaginary part and absolute value dependence on frequency.

From Fig. 2.2, one can see that the nonlinear susceptibility is greatly enhanced at resonance frequencies  $\omega_0, 2\omega_0, 3\omega_0$ , which are related to linear absorption, two photon absorption and three photon absorption respectively. This is the main reason why wavelength tunable laser sources are required in multiphoton absorption applications: they allow tuning the wavelength close to resonance and resonantly enhancing the nonlinear susceptibility which greatly increases the absorption coefficient [41, 46].

## 2.2 Coupled wave equations for ultrashort pulses

If the interacting pulses are ultrashort in time domain, the coupled nonlinear equations should have additional dispersion terms, which would account for dispersive broadening and time domain pulse walk-off. The propagating wave vector can be defined as [41, 42]:

$$k(\Omega) = k(\omega_c) + \delta k, \quad (2.51)$$

where  $\Omega$  is a frequency of the spectrum,  $\omega_c$  is the pulse carrier frequency and  $\delta k$  is the Taylor expansion of the wave vector up to the second order:

$$\delta k = \frac{dk}{d\Omega}_{\omega=\omega_c} (\Omega - \omega_c) + \frac{1}{2} \frac{d^2k}{d\Omega^2}_{\omega=\omega_c} (\Omega - \omega_c)^2, \quad (2.52)$$

The electric field can then be defined as:

$$E(\Omega, z) = E(\Omega, 0) e^{-ik_c z} e^{-i\delta k z}. \quad (2.53)$$

The electric field definition can be inserted into the coupled wave equation derived from Maxwell's equation (2.4), the approximation of a slowly varying amplitude is made in spatial domain, but not in the time domain. The wave equation for ultrashort pulses reads:

$$\left( \frac{\partial}{\partial z} + \frac{1}{u} \frac{\partial}{\partial t} - \frac{ik''}{2} \frac{\partial^2}{\partial t^2} \right) E = i \frac{1}{\epsilon c^2 k} \frac{\partial^2}{\partial t^2} P_{NL}. \quad (2.54)$$

Here,  $u$  is a group velocity,  $k''$  is the second derivative of wave vector with respect to frequency. Analogously to the equations (2.14) - (2.16), inserting the nonlinear polarization term leads to the coupled equations for all three interacting waves. The

equations could be written in pump pulse frame of reference with  $t = t' - \frac{z}{u_g}$ :

$$\frac{\partial E_1}{\partial z} + v_{13} \frac{\partial E_1}{\partial t} - \frac{i}{2} k_1'' \frac{\partial^2 E_1}{\partial t^2} = -i\sigma_1 E_2^* E_3 e^{-i\Delta k z}, \quad (2.55)$$

$$\frac{\partial E_2}{\partial z} + v_{23} \frac{\partial E_2}{\partial t} - \frac{i}{2} k_2'' \frac{\partial^2 E_2}{\partial t^2} = -i\sigma_2 E_1^* E_3 e^{-i\Delta k z}, \quad (2.56)$$

$$\frac{\partial E_3}{\partial z} - \frac{i}{2} k_3'' \frac{\partial^2 E_3}{\partial t^2} = -i\sigma_3 E_1 E_2 e^{i\Delta k z}, \quad (2.57)$$

where  $v_{j3} = u_j^{-1} - u_3^{-1}$  is the group velocity mismatch parameter. In a limiting case of the monochromatic waves when dispersive terms can be ignored, the equations (2.14) - (2.16) are recovered. In the case of parametric amplification, a strong pump pulse  $E_3$  is incident into the material, and a weak signal  $E_1$  and idler  $E_2$  electric fields are amplified simultaneously. The equations are solved with boundary conditions [6]:

$$A_j(t, z=0) = A_{j0}(t), \quad j = 1, 2, 3. \quad (2.58)$$

In the case of strong pump depletion and strong interacting pulse intensities as in optical parametric oscillators, self- and cross-phase modulation terms should be accounted for. The origin of these effects stems from intensity-dependent refractive index introduced in section 2.1.2. Propagating pulse changes the refractive index of the medium, which can modulate its own phase and that of other simultaneously propagating pulses. These effects can be accounted for by inserting the self- and cross-phase modulation terms into the ultrashort pulse equations (2.55) – (2.57) [42, 47]:

$$\begin{aligned} \frac{\partial E_1}{\partial z} + v_{13} \frac{\partial E_1}{\partial t} - \frac{i}{2} k_1'' \frac{\partial^2 E_1}{\partial t^2} &= -i\sigma_1 E_2^* E_3 e^{-i\Delta k z} \\ &- i\beta_1 E_1 \left( |E_1|^2 + \gamma_{12} |E_2|^2 + \gamma_{13} |E_3|^2 \right) \end{aligned}, \quad (2.59)$$

$$\begin{aligned} \frac{\partial E_2}{\partial z} + v_{23} \frac{\partial E_2}{\partial t} - \frac{i}{2} k_2'' \frac{\partial^2 E_2}{\partial t^2} &= -i\sigma_2 E_1^* E_3 e^{-i\Delta k z} \\ &- i\beta_2 E_2 \left( |E_2|^2 + \gamma_{21} |E_1|^2 + \gamma_{23} |E_3|^2 \right) \end{aligned}, \quad (2.60)$$

$$\begin{aligned} \frac{\partial E_3}{\partial z} - \frac{i}{2} k_3'' \frac{\partial^2 E_3}{\partial t^2} = -i\sigma_3 E_1 E_2 e^{i\Delta k z} \\ -i\beta_3 E_3 \left( |E_3|^2 + \gamma_{31} |E_1|^2 + \gamma_{32} |E_2|^2 \right) \end{aligned} \quad , \quad (2.61)$$

where  $\beta_i = \frac{n_2 c \varepsilon_0 k_i}{2}$  is the coefficient of nonlinearity,  $\gamma_{ij}$  is a cross-phase modulation coefficient, which depends on the polarizations of the interacting fields indexed  $i$  and  $j$ . If polarizations are parallel  $\gamma_{ij} = 2$ , whereas in the case of perpendicular polarizations  $\gamma_{ij} = 2/3$ . The expressions indicate that the cross-phase modulation term is two times stronger than self-phase modulation term [47].

In order to account for the spatial distribution of the interacting beams, the diffraction term has to be included into the equations (2.59) – (2.61):

$$\begin{aligned} \frac{\partial E_1}{\partial z} + v_{13} \frac{\partial E_1}{\partial t} - \frac{i}{2} k_1'' \frac{\partial^2 E_1}{\partial t^2} + \frac{i}{2k_{01}} \Delta E_1 = -i\sigma_1 E_2^* E_3 e^{-i\Delta k z} \\ -i\beta_1 E_1 \left( |E_1|^2 + \gamma_{12} |E_2|^2 + \gamma_{13} |E_3|^2 \right) \end{aligned} \quad , \quad (2.62)$$

$$\begin{aligned} \frac{\partial E_2}{\partial z} + v_{23} \frac{\partial E_2}{\partial t} - \frac{i}{2} k_2'' \frac{\partial^2 E_2}{\partial t^2} + \frac{i}{2k_{02}} \Delta E_2 = -i\sigma_2 E_1^* E_3 e^{-i\Delta k z} \\ -i\beta_2 E_2 \left( |E_2|^2 + \gamma_{21} |E_1|^2 + \gamma_{23} |E_3|^2 \right) \end{aligned} \quad , \quad (2.63)$$

$$\begin{aligned} \frac{\partial E_3}{\partial z} - \frac{i}{2} k_3'' \frac{\partial^2 E_3}{\partial t^2} + \frac{i}{2k_{03}} \Delta E_3 = -i\sigma_3 E_1 E_2 e^{i\Delta k z} \\ -i\beta_3 E_3 \left( |E_3|^2 + \gamma_{31} |E_1|^2 + \gamma_{32} |E_2|^2 \right) \end{aligned} \quad , \quad (2.64)$$

where  $k_{0j}$  is a wave vector of each interacting wave,  $\Delta$  is the Laplace operator. The equations (2.62) – (2.64) describe the propagating electric fields simultaneously as beams and as pulses, and their nonlinear terms allow describing their interaction in spatial and time domain.

If the spectra of interacting pulses are broad, the equations should also include higher orders of dispersion. This can be done while recalling the equations

(2.51) and (2.52) and including the first member of (2.52) in the wave vector term  $\delta k$  :

$$k(\Omega) = k(\omega_c) + \frac{dk}{d\Omega}_{\omega=\omega_c} (\Omega - \omega_c) + \delta k , \quad (2.65)$$

where  $\delta k$  includes higher terms of the expansion:

$$\delta k = \frac{1}{2} \frac{d^2 k}{d\Omega^2}_{\omega=\omega_c} (\Omega - \omega_c)^2 + \frac{1}{6} \frac{d^3 k}{d\Omega^3}_{\omega=\omega_c} (\Omega - \omega_c)^3 + \dots . \quad (2.66)$$

The (2.66) equation is used as a wave's  $k$  vector and propagation is analyzed in the reference frame of the carrier frequency.

It is clear that the nonlinear optics phenomena described by the equations are highly complex, and can be solved analytically only in the simplest cases. In order to understand and explain the measured optical parametric oscillator characteristics in the real world, the tools of numerical simulation should be used. Such multipass time- and space-domain systems are never accurately described by purely analytic methods. Nonlinear crystal is the location of a large number of simultaneous physical effects: parametric amplification, pulse dispersive propagation, beam diffraction, extraordinary beam walk-off, linear and nonlinear absorption, pulse and beam self- and cross- phase modulation, cascaded phase matching effects, parasitic non-phase matched nonlinear conversion effects. In addition to the crystal, the resonator contains a plethora of other physical effects that have to be accounted for: diffraction, losses in optical elements, dispersive broadening, pulse delay by cavity mirror translation. If all these effects are included, the simulation model becomes numerically costly, hard to implement and even harder to interpret. Therefore, analyzing the OPO operation should be done with the most important effects which can be prioritized by comparing the distances under which the effects are pronounced.

OPO can be analyzed by 4 different approaches each including different experimentally observable effects: 1) plane wave and monochromatic wave approach (2.14) - (2.16) system of linear equations; 2) plane wave and pulse approach, described by the equations (2.55) - (2.57); 3) Beam and monochromatic wave approach, described by the equations (2.62) - (2.64) with time domain derivatives set to 0. Beam and pulse, described by the system of equations (2.62) - (2.64). We will further discuss the validity and applicability domains for each of these simplified models, their advantages and shortcomings.

### 2.2.1 Plane and monochromatic wave model

Numerical solution of the equations (2.14) – (2.16) is a task of finding the complex electric field amplitude and phase change while light propagates through the nonlinear crystal. In this model, the spectrum of the propagating field is composed of one component (monochromatic wave), the spatial mode also has only one frequency component (plane wave), and the dispersive and diffractive light nature is ignored. This model is suitable for narrow bandwidth pulses when dispersive broadening is only weakly pronounced, for instance, in the case of nanosecond pulses and picosecond pulses with short interaction lengths. An approximation in spatial domain leads to the requirement that interacting beams should be large and have narrow spatial frequency content, so that diffraction could be ignored. A single beam resonator is simulated by providing feedback to only one of the interacting beams. After each single pass, the signal field is multiplied by the loss coefficient and is returned back to the crystal. The calculation is repeated again with new pump field and new idler field starting from noise. The system of equations (2.14) - (2.16) is solved using a finite difference method with appropriate step size  $\Delta z$  and initial conditions at the start of the crystal  $z = 0$ . The calculation step size should be small enough so that the electric field phase change after a step is not larger than  $\sim \pi/10$ , which leads to a very gradual increase of the phase while fields propagate. If interaction is strong with strongly pronounced pump depletion and abruptly changing phase, the step size  $\Delta z$  is decreased until the calculation results no longer depend on the step size  $\Delta z$ . A standard technique for solving such a system of linear differential equations is 4<sup>th</sup> order Runge-Kutta method [48]. The examples of the OPO simulated using this approach are given in [49].

## 2.2.2 Plane wave and pulse model

In order to account for the dispersive broadening, a system of equations (2.55) - (2.57) should be solved. In this case, the spatial mode is described as an infinite plane wave, while in time domain it is a packet of monochromatic waves, a pulse. This model is well suited for large beam diameters when beam diffraction can be ignored (or short interaction lengths). In the field of short pulse OPO numerical modelling, this is the most popular model because it is the fastest approach. Nevertheless, it has its shortcomings: it fails, if the spatial spectrum is broad (high convergence or divergence angles) or there is a significant walk-off of extraordinary beam.

The system of linear equations (2.55) - (2.57) is solved with „split-step“ method based on separation of the equation into linear and nonlinear parts [50]. We will focus on the method for one of the equations of the system:

$$\frac{\partial E_1}{\partial z} = (\hat{D} + \hat{N}) E_1, \quad (2.67)$$

where the linear term:

$$\hat{D} = -v_{12} \frac{\partial}{\partial t} + \frac{i}{2} k_1'' \frac{\partial^2}{\partial t^2}, \quad (2.68)$$

and the nonlinear term:

$$\hat{N} = -i\sigma_1 \frac{E_3^* E_2}{E_1} e^{-i\Delta k z} - i\beta_1 \left( |E_1|^2 + \gamma_{12} |E_2|^2 + \gamma_{13} |E_3|^2 \right). \quad (2.69)$$

The solution to the equation (2.69) could be written as:

$$E_1(t, z) = E_{10} \exp((\hat{D} + \hat{N})(z - z_0)), \quad (2.70)$$

where  $E_{10} = E_1(t, z_0)$ . A notation is used  $h = z - z_0$  and an exponent of the equation (2.70) is expanded with a Taylor series:

$$\exp((\hat{D} + \hat{N})h) = 1 + (\hat{D} + \hat{N})h + \frac{(\hat{D}^2 + \hat{D}\hat{N} + \hat{N}\hat{D} + \hat{N}^2)h^2}{2} + \dots \quad (2.71)$$

On the other hand, the product of both exponents leads to:

$$\exp(\hat{D}h)\exp(\hat{N}h) = 1 + (\hat{D} + \hat{N})h + (\hat{D}^2 + 2\hat{D}\hat{N} + \hat{N}^2)\frac{h^2}{2} + \dots \quad (2.72)$$

If operators  $\hat{D}$  and  $\hat{N}$  commute, the expressions (2.71) and (2.72) are equal to each other within  $o(h^2)$ . If  $h$  is small, an approximate relationship holds:

$$\exp((\hat{D} + \hat{N})h) = \exp(\hat{D}h)\exp(\hat{N}h). \quad (2.73)$$

A solution (2.70) could be rewritten as:

$$E_1(t, z_0 + h) = E_1(t, z_0)\exp(\hat{D}h)\exp(\hat{N}h). \quad (2.74)$$

A part of the solution with the nonlinear operator could be rewritten as:

$$E_1'(t, z_0 + h) = E_1'(t, z_0)\exp(\hat{N}h). \quad (2.75)$$

An expression (2.75) is a solution to such an equation:

$$\frac{\partial E_1'}{\partial z} = \hat{N} E_1'. \quad (2.76)$$

Similarly, an expression  $E_1(t, z_0 + h) = E_1(t, z_0)\exp(\hat{D}h)$  is a solution to a linear operator equation:

$$\frac{\partial E_1}{\partial z} = \hat{D} E_1. \quad (2.77)$$

Linear operator consists of time-domain derivatives so it could be written more conveniently in frequency domain:

$$\hat{D} = -iv_{12}\omega - \frac{i}{2}k_1''\omega^2. \quad (2.78)$$

And the solution to (2.77) equation could be written as:

$$S_1(\omega, z_0 + h) = S_1(\omega, z_0) \exp\left(\left(-iv_{12}\omega - \frac{i}{2}k_1''\omega^2\right)h\right). \quad (2.79)$$

Using an inverse Fourier transform an electric field can be calculated  $E_1(t, z_0)$  and it is used as an initial value while solving the nonlinear equation (2.76). The same algorithm could be used for all three equations (2.55) - (2.57) to obtain the initial conditions for the signal, idler and pump waves. Afterwards, the system of differential equations based on (2.69) and (2.76) is solved and the values of electric field are found at each time instance [51]. A solution could be implemented by the 4<sup>th</sup> order Runge-Kutta finite difference method [48]. The examples where OPO simulation is carried out with plane waves and pulses are presented in [50 - 53].

### 2.2.3 Beam and monochromatic wave model

If the diameters of interacting beams are small and the spatial domain frequency spectrum is broad, the spatial distribution has to be taken into account. In this case, the pulses are considered long in the time domain and their spectrum is nearly monochromatic. Solving in Cartesian coordinate system allows accounting for such effects as extraordinary beam walk-off and resonator astigmatism. Working in XY plane requires using two dimensional Fourier transform, which is more computationally expensive compared to the standard one dimensional one [54, 55].

The system of equations (2.62) - (2.64) is solved without the time derivatives because pulses are long and time-domain amplitude changes are small (in other words, time derivatives are set to zero). Self- and cross- phase modulation terms describe beams self- and cross- induced focusing. The system of equations in the spatial domain [42] reads:

$$\begin{aligned} \frac{\partial E_1}{\partial z} + \frac{i}{2k_1} \left( \frac{\partial^2 E_1}{\partial x^2} + \frac{\partial^2 E_1}{\partial y^2} \right) &= -i\sigma_1 E_2^* E_3 e^{-i\Delta kz} \\ -i\beta_1 E_1 \left( |E_1|^2 + \gamma_{12} |E_2|^2 + \gamma_{13} |E_3|^2 \right), \end{aligned} \quad (2.80)$$

$$\begin{aligned} \frac{\partial E_2}{\partial z} + \frac{i}{2k_2} \left( \frac{\partial^2 E_2}{\partial x^2} + \frac{\partial^2 E_2}{\partial y^2} \right) &= -i\sigma_2 E_1^* E_3 e^{-i\Delta k z} \\ -i\beta_2 E_2 \left( |E_2|^2 + \gamma_{12} |E_1|^2 + \gamma_{23} |E_3|^2 \right), \end{aligned} \quad (2.81)$$

$$\begin{aligned} \frac{\partial E_3}{\partial z} + \rho_3 \frac{\partial E_3}{\partial y} + \frac{i}{2k_3} \left( \frac{\partial^2 E_3}{\partial x^2} + \frac{\partial^2 E_3}{\partial y^2} \right) &= -i\sigma_3 E_1 E_2 e^{i\Delta k z} \\ -i\beta_3 E_3 \left( |E_3|^2 + \gamma_{13} |E_1|^2 + \gamma_{23} |E_2|^2 \right), \end{aligned} \quad (2.82)$$

where the third beam is assumed to be extraordinarily polarized with the spatial walk-off accounted for by the angle  $\rho_3$ . Numerical calculation should be performed with the ‘‘split-step’’ method, where the linear operator in spatial frequency domain is:

$$\hat{D} = i \frac{k_x^2 + k_y^2}{2k_{01}}, \quad (2.83)$$

and the nonlinear operator is written as:

$$\hat{N} = -i\sigma_1 \frac{E_2^* E_3}{E_1} e^{-i\Delta k z} - i\beta_1 \left( |E_1|^2 + \gamma_{12} |E_2|^2 + \gamma_{13} |E_3|^2 \right). \quad (2.84)$$

Discretizing crystal axial  $Z$  coordinate to  $N$  points with a step size of  $\Delta z$ , the following procedure is performed  $N$  times: a linear part is solved, (2.79) equation’s result in the spatial domain is used and inverse 2D Fourier transform is calculated, a field which has propagated a distance  $\Delta z$  is recovered. Afterwards, this field is used as an initial value to solve the nonlinear part of the equation with propagation distance  $\Delta z$ , Runge-Kutta method is used to solve it. 2D Fourier transform is carried out to return to the spatial domain spectrum representation. The same operation is done for all three interacting beams.

After a computation in crystal is performed, propagation in resonator is simulated. The simplest approach is solving the diffraction equation in spatial frequency domain. Resonator’s spherical mirrors are simulated using thin lens transfer function in real domain. After a complete resonator round trip, the fields are returned back to the crystal and the same system of differential equations is solved

again [54, 55]. As an example, OPO simulation with beam and monochromatic wave method is presented in [52].

If extraordinary beam walk-off and resonator astigmatism are small, spatial domain calculation can be carried out conveniently in the polar coordinate system. Splitting a space to points with steps  $\Delta r$  and  $\Delta\varphi$ , spatial grid is not uniform, increasing  $r$  leads to widening of the step size. Such a grid is a web like. If it is transformed to Cartesian coordinate system, the distances between points are not constant and the Fast Fourier Transform algorithm cannot be used (as it requires an uniform grid). Therefore, the diffraction part in a polar coordinate system should be solved with a finite difference method. A system of equations (2.62) - (2.64) is solved without time domain terms and using Laplacian operator in polar coordinate system. One of the equations could be written as:

$$\begin{aligned} \frac{\partial E_1}{\partial z} + \frac{i}{2k_{01}} \left( \frac{1}{r} \frac{\partial}{\partial r} \left( r \frac{\partial}{\partial r} \right) \right) E_1 = -i\sigma_1 E_2^* E_3 e^{-i\Delta k z} \\ -i\beta_1 E_1 \left( |E_1|^2 + \gamma_{12} |E_2|^2 + \gamma_{13} |E_3|^2 \right) \end{aligned} \quad (2.85)$$

The algorithm is solved with the “split-step” method but in this case the linear equation is solved with a finite difference method using non-implicit Crank-Nicholson scheme [48]. Linear part and its approximation:

$$\begin{aligned} \frac{\partial E_1}{\partial z} = -\frac{i}{2k_{01}} \left( \frac{1}{r} \frac{\partial E_1}{\partial r} + \frac{\partial^2 E_1}{\partial r^2} \right), \quad (2.86) \\ \frac{E_l^{j+1} - E_l^j}{\Delta z} = -\frac{i}{4k_{01}} \left( \frac{1}{r} \frac{E_{l+1}^{j+1} - E_{l-1}^{j+1}}{2\Delta r} + \frac{E_{l+1}^{j+1} - 2E_l^{j+1} + E_{l-1}^{j+1}}{\Delta r^2} \right. \\ \left. + \frac{1}{r} \frac{E_{l+1}^j - E_{l-1}^j}{2\Delta r} + \frac{E_{l+1}^j - 2E_l^j + E_{l-1}^j}{\Delta r^2} \right), \quad (2.87) \end{aligned}$$

where index  $l$  designates transversal  $r$  coordinate and index  $j$  designates axial  $z$  coordinate. At the boundaries of the transverse range  $r = 0$  and  $r = R$ , two separate equations are solved to account for  $1/r$  uncertainty and to account for absence of  $R + \Delta r$  point. In order to solve this equation numerically, terms  $E_0^{j+1}, \dots, E_R^{j+1}$

need to be found. This can be done with gathering the coefficients near the corresponding  $j+1$  members and using Thomas algorithm [48].

After solving the linear part, a nonlinear part is solved. Iterations are repeated till the beam diffracts through the entire crystal. After the crystal is passed, diffractive propagation in the resonator is solved further. Two different approaches could be used: spatial domain frequency can be calculated while using Hankel transform (expanding the field with Bessel functions) and using a propagator defined in equation (2.83). Another approach is using a Fresnel diffraction formula in the polar coordinate system. During the numerical simulations performed in this dissertation, it was noted that the second method is much more computationally efficient when wide angular spectrum has to be calculated after focusing elements of the resonator [56].

## 2.2.4 Beam and pulse model

In order to account for the spatial effects as well as the pulse intensity in the time domain, solutions of the equations (2.62) - (2.64) have to be calculated. A calculation in Cartesian coordinate system is based on the synthesis of the approaches described in the previous chapters (2.2.2 - 2.2.3). The same “split-step” method is used, but in this case the 3D Fourier transformation is performed in temporal and spatial domains simultaneously. The linear operator is described in a such way:

$$\hat{D} = i \left( \frac{k_x^2 + k_y^2}{2k_{01}} - v_{12}\omega - \frac{1}{2}k_1''\omega^2 \right). \quad (2.88)$$

The remaining analysis is carried out according to the procedures described in the sections (2.2.2 - 2.2.3)

Calculation in the polar coordinate system is based on the synthesis of the approaches described in the previous chapters (2.2.2 - 2.2.3). A linear part of the equation is Fourier transformed with  $E$  now denoting spectral electric field amplitude:

$$\frac{\partial E_1}{\partial z} = -\frac{i}{2k_{01}} \left( \frac{1}{r} \frac{\partial E_1}{\partial r} + \frac{\partial^2 E_1}{\partial r^2} \right) - v_{13} \frac{\partial E_1}{\partial t} + \frac{i}{2} k_1'' \frac{\partial^2 E_1}{\partial t^2}, \quad (2.89)$$

$$\begin{aligned} \frac{E_l^{j+1} - E_l^j}{\Delta z} = & -\frac{i}{4k_{0l}} \left( \frac{1}{r} \frac{E_{l+1}^{j+1} - E_{l-1}^{j+1}}{2\Delta r} + \frac{E_{l+1}^{j+1} - 2E_l^{j+1} + E_{l-1}^{j+1}}{\Delta r^2} + \frac{1}{r} \frac{E_{l+1}^j - E_{l-1}^j}{2\Delta r} \right. \\ & \left. + \frac{E_{l+1}^j - 2E_l^j + E_{l-1}^j}{\Delta r^2} \right) + \frac{1}{2} (E_l^{j+1} + E_l^j) \left( i\omega v_{l3} - i\frac{k''}{2}\omega^2 \right). \end{aligned} \quad (2.90)$$

Calculations in polar coordinate system use only one transversal coordinate, so the computational resources are saved and the solution is faster than the solution in Cartesian coordinate system. An example of full OPO field solution with a method of beam in Cartesian coordinate system and pulse is presented in [57].

In this dissertation, pulse model simulation in the time domain was carried out supporting soliton generation experiments described in chapters 4 to 6. The spatial domain was included phenomenologically, by reducing the calculation crystal length to the one limited by the spatial walk-off. In the spatial domain investigation described in chapter 7, the spatial domain numerical simulation was carried out in Cartesian coordinates without the reduction of the crystal length as it was not limited by the group velocity walk-off. The full spatial and time model described in this chapter was not used because of its computational inefficiency. The polar coordinate spatial domain model with a time domain could not be used as it excluded the resonator's astigmatism.

## 2.3 Cascaded Nonlinearity

The cascaded nonlinearity can be described as a two-step cascading interaction which includes the generation of the second harmonic wave  $\omega + \omega = 2\omega$ , followed by the reconstruction of the fundamental wave through the down-conversion frequency mixing process  $2\omega - \omega = \omega$ . Respectively, the first sub-process is responsible for the generation of the second harmonic field, with the most efficient conversion observed at  $\Delta k = 0$ , while the second sub-process, also called cascading, can be associated with an effective intensity-dependent change of the phase of the fundamental harmonic, which is similar to that of the cubic nonlinearity [58]. This process is called quadratic cascaded nonlinearity and is observed in crystals which have a non-vanishing quadratic nonlinear susceptibility  $\chi_{ijk}^{(2)}$ . Cascaded SHG / DFG occurs when the nonlinear conversion process is strongly phase mismatched. In the case of SHG, due to the  $\Delta k \neq 0$  up-conversion after one coherence length  $\pi/|\Delta k|$  to the second harmonic is followed by the reverse process of down-conversion to the fundamental wave after the coherence length. On continued propagation, the macroscopic picture shows that second harmonic is cyclically generated and back-converted, hence producing a cascade of nonlinear effects. During this process, the fundamental wave essentially experiences a nonlinear phase shift due to the difference in phase velocities (this is a consequence of  $\Delta k \neq 0$ ), and the magnitude and sign of the phase shift depends on the phase mismatch  $\Delta k$ : the sign of the nonlinear phase shift can be controlled by the sign of  $\Delta k$ . In the meantime, the magnitude of such phase shift is inversely proportional to the phase mismatch. If the phase mismatch is large enough, this nonlinear phase shift behaves as a Kerr effect with controllable nonlinearity [45, 59].

The nonlinear phase  $\varphi_{NL}$  can be extracted from the coupled nonlinear equations (2.14) to (2.16), as the solutions of the electric field  $E_N(\omega_N) = E_{N0}(\omega_N)e^{i\varphi_{NL}}$ . Only under very restrictive conditions is there a linear dependence of  $\varphi_{NL}$  on either the distance traversed in the sample or on the incident irradiance (and hence the equivalence to the electronic Kerr  $\chi^{(3)}$ ). An example of the variation of  $\varphi_{NL}$  with distance is shown in Fig. 2.3A, whereas Fig. 2.3B shows

corresponding fundamental transmission. Fig. 2.3A shows linear variation of phase with distance only for large phase mismatch and / or small phase shifts. The increment of the nonlinear phase occurs primarily during the cycle in which power flows back from the harmonic into the fundamental so the phase changes stepwise [45].

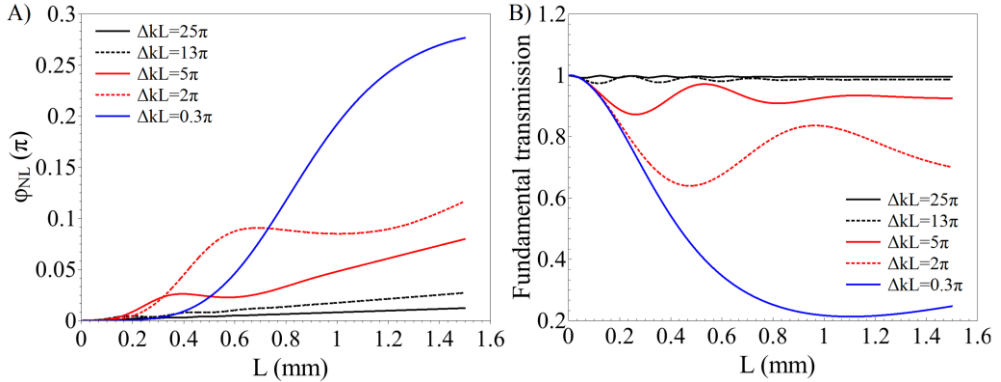


Fig. 2.3. A) Nonlinear phase dependence on the traversed distance in the crystal. B) Fundamental transmission dependence on the propagated crystal length. In both panels, phase mismatch parameter is varied. The simulated pulse duration is 120 fs in BBO with  $\lambda_{\text{fundamental}}=860$  nm.

The dependence of the nonlinear phase  $\varphi_{NL}$  versus increasing input intensity is shown in Fig. 2.4. Note that there is an intensity range in which the nonlinear phase shift is linear in intensity. Therefore, it is sensible to discuss cascading as leading to an effective third order nonlinearity and effective nonlinear refractive index coefficient  $n_2^{\text{eff}}$ . It is clear that the maximum phase shift, where this approximation is valid depends on the detuning: the larger the  $\Delta kL$ , the larger the range of intensities where this concept is valid.

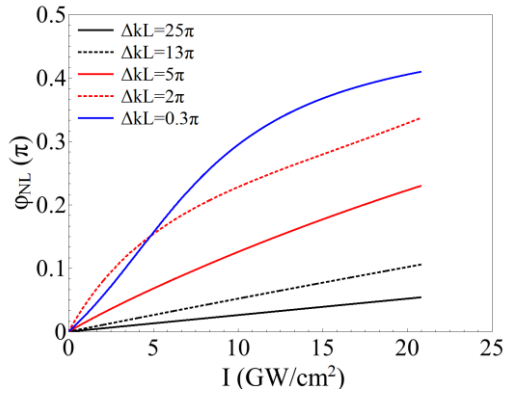


Fig. 2.4. Nonlinear phase as a function of the input intensity at varying levels of phase mismatch. The simulated pulse duration is 120 fs in BBO with  $\lambda_{\text{fundamental}}=860$  nm, an intensity is increased with varying pulse energy.

As indicated in the Fig. 2.5A, the net phase shift depends on the phase mismatch, commonly called the SHG detuning. Just by adjusting the phase matching, the magnitude and the sign of the effective nonlinearity can be varied.

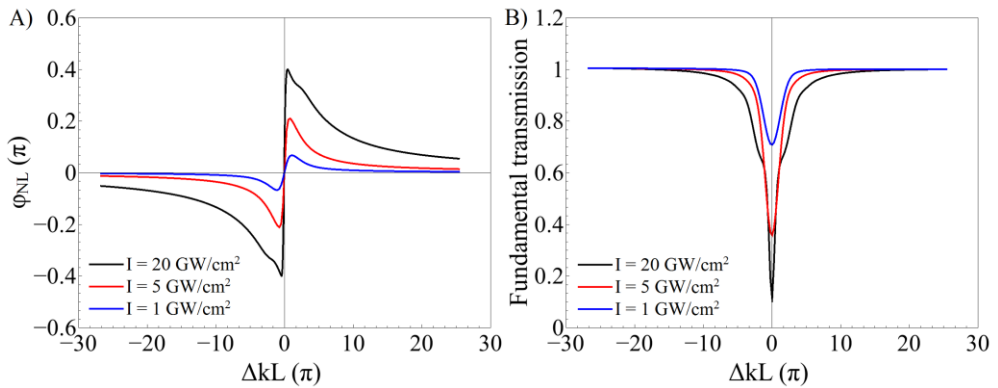


Fig. 2.5. A) Nonlinear phase dependence as a function of phase mismatch. B) Fundamental transmission as a function of the phase mismatch. In both panels, incident intensity is varied. The simulated pulse duration is 120 fs in BBO with  $\lambda_{\text{fundamental}}=860$  nm.

There is an intensity dependence to the detuning needed for maximum phase shift: in the small depletion limit, this maximum occurs at  $\Delta kL \sim \pm\pi$ . The dispersion in the low depletion limit is an indicator of refractive index dispersion and is linked to the coherence length. As shown in Fig. 2.5B, the „price“ for obtaining large phase shifts is effectively the „loss“ of the fundamental throughput to second harmonic. In fact, the connection between the phase shift and the loss to SHG has been shown to satisfy the Kramers-Kronig relations in the limit of weak depletion [45, 60].

The effect of pulse duration of the nonlinear phase dependence on the phase mismatch is shown in Fig. 2.6A. The corresponding fundamental transmission is shown in Fig. 2.6B. It can be seen that the oscillations of the nonlinear phase become more pronounced with an increase of pulse duration. This is a consequence of the smoothing of the phase shift oscillations over the broad spectrum of the short pulse.

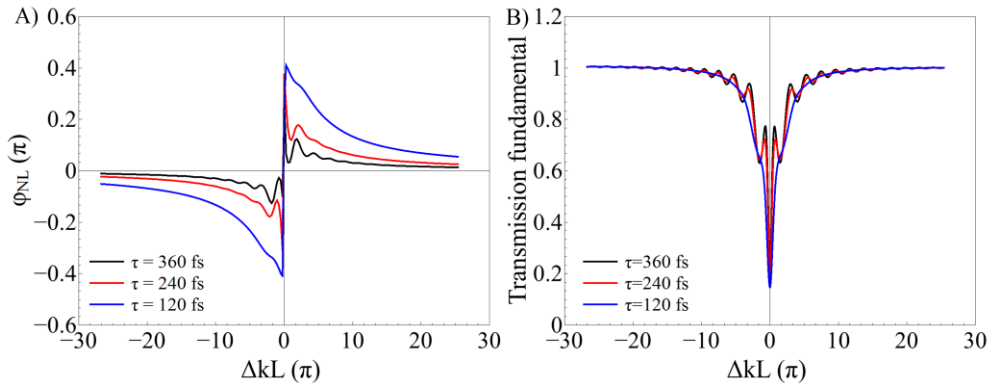


Fig. 2.6. A) Nonlinear phase dependence on the phase mismatch. B) Fundamental transmission dependence on the phase mismatch. In both panels incident pulse duration is varied with constant intensity  $I=20$  GW/cm<sup>2</sup> in BBO with  $\lambda_{\text{fundamental}}=860$  nm.

In the limit of negligible depletion of the fundamental wave, it is possible to deduce a simple expression for the effective nonlinearity  $n_2^{\text{eff}}$  in the case of SHG [59]:

$$n_2^{eff} = -\frac{2\omega_1 d_{eff}^2}{c^2 \varepsilon_0 n_1^2 n_2 \Delta k}. \quad (2.91)$$

As is evident from the expression, the resulting nonlinear refractive index is proportional to the square of the quadratic nonlinearity  $d_{eff}$  and is inversely proportional to the SHG phase mismatch. Its sign can be controlled by the sign of the phase mismatch: for  $\Delta k > 0$  it results in self-defocusing, while for  $\Delta k < 0$  it causes self-focusing.

Interestingly enough, in the case of difference frequency generation (DFG) the cascaded nonlinearity induced nonlinear phase shifts are opposite to the SHG case. The ideas for the explanation of this difference in behavior can be gleaned from the earlier work of Conti, di Trapani and Valiulis [61, 62].

Conti *et al* have shown that in a non-phase matched case, the system of nonlinear coupled equations can be simplified using perturbation methods and solved exploiting a method of multiple scales [63, 64]. If the phase mismatch  $\Delta k$  is much larger than zero, a small parameter  $\varepsilon$  can be introduced, given by  $\varepsilon = \Delta k^{-1}$ . The electric fields are expanded in power series of this small parameter  $\varepsilon$ :

$$E_s = A + \varepsilon A_1 + \varepsilon^2 A_2 + \dots, \quad (2.92)$$

$$E_p = B + \varepsilon B_1 + \varepsilon^2 B_2 + \dots. \quad (2.93)$$

Inserting these expansions into coupled nonlinear equations (2.14) – (2.16) (in the degenerate second harmonic generation case, with scaled variables), yields the following equations for the leading order envelopes  $A$  and  $B$  which correspond to the fundamental (signal / idler) and the second harmonic (pump) electric fields respectively:

$$\frac{\partial A}{\partial z} - i \frac{1}{2\Delta k} |A|^2 A + i \frac{1}{\Delta k} |B|^2 A = 0, \quad (2.94)$$

$$\frac{\partial B}{\partial z} + i \frac{1}{\Delta k} |A|^2 B = 0. \quad (2.95)$$

The term  $|A|^2 A$  is a self-induced phase modulation term originating from the cascaded phase matching. It describes the nonlinear phase shift acquired during steps

of cascaded photon processes, involving up-conversion to  $2\omega$  followed by back-conversion to  $\omega$ . Conti *et al.* have shown that there is an additional term to the signal/idler equation (2.94) if the pump electric field is sufficiently intense, as evident from expression  $|B|^2 A$ . The physical process consists of two successive difference frequency generation processes  $\omega = 2\omega - \omega$ , which are responsible for the cross-induced phase shift at signal/idler. The sign of the produced phase shift is different as evident from equation (2.94). The relative intensities of interacting beams determine which process is dominating – either self-induced phase modulation term during sum frequency generation  $|A| \gg |B|$ , or cross-induced phase modulation term during difference frequency generation  $|B| \gg |A|$ . These effects help to explain the sign differences of phase modulation observed in DFG and SHG experimental cases.

## 2.4 Time domain solitons in OPO

Positive / negative nonlinearity and the corresponding negative / positive resonator group delay dispersion leads to the soliton formation. For a Gaussian-shaped pulse propagating inside the dispersive nonlinear material, the positive material's dispersion leads to a pulse broadening and a "chirp" of the pulse. The negative dispersion induced by a prism or grating pair could be used to compensate the positive material's dispersion or the self-phase modulation induced "chirp". The "chirp" by negative dispersion means time delay of the spectral components so that the blue spectral components are at the leading edge and the red spectral components are at the trailing edge of the pulse. The change of the pulse "chirp" in time or, in other words, dispersion-induced frequency modulation, can be calculated by the time derivative of the "chirp" parameter, which itself is a time derivative of pulse phase [42]:

$$\alpha_D(\omega) = \frac{\partial}{\partial t} \left( \frac{\partial \varphi_D}{\partial t} \right) = \frac{4k''}{\tau_0^4} L, \quad (2.96)$$

where  $L$  is the propagation length,  $\tau_0$  is the duration of unchirped pulse and  $k''$  is the group velocity dispersion of the medium, expressed as the second derivative of the wave vector.

The self-phase modulation-induced frequency modulation can be calculated in a similar manner:

$$\alpha_{SPM}(\omega) = \frac{\partial}{\partial t} \left( \frac{\partial \varphi_{SPM}}{\partial t} \right) = -\frac{2\pi}{\lambda} n_2 \frac{\partial^2 I}{\partial t^2} L. \quad (2.97)$$

Summing both relations for the zero net modulation in the Gaussian-shaped pulse center  $\alpha_D + \alpha_{SPM} = 0$ , we find a condition for a chirp-free propagating pulse:

$$I_p \tau_0^2 = \frac{\lambda k''}{\pi n_2}, \quad (2.98)$$

where  $I_p$  is the peak intensity. This is the formula for the first order soliton ( $N_{\text{soliton}} = 1$ ) which shows that both the material and nonlinearity frequency modulations can

approximately compensate each other if the material and pulse properties satisfy the underlying soliton equation.

An integer number of the soliton order parameter  $N_{soliton}$  is given by square root of ratio of dispersive length  $L_D$  to nonlinear length  $L_{NL}$ . Dispersive length is defined as a distance, after which the pulse duration increases by a factor of  $\sqrt{2}$ . Nonlinear length is defined as a distance, after which the accumulated nonlinear phase reaches 1 radian. If the  $N_{soliton} < 1$ , the pulse evolution is dominated by dispersion, if the  $N_{soliton} > 1$ , the pulse evolution is dominated by the self-phase modulation. The exact balance with  $N_{soliton} = 1$  leads to the fundamental soliton which has a stable pulse and spectrum shape when propagating. Higher integer order  $N_{soliton} > 1$  solitons show periodic time and frequency domain oscillations with a soliton period. The pattern of the oscillations becomes more complicated and dominated by the SPM with increasing soliton order  $N_{soliton}$ . The soliton order equation is given by [47]:

$$N_{soliton} = \sqrt{\frac{L_D}{L_{NL}}} = \frac{\tau_0 (k_{eff}'' )^{-1/2}}{\left( \frac{n_2^{eff} \omega_0 P_0}{c A_{eff}} \right)^{-1/2}}, \quad (2.99).$$

where  $\tau_0$  is pulse duration,  $P_0$  is the intracavity peak power,  $A_{eff}$  is the effective beam area,  $c$  – the speed of light in vacuum,  $\omega_0$  is angular frequency, and  $k_{eff}''$  is the group velocity dispersion of the resonator, normalized to crystal length. In the case of two crystals, the crystal lengths are averaged using their effective nonlinearities as weighing coefficients. From the equation (2.99), the  $N$ -th order soliton FWHM duration and the average power in the cavity with the propagating soliton can be calculated [19, 65]:

$$\tau_N = - \frac{\lambda k_{eff}'' N_{soliton}^2 A_{eff} f}{0.57 \pi n_2^{eff} P_{ave}}, \quad (2.100)$$

$$P_N = - \frac{\lambda k_{eff}'' N_{soliton}^2 A_{eff} f}{0.57 \pi n_2^{eff} \tau}, \quad (2.101)$$

where,  $\lambda$  is the signal wavelength and  $f$  – pulse repetition rate. Experimentally measured values of the output average power, pulse duration and numerically calculated effective nonlinearity are used in the calculation of soliton duration and

soliton power given by equations (2.100) and (2.101). Using the numerical modelling results, nonlinear phase is extracted and soliton order given by equation (2.99) is calculated. When the nonlinearity increases, the nonlinear length decreases and an increasing order of soliton can be supported by the cavity as given by the soliton order equation.

In this dissertation, two ways of soliton generation were experimentally observed: the state-of-the-art method of soliton generation with positive material nonlinearity and negative intracavity dispersion; a novel method of soliton generation with negative material cascaded nonlinearity and positive intracavity dispersion. The results obtained with these methods are discussed in the chapters 3-6.

## 2.5 OPO resonator stability

The ABCD matrix tool is an invaluable tool in analyzing paraxial beam propagation and resonator stability. Its complete derivation is given in [66, 67]. If resonator's round trip matrix is analyzed, a condition of the stable resonator and pass-to-pass bound ray position is given by the following inequality:

$$-1 \leq \frac{A+D}{2} \leq 1. \quad (2.102)$$

Here, A is the resonator's round trip matrix (1, 1) element and D is the resonator's round trip matrix (2, 2) element. Even though there are many ways to design an optical resonator, the procedure of finding its stability is always the same - multiplying the transfer matrices of resonator's optical elements and calculating the stability as given by equation (2.102). A principal scheme of a resonator used throughout the experiments described in this dissertation is shown in Fig. 2.7. The nonlinear crystal is represented as an intensity dependent nonlinear lens. The dependence of the calculated stability parameter on the distance between the spherical mirrors of the resonator is shown in Fig. 2.8.

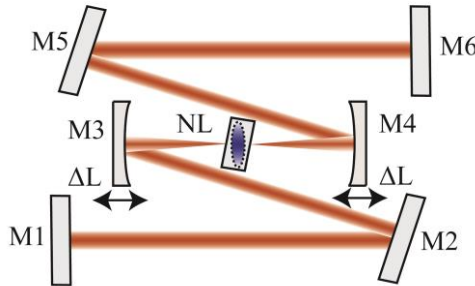


Fig. 2.7. Example Z-folded resonator with plane mirrors M1, M2, M5, M6 and curved mirrors M3, M4 on linear translation tables. The nonlinear crystal NL is represented as a nonlinear lens.

The red zone indicates the stability range where the resonator is stable – physical mirror separation distances outside these boundaries lead to an unstable resonator which does not form pass-to-pass stable resonator’s mode. The stability range could be split in two zones with different beam sizes in the crystal and at output coupler. The 1<sup>st</sup> zone is defined as the one having the stability parameter change from 1 to -1 (the physical mirror separation from 92 mm to 103 mm). The 2<sup>nd</sup> zone is defined as the one having the stability parameter change from -1 to 1 (the physical mirror separation from 103 mm to 116 mm).

The dotted lines indicate the stability parameter’s dependence when thin-lens is inserted intracavity with focusing power of  $D \sim 50 \text{ m}^{-1}$ . This simulates nonlinear focusing effect to resonator’s stability, even though the twice larger value of  $D \sim 50 \text{ m}^{-1}$  is used than numerically simulated in the dissertation chapter 7. The larger value allows showing the influence of the lens on a larger scale. The inclusion of the lens shifts the resonator stability range and separates the two stability zones. If continuously varying lens is inserted intracavity with fixed physical mirror distances, the stability parameter will change and this will limit the operation of the device. This is exactly the case if a nonlinear focusing occurs in an OPO crystal. When OPO generation starts and output power saturates - peak power is increased from 0 to the 400 kW after a number of round trips, and the first pulses “see” different resonator’s stability compared to the steady state ones [70].

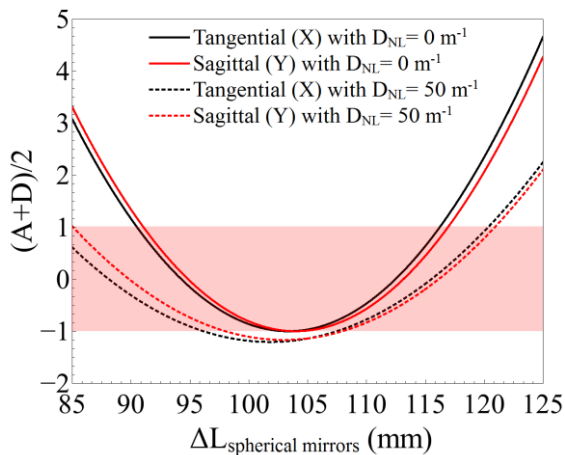


Fig. 2.8. The calculated tangential (X) and sagittal (Y) resonator stability parameter  $(A+D)/2$  dependence on the distance between resonator’s spherical mirrors. The dashed lines indicate the stability parameter with thin-lens power  $D=50 \text{ m}^{-1}$  included in the location of the crystal. The red zone indicates the spherical mirror separation distance where resonator is stable.

If the resonator's roundtrip matrix is known, the ABCD parameters can as well be used for calculating the Gaussian beam parameters. Round trip matrix calculation starting from each element of the resonator allows finding the complex beam parameter  $q$  at those elements. The stability condition is the requirement that the field distribution in the cavity reproduces its relative shape and phase after a round trip through the system. It can be written mathematically as follows:

$$q = \frac{Aq + B}{Cq + D}, \quad (2.103)$$

with complex beam parameter given as:

$$\frac{1}{q} = \frac{1}{R} - j \frac{\lambda_0}{\pi \omega^2}, \quad (2.104)$$

where  $R$  and  $\omega$  are Gaussian beam curvature radius and spot size respectively.

Both these approaches allow calculating the spot sizes in the OPO cavity and the stability ranges where a cavity is stable and generation could be observed. Calculation gets a bit more challenging if the parameters of optical components depend on the strength of the propagating electric field. A useful comparison with thermal lensing can be made: in laser resonators, the thermal lens depends on the mode size in the active element, and the mode size, in turn, depends on the thermal lens. The first approximation is calculating "cold" laser resonator mode size at active element and using the calculated mode size to derive element's thermal focal length. A parabolic refractive index approximation can be used to derive the thermal focal length, as given by [68]:

$$f_{\pi L} = \frac{2\kappa \pi \omega_0^2}{dn/dT P_{\text{heat}}}, \quad (2.105)$$

where  $\kappa$  is material's heat conductivity,  $dn/dT$  is material's refractive index dependence on temperature coefficient,  $\omega_0$  is a mode waist size at the active element and  $P_{\text{heat}}$  is absorbed thermal power/ Inserting the "cold" resonator's mode size into the equation (2.105), allows calculating thermal lens value, which in thin lens approximation can be used with a lens matrix to calculate "hot" resonator's mode sizes.

Similarly, the resonator mode sizes with Kerr lens-like nonlinear focusing / defocusing element can be calculated. A parabolic refractive index approximation can be used to derive the nonlinear focal length, as given by [67]:

$$f_{NL} = \frac{\pi \omega_0^4}{8P n_2 L}, \quad (2.106)$$

where  $P$  is the pulse peak power,  $\omega_0$  is a mode waist size at the element,  $n_2$  is the nonlinear refractive index, and  $L$  is the thickness of the material. The origin of both thermal and nonlinear focusing is a spatial phase gradient throughout the mode. In parabolic approximation, the phase gradient depends on the maximum phase shift at the center of the mode. It is also proportional to the square of the mode waist size at the active element. The maximum phase shift in thermal lens depends on  $\kappa$ ,  $dn/dT$  and  $P_{\text{heat}}$ . In the case of Kerr lens, the peak phase shift depends on peak intensity  $P/\pi \omega_0^2$  and material nonlinearity  $n_2$ . Hence, the nonlinear lens has a fourth power dependence on the mode size compared to the square power law of the thermal one. Thus, precise mode size calculation is required in order to correctly evaluate the nonlinear focal length.

On the other hand, as shown by Magni *et al.* [69], the variation range of the active element's focusing power  $\Delta 1/f$  which leads to a stable resonator is related to the mode size at the active element :

$$\left| \Delta \frac{1}{f} \right| = \frac{2\lambda}{\pi} \frac{1}{\omega_0^2}. \quad (2.107)$$

The equation shows that smaller resonator waist size at the active element leads to the active element focusing / defocusing insensitive resonator. This is the main reason why increasing the beam waist in the laser crystal does not prevent the thermal lens from shifting the laser resonator out of the stability range. The dependencies of thermal lens power and the stable zone width on the mode size cancel each other because they have exactly opposite square law relationships shown in equations (2.105) and (2.107).

The OPO case would make the mode size scaling even harder, as the fourth power dependence of nonlinear focal length would dominate the second power dependence of resonator's sensitivity to lensing. Luckily, the nonlinear refraction index of commonly used OPO crystals is low enough to reach focusing the powers

of  $D \sim 20 \text{ m}^{-1}$  with  $\sim 50 \text{ }\mu\text{m}$  spot size and  $\sim 400 \text{ kW}$  of peak output power [70]. The thermal lenses of laser resonators with Yb-doped slab type medium reach  $D \sim 20 \text{ m}^{-1}$  with  $\sim 150 \text{ }\mu\text{m}$  spot size and  $\sim 4 \text{ W}$  of average output power [71]. Three times smaller mode of OPO resonator makes the OPO resonator  $\sim 10$  times less sensitive to the change of the focal length compared to the laser resonator, as indicated by the equation (2.107).

Analogously to the laser resonators, the mode size in optical parametric oscillators can also be calculated in two step approach. The “cold” resonator involves stability calculation without the additional nonlinear lens. The retrieved mode size is inserted into the equation (2.106) and the nonlinear focal length is calculated. The “hot” resonator’s stability calculation requires inserting the nonlinear focal length into thin lens matrix and the resonator’s stability is calculated.

In this dissertation, the spatial domain nonlinear focusing effects were experimentally observed and are discussed in chapter 7.

### **3 OPO with negative GDD**

The state-of-the-art femtosecond synchronously pumped optical parametric oscillators include intracavity group delay dispersion compensation [72 – 74]. The third order nonlinearity of nonlinear crystal is positive, therefore requiring negative dispersion in order to generate soliton-like pulses. This chapter explores the method of dispersion compensation using a prism pair and the manifestation of cascaded nonlinearity effects. The results reflect the first attempt to design and characterize an operational OPO using the second harmonic pump, while the cascaded nonlinearity induced effects were not obvious at the time of the study.

Parts of the material covered in this chapter have been published in publication P2 and presented in conference papers C1 and C2.

### 3.1 Experimental procedures

The optical setup used in the experiments is shown in Fig. 3.1. The optical parametric oscillator was pumped by the second harmonic of 3 W Yb:KGW oscillator. The used nonlinear crystal was LBO, crystal length was chosen based on a double group velocity mismatch length  $L_{gv\ walkoff} = 2\tau / (v_{FM}^{-1} - v_{SH}^{-1})$  between the pump  $\lambda_p = 516\text{ nm}$  and the signal wavelength of  $\lambda_s = 950\text{ nm}$ , as for this wavelength the mismatch is maximum ( $L_{gv\ 515nm/960nm} = 45\text{ fs/mm}$  and  $L_{gv\ 515nm/730nm} = 25\text{ fs/mm}$ ). The parametric interaction is Type 1  $e \rightarrow o + o$  carried out in XY plane, the crystal length is 5 mm LBO, the cut angles are  $\theta = 90^\circ$  and  $\phi = 11.6^\circ$ , both surfaces are coated with anti-reflection coatings with  $R < 0.5\%$  in the range of 750-950 nm and  $R < 1\%$  for a wavelength of 516 nm. The resonator mirrors are highly reflective in the range of 780 - 950 nm with  $R > 99.9\%$  and highly transmissive at 515 nm. The group delay dispersion of the mirrors in this range was designed to be negative, in order to compensate and surpass the positive dispersion of the crystal. In Fig. 3.2B a round trip group delay dispersion of the mirrors is shown measured by white light interferometer. As can be seen from the graph, the group delay dispersion is oscillating and is gradually decreasing if shifted to lower wavelengths. The pump oscillator is 3 W average power, 95 fs pulse duration, 76 MHz pulse repetition rate oscillator (Flint, Light Conversion), the used second harmonic crystal is 2.5 mm length LBO crystal with AR coatings. The generated second harmonic power reaches 1.7 W with a conversion efficiency of 57 %. The pulse duration calculated from the spectrum bandwidth is 80 fs. The fundamental harmonic is focused to the second harmonic crystal with 22  $\mu\text{m}$  radius at  $1/e^2$  level resulting in peak intensity of 64  $\text{GW/cm}^2$ . The generated second harmonic is focused to the OPO crystal through the spherical mirror, to the focus of 25  $\mu\text{m}$  radius at  $1/e^2$  level to match the resonating mode's radius. Producing a peak intensity of 37  $\text{GW/cm}^2$ . The resonator design is symmetrical Z form confocal resonator with spherical mirrors radius of curvature  $R = -100\text{ mm}$ . The OPO's resonator's length is matched to the resonator length of the pump oscillator to enable the synchronous pumping condition. The resonator end mirror M9 is put on a linear translational stage to allow finding the synchronous pumping condition.

Output coupler is replaced with an uncoated glass plate, this allows varying the output coupler reflection coefficient to experimentally probe the most optimal

output coupler reflection coefficient which can be calculated with Fresnel reflection formula. The optimal reflection coefficient is probed to be with  $R = 9\%$ .

The experiments are done in two parts: in the first part, the resonator is operated with a net negative group delay dispersion induced by chirped mirrors and without a prism pair. In the second part of the experiments, in order to vary the amount of the intracavity negative GDD, a prism pair (P1-P2) is inserted intracavity. The SF10 prism pair is used at Brewster's angle with prism apex to apex distance of  $l=200$  mm. Therefore, the net negative resonator group delay dispersion is induced by the chirped mirrors and an additional variable negative term is induced by a prism pair.

Average power of output radiation was measured using a power meter (Nova-2, Ophir) equipped with a thermopile detector (30(150)A-BB-18, Ophir). Radiation spectra were recorded using a spectrometer (STS-NIR, Ocean Optics), pulse durations were measured using a scanning autocorrelator (Geco, Light Conversion).

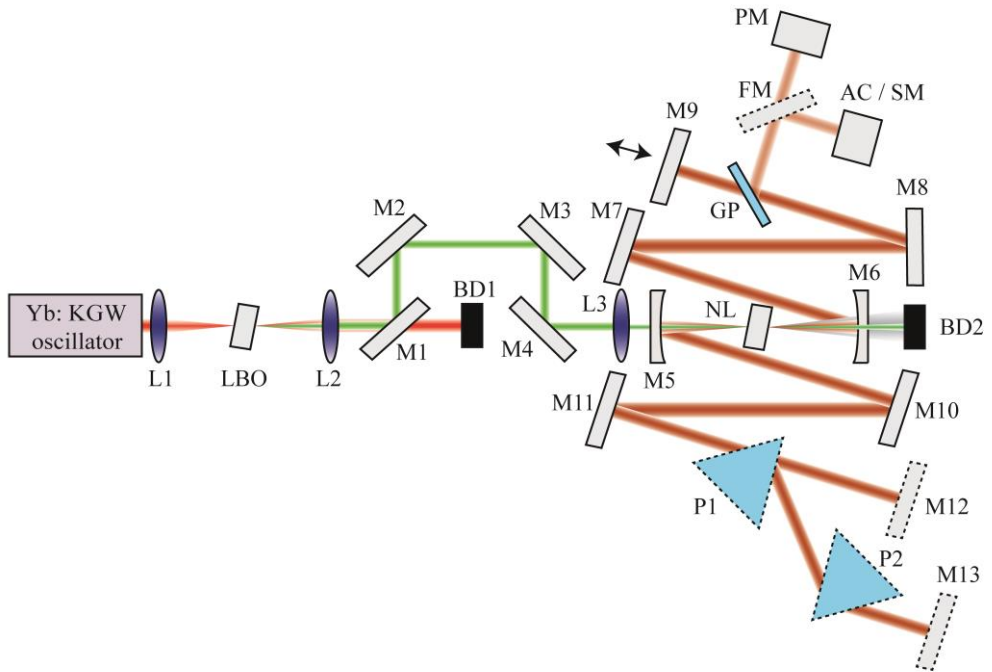


Fig. 3.1. Experimental setup. L1, L2, L3 – lenses for second harmonic generation, collimation and pump light focusing respectively. M1, M2, M3, M4 mirrors for pump light delivery with high transmission at fundamental wavelength. M5, M6 – curved resonator mirrors. M7, M8, M9, M10, M11, M12, M13 – plane resonator mirrors. M12 is used when resonator is operated without intracavity dispersion compensation by a prism pair. M13 is used when intracavity prism pair P1 / P2 is used for dispersion compensation. GP – uncoated glass plate used as an output coupler, NL – nonlinear crystal, BD1, BD2- beam dump, FM – flip mirror, PM – power meter, AC – autocorrelator, SM – spectrometer.

### 3.2 Results and discussion

Whenever nonlinear crystal is rotated to change the phase matching angle, the resonator is misaligned because of the refraction in the crystal. Therefore, every step of the wavelength change should be followed by alignment of the resonator which leads to a very cumbersome procedure. In order to prevent this, the central wavelength is changed by changing only the resonator length while keeping the nonlinear crystal angle fixed. This leads to parametric gain optimized at the center of the tuning curve with decreasing conversion efficiency if a wavelength is changed. The experiment was conducted in two steps: in the first part, wavelength was tuned without dispersive prisms. In the second part of the experiments, wavelength was tuned and the intracavity prism pair was adjusted to achieve the minimum pulse duration. In both cases the resonator group delay dispersion was negative.

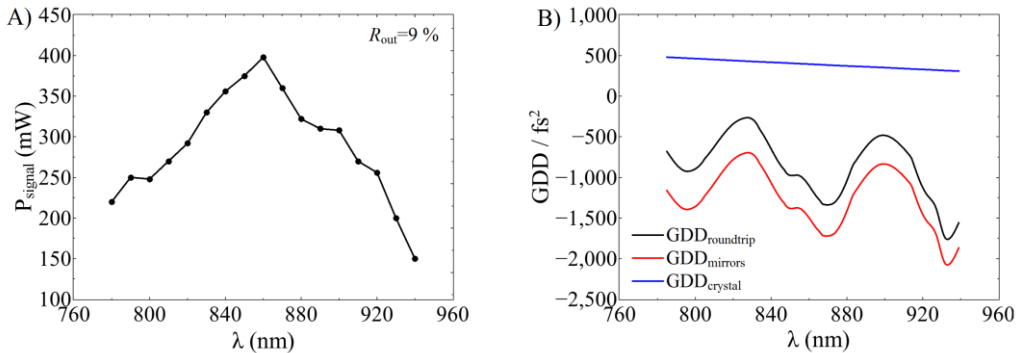


Fig. 3.2. A) Signal output power dependence on wavelength as the crystal angle is fixed at  $12.6^\circ$  and the wavelength is tuned by changing the cavity length. B) Crystal, mirrors and resonator round trip group delay dispersion dependence on the wavelength when resonator is operated without the prism pair.

The crystal angle was fixed at the  $\varphi = 12.6^\circ$ , the power tuning curve is shown in Fig. 3.2A. The power is calculated accounting for all the reflections from all four surfaces of the glass plate. A tuning curve is limited by the amplification

bandwidth of the crystal and the reflection bandwidth of the used resonator mirrors. The measured negative group delay dispersion of the mirrors is negative through the wavelength tuning range as shown in Fig. 3.2B.

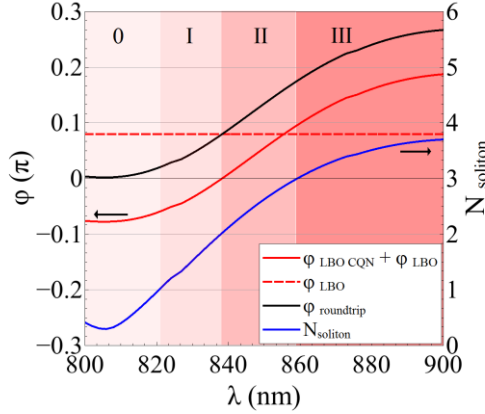


Fig. 3.3. Numerically calculated nonlinear phase and soliton number dependence on the signal wavelength with intracavity GDD  $\sim -1000 \text{ fs}^2$ . Negative CQN areas (0, I, II, III) colored with different red shades indicate wavelengths with negative CQN high enough to support soliton of corresponding order  $N = 0, 1, 2, 3$ . OPO crystal angle is fixed at  $12.7^\circ$  for optimal conversion efficiency to 860 nm.

The Fig. 3.3 shows numerically calculated nonlinear phase and soliton order dependence on the central signal wavelength. The soliton order was calculated from the equation (2.99) with a fixed dispersive length (with  $\sim -1000 \text{ fs}^2$  resonator GDD and  $\tau = 140 \text{ fs}$ ) and nonlinear length estimated from the nonlinear phase. The nonlinear phase was computed using the numerical model equations (2.59) to (2.61) by simulating a single pass through the OPO crystal with varying signal wavelengths. An input signal pulse is injected with approximate experimentally observed steady state OPO signal pulse parameters at the center of the tuning curve: pulse duration  $\tau = 140 \text{ fs}$  and intracavity average power  $P = 3.5 \text{ W}$ . As can be seen from the curve, the nonlinear phase is large enough to reach high order soliton threshold and only the wavelength range of 800-840 nm supports solitons below order of 2, as negative CQN compensates crystal material positive nonlinearity. As the used crystal is

relatively long, (5 mm), the positive material nonlinearity overweighs the added difference-frequency-induced CQN. This leads to small values of positive intracavity nonlinearity at shorter wavelengths and larger values of positive intracavity nonlinearity at longer wavelengths.

The measured pulse durations are shown in Fig. 3.4A. The pulse duration without the prism pair anticorrelates with the group delay dispersion, even though similar values of GDD produces strikingly different pulse durations at longer and shorter wavelengths of 860 nm. It is interesting to note that inserting the prism pair and optimizing the pulse duration does not optimally compress the pulse for the wavelengths longer than the phase matched 860 nm.

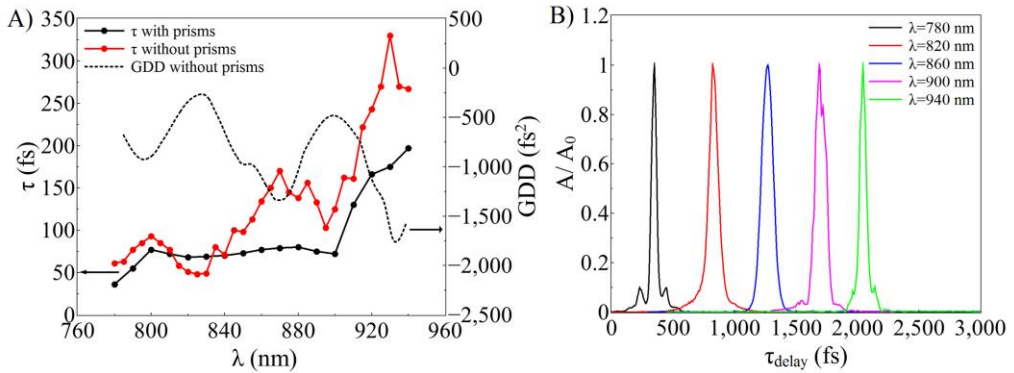


Fig. 3.4. A) Pulse duration with and without the prism pair and resonator group delay dispersion dependence on wavelength. B) Autocorrelation traces of various central wavelengths when prism pair is inserted intracavity and pulse duration is adjusted to minimum value at each wavelength. OPO crystal angle is fixed at  $12.7^\circ$  for optimal conversion efficiency to 860 nm.

The autocorrelation traces of minimal achievable pulse durations at different central wavelengths while minimizing the resonator GDD with the prism insertion is shown in Fig. 3.4B. The autocorrelation trace is Gaussian-like only at around the exact phase matching angle at the wavelength of 860 nm. As the wavelength is changed to shorter and longer wavelengths and GDD is decreased, pulse-splitting behaviour and deteriorated pulse structure start to appear. This is unsurprising, as the cavity nonlinearity is large enough to generate higher order solitons which tend to

split to individual pulses when perturbed [75]. The autocorrelation traces are measured at low resonator dispersion values, which increases the achievable soliton order even further. The higher order solitons split into the larger number of pulses [47]. This results in chaotic-like pattern of autocorrelation trace as minute changes of the ambient conditions destabilize the internal higher order soliton.

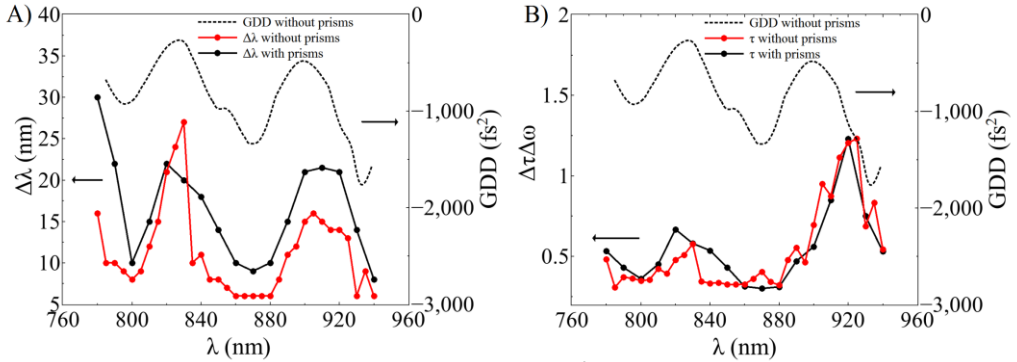


Fig. 3.5. A) Spectrum bandwidth with and without prism pair and resonator group delay dispersion dependence on wavelength. B) Pulse time-bandwidth product with and without prism pair and resonator group delay dispersion dependence on wavelength. OPO crystal angle is fixed at  $12.7^\circ$  for optimal conversion efficiency to 860 nm.

The pulse spectrum bandwidth presented in Fig. 3.5A with and without a prism pair shows good correlation with intracavity GDD. The measured spectra of Fig. 3.6 show pronounced spectrum distortion at longer wavelengths with varying amounts of GDD. Inspecting the time-bandwidth product results in Fig. 3.5B suggests that the pulse formation is influenced by some stronger nonlinear effect. The time-bandwidth product is virtually independent on the applied cavity GDD when the output wavelength is tuned from 770 nm up to the exact phase matching at 860 nm. At longer wavelengths, the CQN distorts the spectrum through self-phase modulation resulting in an increase of time-bandwidth product. As shown by the soliton equation (2.99), further increase of negative GDD would compensate large values of intracavity nonlinearity and allow soliton formation. Despite that, the amount of negative GDD achievable in a prism pair is limited by the physical footprint which is needed to increase the distance between the prisms even further.

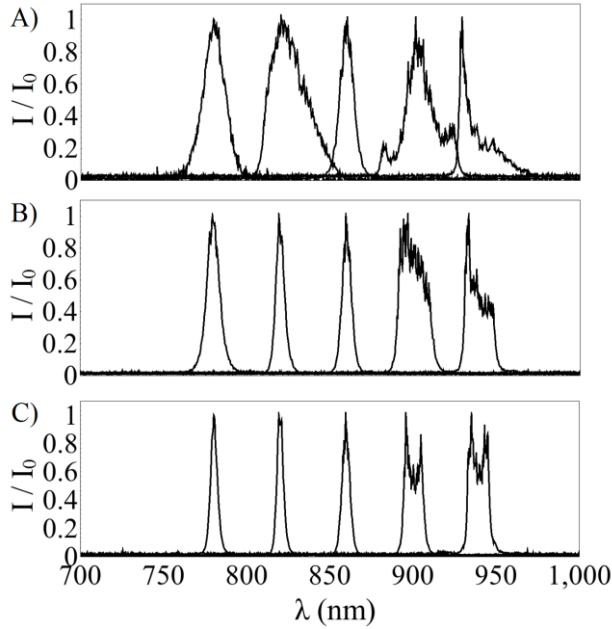


Fig. 3.6. Pulse spectra when prism pair is inserted intracavity and dispersion is varied to the different values of negative group delay dispersion: A) minimum of absolute GDD ( $\sim -500 \text{ fs}^2$  at 880 nm); B) average of absolute GDD ( $\sim -1200 \text{ fs}^2$  at 880 nm); C) maximum of absolute GDD ( $\sim -2000 \text{ fs}^2$  at 880 nm). The GDD values correspond to the GDD ranges shown at Fig. 3.7. In all panels OPO crystal angle is fixed at  $12.7^\circ$  for optimal conversion efficiency to 860 nm.

The variation of output power and pulse duration with intracavity GDD is shown in Fig. 3.7A and Fig. 3.7B. The negative GDD and positive intracavity nonlinearity allow soliton formation. For a soliton with an order  $N_{\text{soliton}} = 1$ , it should lead to a linear pulse duration dependence on intracavity GDD, as given by the equation (2.100). The linear fit of pulse duration dependence on GDD correspond well to the experimental results at wavelengths shorter than exact phase matching wavelength. At longer wavelengths, the dependence deviates from linear. This confirms that the pulse formation effect is soliton-like at shorter wavelengths, when cavity nonlinearity is small enough to be compensated by linear intracavity GDD. The pulses exhibit the signatures of higher order solitons at longer wavelengths, where the spectra are deformed and pulse duration dependence on GDD is influenced

by pulse splitting effects. This is well in line with the time-bandwidth product dependence on GDD at different wavelengths shown in Fig. 3.8B. Soliton pulses should have pulse quality close to transform limit ( $\sim 0.44$  for Gaussian form pulses). The durations of at longer wavelengths are short, most likely because short pump pulse acts as a temporal filter for slightly chirped signal pulses. This effect allows short pulse formation in synchronously pumped femtosecond OPOs without soliton formation mechanism [76]. The temporal filtering is as well evident in Fig. 3.8A, where increasing amounts of intracavity GDD lead to narrower pulse bandwidths. The intracavity GDD stretches the pulse in time domain so that short pump pulse overlaps in time only with part of the signal spectrum. Increasing the GDD leads to stronger filtering effect as is evident from the experimental results.

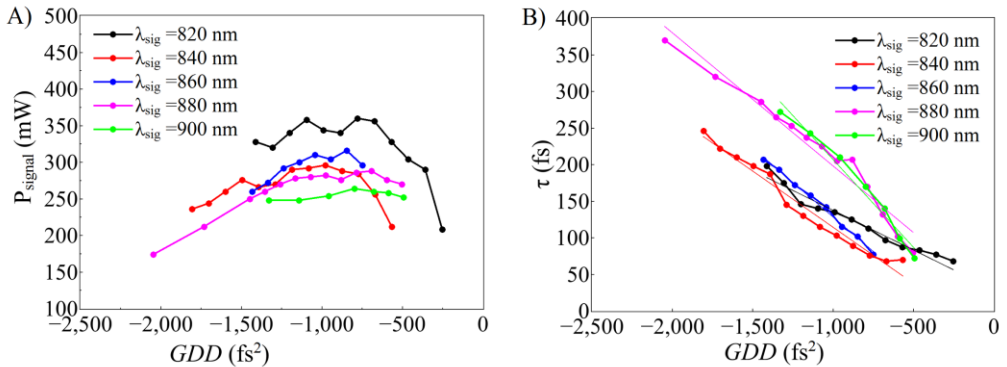


Fig. 3.7. A) Signal output power dependence on the prism pair induced group delay dispersion with varying signal central wavelengths. B) Signal pulse duration dependence on the prism pair induced group delay dispersion with varying signal central wavelengths. In all panels OPO crystal angle is fixed at  $12.7^\circ$  for optimal conversion efficiency to 860 nm.

OPO with negative GDD

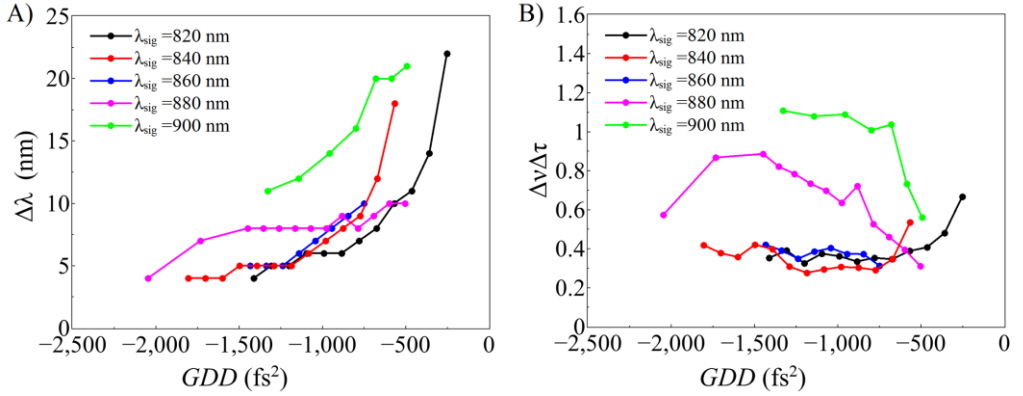


Fig. 3.8. A) Signal spectrum bandwidth dependence on the prism-pair-induced group delay dispersion with varying signal central wavelengths. B) Signal time-bandwidth product dependence on the prism pair induced group delay dispersion with varying signal central wavelengths. In all panels OPO crystal angle is fixed at  $12.7^\circ$  for optimal conversion efficiency to 860 nm.

### **3.3 Summary**

The prism pair induced negative group delay can be used to compensate the material nonlinearity and generate soliton-like pulses, but the required physical footprint limits an integration of the device.

The oscillations of chirped mirror induced negative group delay dispersion are leading to varying signal output pulse duration and spectrum bandwidth.

Large cavity nonlinearity leads to higher order solitons which show pulse splitting behaviour and SPM deformed spectra.

An intracavity prism pair allows to control the generated pulse spectrum form and bandwidth through the interplay of GDD and SPM.

## 4 OPO with negative GDD and CQN

High intracavity intensities in femtosecond optical parametric oscillators induce nonlinear effects in the crystals used for amplification. Previous chapter showed the first observation of the influence of nonlinearity on the spectrum and pulse characteristics when OPO is operated with a phase mismatch. Such effects need to be accounted for to scale the output power and fully understand the temporal and power characteristics of the OPO radiation. Furthermore, other possible nonlinear effects include temporal soliton formation [72, 77], temporal simulton formation [78], four-wave mixing [79, 80] and other effects. In this chapter, cascaded nonlinearities and their effects to soliton formation are focused on. Previous work in the field include DeSalvo *et al.* showing that cascaded nonlinearities induce effective nonlinearity which is proportional to the  $(d_{eff})^2 / \Delta k$  [18]. Gale et al. have shown that this effective nonlinearity can be measured using Z-scan setup and expressed as crystal angle dependent  $n_2$ . Gale et al. and Laenen et al. have shown experimental observation and analysis of soliton formation of resonating signal or idler pulse in OPO [19, 23]. Works by Gale et al. and Laenen et al. considered signal when its wavelength is close to the wavelength for which second harmonic generation is phase matched - either close to degeneracy or to phase matched parasitic second harmonic generation. In this chapter, we demonstrate that effective nonlinearity can be observed for any resonating signal or idler wavelength if its wavelength is tuned from the exact phase matching - either by tuning the cavity delay or by rotating the intracavity crystal. We also perform Z-scan measurements and show that this difference-frequency-induced effective nonlinearity cannot be explained the same way as second harmonic induced effective nonlinearity. All these findings lead to a better understanding of how to design a high power femtosecond optical parametric oscillator with optimal pulse characteristics.

Parts of the material covered in this chapter have been published in publication P4 and presented in conference paper C3.

## 4.1 Experimental procedures

The optical setup used for the experiments is shown in Fig. 4.1. The optical parametric oscillator is pumped by second harmonic of Yb:KGW based femtosecond oscillator (Flint, Light Conversion). Pump oscillator emits 8 W of average power with 120 fs pulse duration at 1030 nm central wavelength and 76 MHz repetition rate. Pump light is frequency doubled in 2.5 mm length LBO crystal with AR coatings, where 4 W of average power at 515 nm is generated with 50% conversion efficiency. Fundamental light is filtered out and pump light is delivered to pump the optical parametric oscillator. Pump light is focused to the spot size of 40  $\mu\text{m}$ , which is the size of resonating signal mode's radius. Cavity mirrors M6, M7, M8, M9 are high reflective in the range from 820 to 940 nm and have a mean GDD of  $-100 \text{ fs}^2$  through the wavelength range. The total resonator round trip group velocity dispersion is  $-550 \text{ fs}^2$  for a case of BBO and  $-600 \text{ fs}^2$  for a case of LBO. The used concave mirrors ( $R=-200 \text{ mm}$ ) focus the resonating beam into the nonlinear crystal. One of the curved mirrors, M5, is highly reflective in 820 to 940 nm range and has high transmittance at the pump wavelength of 515 nm. The output coupler OC with 20% of transmission in the wavelength range from 820 to 940 nm was used. Two different nonlinear crystals (both type I, both from Eksma Optics) were investigated as nonlinear gain materials (NL) for optical parametric oscillator: a) 2 mm long BBO crystal ( $\theta = 24^\circ$ ) and b) 2.5 mm long LBO crystal ( $\theta = 14^\circ$ ). Both crystals were AR coated at 1030+515 nm. The reflection coefficient at the signal wavelength range 820-920 nm was experimentally measured to vary from 2% (820 nm) to 1.5% (920 nm) for BBO and from 5% (820 nm) to 3.5% (920 nm) for LBO. The crystals were mounted on precision rotation stage allowing the control of phase matching angle, which was later recalculated to internal angle. Beam dump discarded the remaining pump and idler beams. OPO cavity length was adjusted by moving the output coupler placed on a translation stage, to enable finding synchronous pumping conditions.

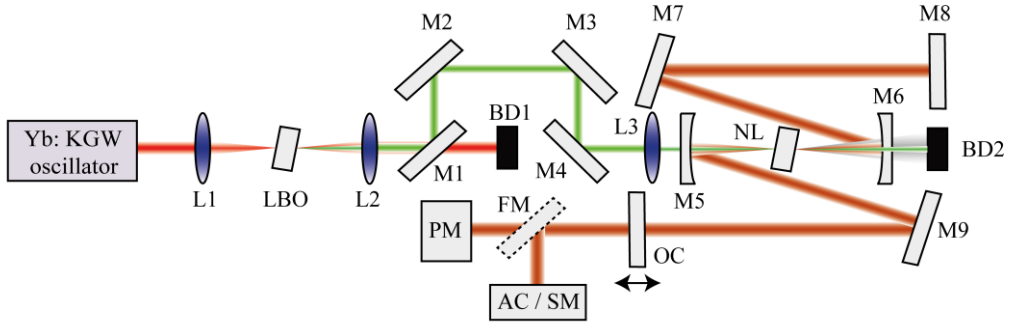


Fig. 4.1. Experimental setup. L1, L2, L3 – lenses for second harmonic generation, collimation and pump light focusing respectively. M1, M2, M3, M4 mirrors for pump light delivery with high transmission at fundamental wavelength. M5, M6 – curved resonator mirrors. M7, M8, M9 – plane resonator mirrors. OC – output coupler, NL – nonlinear crystal, BD1, BD2- beam dump, FM – flip mirror, PM – power meter, AC – autocorrelator, SM – spectrometer.

Average power of output radiation was measured using a power meter (Nova-2, Ophir) equipped with a thermopile detector (30(150)A-BB-18, Ophir). Radiation spectra were recorded using a spectrometer (STS-NIR, Ocean Optics), pulse durations were measured using a scanning autocorrelator (Geco, Light Conversion).

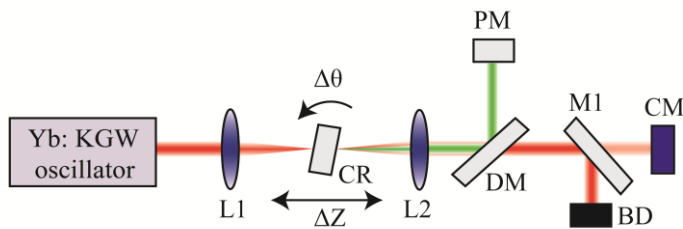


Fig. 4.2. Z-scan experimental setup. L1, L2 – lenses for second harmonic generation and imaging to the camera. CR – nonlinear crystal on a linear translation  $\Delta Z$  and rotation  $\Delta \theta$  stages. DM – dichroic mirror. PM – power meter. M1 – highly reflective mirror HR1030+515 nm acting as a camera filter for fundamental harmonic. BD – beam dump. CM – camera for fundamental harmonic beam radius change.

Nonlinear refractive indices were measured in a home-built Z-scan setup shown in Fig. 4.2. The OPO pump Yb: KGW “Flint” oscillator with 8 W of average power and 120 fs pulse duration was used as a light source. The beam was focused with  $f = 200$  mm lens to the spot of 75  $\mu\text{m}$  beam radius ( $1/e^2$ ), and the sample was translated along the propagation direction. Because of the simplicity of the approach, the Z-scan method with direct measurement of beam radius with CCD camera was used [81]. The beam profile width of the fundamental radiation was monitored with a CCD camera while the second harmonic was filtered out. The conversion efficiency was limited to 15 % in order to measure cascaded nonlinear phase at the conditions, when parametric conversion is not saturated. Avoiding saturation is important because cascaded nonlinear phase (or nonlinear refractive index) can only be considered a linear function of intensity in a narrow range of intensities, as shown in chapter 2.3 and in [82]. As the beam profile widths were measured, care was taken to preserve a high fundamental beam quality during the conversion process. Low intensity and large beam size were used to mitigate second harmonic beam walk-off effect and to prevent fundamental beam deviation from Gaussian beam under strong conversion efficiency. Both of these effects limited the upper bound of the conversion efficiency. The lower bound of the conversion efficiency was limited by the noise of the CCD camera. The measured Z-scan traces were fitted by a numerical propagation model solved in spatial domain with Kerr-like medium as a source of nonlinearity. The resultant theoretical nonlinear refractive index was calibrated by measuring and fitting Z-scan traces of well-known materials with different  $n_2$  values (fused quartz, BK7, SF10 glasses). In such a way, the linearity of the measurement setup was calibrated, and relative  $n_2$  measurements could be employed instead of absolute ones. All the subsequent measurements of LBO and BBO were compared to the nonlinear phase of fused silica sample.

## 4.2 Results and discussion

The resonating signal wavelength can be changed in two ways – by rotating the nonlinear crystal to match phase matching to particular wavelengths or by tuning the resonator length to match the synchronous pumping condition for different wavelengths. The focus on this investigation was the changes in pulse formation characteristics when these two methods of tuning are applied.

In Fig. 4.3A, tuning curves are given of BBO (red) and LBO (black) based optical parametric oscillators when central wavelength is changed by tuning the resonator length. The crystal angle is fixed to maximize parametric conversion at the center of the mirror reflection range. The dashed curves indicate numerical simulation results produced by solving coupled wave equations (2.59) to (2.61). The difference between maximum output powers of LBO and BBO is mainly determined by lower nonlinear coupling coefficient of LBO and higher reflectivity of LBO crystal coatings at 820 nm. A similar experiment was performed while the central wavelength was held fixed at 850 nm and the cavity length was varied together with the crystal angle, thereby compensating the change in phase matching wavelength by the offset of synchronous pumping condition. The results are shown in the Fig. 4.3B with dashed curves indicating simulation results. As can be seen in both cases, the curves are asymmetric for both LBO and BBO crystal. This asymmetry can be explained by a closer scrutiny of time and spectral domain results.

OPO with negative GDD and CQN

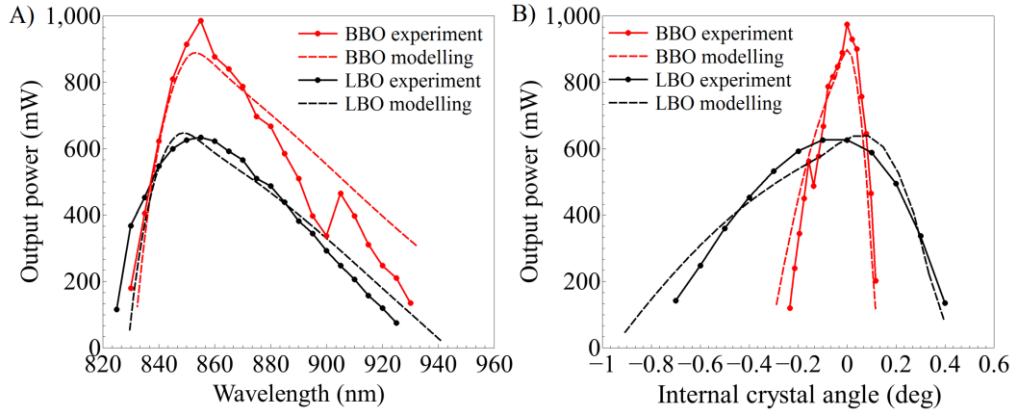


Fig. 4.3. Panel A) - output power dependence on central wavelength when crystal angle is fixed at  $23.1^\circ$  for BBO and  $12.6^\circ$  for LBO. Panel B) – output power dependence on crystal rotation angle while central wavelength is fixed at 850 nm. Solid curves of BBO (red) and LBO (black) indicate the experimental results. Dashed curves depict the results of numeric simulations.

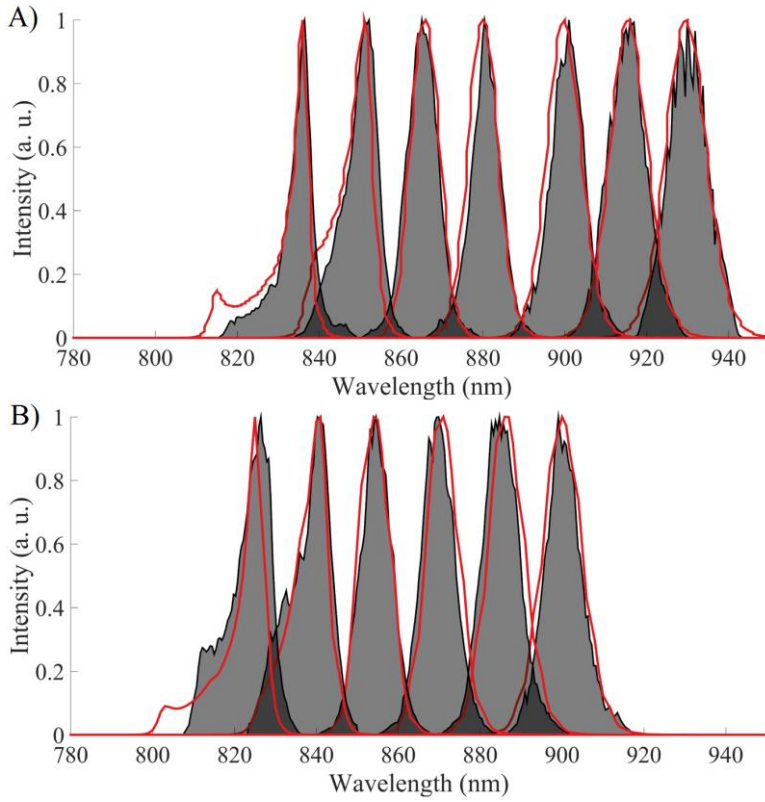


Fig. 4.4. Measured (gray) and simulated (red line) spectra while resonator length is changed with fixed crystal angle with BBO at  $23.1^\circ$  (panel A)) and LBO at  $12.6^\circ$  (panel B)).

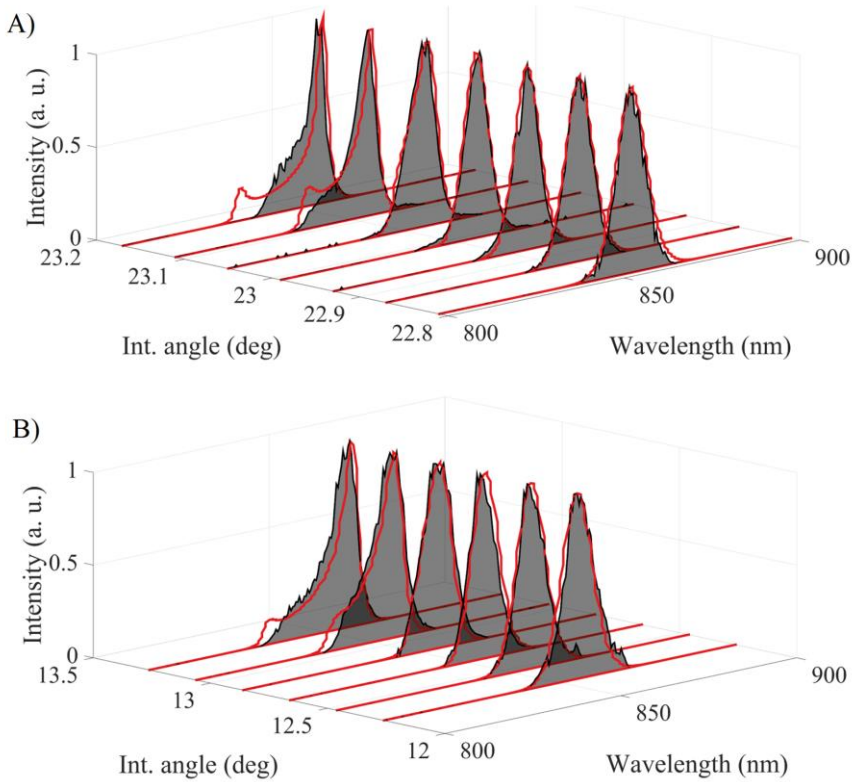


Fig. 4.5. Measured (gray) and simulated (red line) spectra while rotating crystal angle in BBO (panel A)) and LBO (panel B)) with wavelength fixed at 850 nm.

The spectra of output signal with intracavity LBO and BBO are presented in Fig. 4.4 and Fig. 4.5. In Fig. 4.4, the resonating wavelength was changed by changing the cavity length while keeping the crystal angle fixed. In Fig. 4.5, on the contrary, the central wavelength was kept fixed while simultaneously rotating the crystal and adjusting the resonator length to keep the central wavelength fixed at 850 nm. The red curves indicate simulation results which show very good agreement with the experimental results when spectra are close to Gaussian and a bit worse one for deformed spectra. As can be seen from the spectra, both resonator length tuning and crystal rotation produce the same trend – spectra remain close to Gaussian on one side of the wavelength / crystal tuning range and become deformed in the other side

of the range. The pulse durations of the measured output signals are given in Fig. 4.6, where experimental (solid curves) and simulation (dashed curves) are compared. It is also evident that the pulses tend to increase / decrease in duration almost linearly as the wavelength is tuned or crystal is rotated. To see if this effect is entirely due to phase mismatch, the same power tuning and pulse duration curves were plotted as functions of phase mismatch  $\Delta k = k_p - k_s - k_i$  calculated from crystal rotation angle and from central wavelength of the spectrum. The results are given in Fig. 4.7 for the output power and pulse duration dependence on phase mismatch for LBO and BBO. As can be seen from the tuning curves, both the output power and the pulse duration exhibit the same trend regardless of the phase mismatch tuning method.

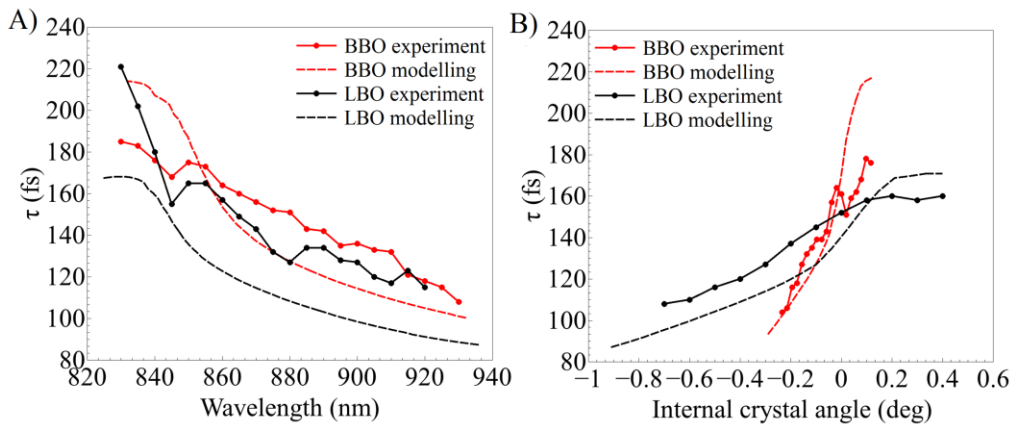


Fig. 4.6. A): Pulse duration dependence on central wavelength while the crystal angle is fixed at  $23.1^\circ$  for BBO and  $12.6^\circ$  for LBO. B): Pulse duration dependence on crystal rotation angle while the central wavelength is fixed at 850 nm. Solid curves of BBO (red) and LBO (black) indicate experimental results. Dashed curves indicate simulation results.

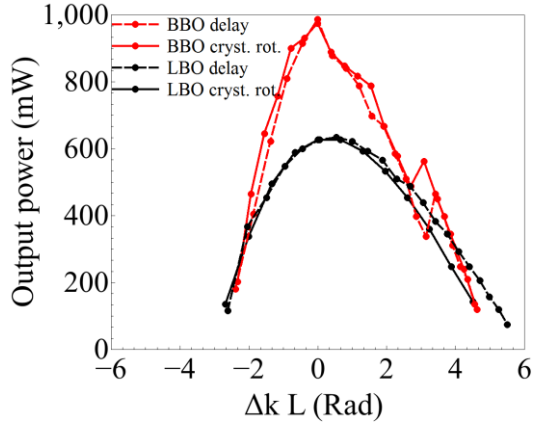


Fig. 4.7. The dependence of output power on the phase mismatch for BBO (red) and LBO (black). Solid lines show the dependence while crystal is rotated keeping the central wavelength fixed at 850 nm. Dashed lines show the results when central wavelength is changed, keeping the crystal angle fixed at  $23.1^\circ$  for BBO and  $12.6^\circ$  for LBO.

Furthermore, high and low output power regimes were compared. The output power (Fig. 4.8A), pulse bandwidth (Fig. 4.8B), pulse duration (Fig. 4.8C), time-bandwidth product (TBP) (Fig. 4.8D) are shown for high output power ( $P_{pump} = 4$  W) and low output power ( $P_{pump} = 2$  W) regimes both for BBO and LBO. The crystal is rotated to change the phase mismatch, the central wavelength was fixed at 850 nm.

The high and low power spectrum bandwidth plots of Fig. 4.8B show strikingly different values, especially in negative phase mismatch range. In low power regime, spectra remain Gaussian in the entire phase mismatch range. In contrast, at high powers spectra become deformed for negative phase mismatch and remain smoothly Gaussian when the phase mismatch is positive. This indicates the effect of phase-mismatch-induced cascaded nonlinearity which under high power and negative phase mismatch leads to strong spectrum deforming self-phase modulation. Surprisingly, the Fig. 4.8C results do not show difference in pulse duration at high and low powers. The Fig. 4.8D TBP results show that for a fixed phase mismatch value, increasing the pump power decreases the time-bandwidth product towards the bandwidth-limited TBP value, especially in positive phase mismatch range. The bandwidth limited TBP value indicates equilibrium of nonlinear phase modulation and GDD induced linear phase modulation, producing soliton-like unchirped pulses. Furthermore, this power related TBP decrease also confirms the influence of

nonlinear phase modulation to pulse characteristics. If soliton-like pulse formation is considered, soliton equation (2.100) given by [19, 47] should be valid. The equation indicates that increasing power should lead to decrease of pulse duration. Surprisingly, this is not the case as given by Fig. 4.8C, the pulse duration is influenced by the phase mismatch and not by the power.

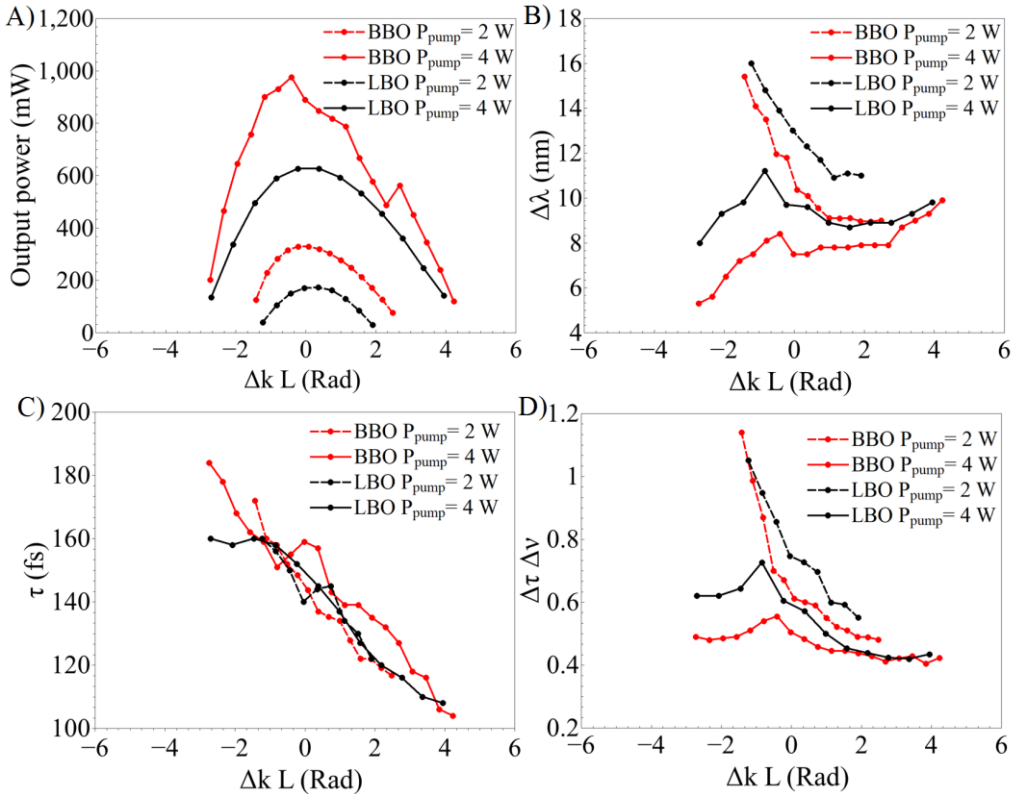


Fig. 4.8. For all panels red curves indicate BBO results, black curves indicate LBO results. Solid curves are results with high pump power  $P_{\text{pump}} = 4$  W, dashed curves indicate results with low pump power  $P_{\text{pump}} = 2$  W. Panel: A) Output power dependence on phase mismatch; B) pulse bandwidth FWHM dependence on phase mismatch; C) pulse duration dependence on phase mismatch; D) time-bandwidth product dependence on phase mismatch. Phase mismatch is induced by changing crystal angle at the central wavelength of 850 nm.

The numerical modelling was carried out to gain further insight into the discrepancy between soliton equation and measured pulse duration dependence. As LBO and BBO crystals showed similar results, only BBO crystal was simulated. The signal wavelength was 850 nm. Two distinct cases were simulated: varying pump power with fixed nonlinear refractive index  $n_2 \sim 3 \cdot 10^{-20} \text{ m}^2/\text{W}$  (the results are given in Fig. 4.9A)); varying material nonlinear refractive index with fixed pump power  $\sim 4 \text{ W}$  (the results are given in Fig. 4.9B). Red zone of panel a) indicates experimentally probed high and low power region. Red zone of panel b) indicates experimentally probed effective nonlinear refractive index which was changed by varying phase mismatch. Modelling results of Fig. 4.9A confirm experimental observation of Fig. 4.8C. Output pulse duration is independent on resonating power in our experimental pump power range. On the other hand, varying of nonlinear refractive index has an inverse relationship to the pulse duration as shown in Fig. 4.9B.

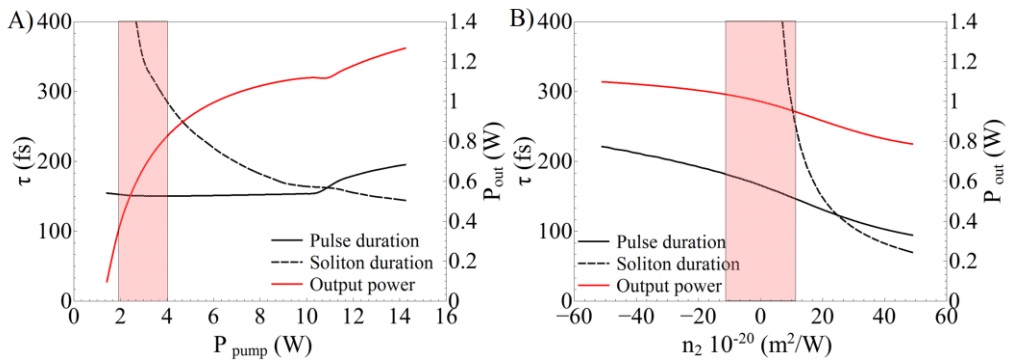


Fig. 4.9. Numerical simulation results of OPO with BBO crystal output pulse duration (solid black, left axis), power (solid red, right axis) and soliton duration (dashed black, left axis) in two different cases: A) Nonlinear refractive index is fixed at  $n_2 \sim 3 \cdot 10^{-20} \text{ m}^2/\text{W}$  and pump power is varied; B) Pump power is fixed at 4 W and nonlinear refractive index is varied. Red zones indicate our experimental conditions when pump power or effective nonlinear refractive index (with induced phase mismatch) is varied. Simulation wavelength is 850 nm.

The soliton duration given by equation (2.100) is also plotted in Fig. 4.9A and Fig. 4.9B, inserting in the equation the simulated parameters of nonlinear

refractive index and intracavity fluence. The resonator group velocity dispersion is the same as in our experimental scheme  $GDD \sim -550 \text{ fs}^2$ , weighed by crystal length. Soliton durations are larger than the simulated OPO output durations (which are similar to the experimentally measured ones) in our experimental pump power and  $n_2$  range. This indicates that the pulses are not classical solitons governed by soliton equation, despite the fact that the pulse-bandwidth product is close to transform limit. Nevertheless, the pulses are soliton-like because the linear group velocity dispersion is partially compensated by nonlinear phase in positive  $n_2$  range. Our explanation for this observation is that synchronous pumping with short length pulse  $\tau \sim 120 \text{ fs}$  allows ultrashort pulse formation with pulse durations shorter than soliton threshold. Increasing the pump power and intracavity power does not change the pulse duration, because increased gain acts as a stronger spectral filter for slightly chirped resonating signal pulses. This leads to pulse duration increase balancing the pulse duration decrease arising from the soliton-like linear and nonlinear phase compensation.

It is interesting to note, that based on the simulation of Fig. 4.9A, when the soliton pulse duration reaches the intracavity pulse duration, abrupt changes in pulse duration and output power can be observed. Closer look at the simulated spectrum and time domain intensity (Fig. 4.10A and Fig. 4.10B) show that just after reaching the soliton threshold, the spectrum gets a tail in the long wavelength side and time envelope of the pulse becomes double peaked. Classical soliton theory indicates that surplus of energy over the soliton threshold is emitted as dispersive wave. In the case of OPO with broad gain bandwidth, this emitted pulse is amplified and is locked to the main pulse deteriorating the pulse quality. The closer look at Fig. 4.9B shows no abrupt change whenever soliton duration reaches intracavity soliton duration. The reason is lower pump power and lower parametric gain which does not amplify the dispersive wave strongly enough to have an impact on spectrum and pulse duration. This is an interesting observation which should definitely have to be considered in a further scaling of the output power of the OPO.

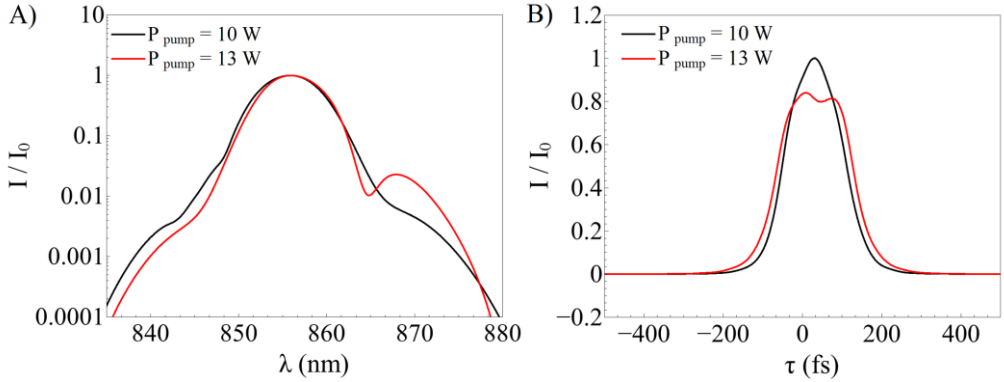


Fig. 4.10. Simulated spectra (panel A) and time domain intensities (panel B)) when OPO is pumped with two slightly different pump powers below (black solid line) and above (red solid line) soliton formation threshold.

To further investigate the origin of the phase mismatch impact on pulse duration, the method of Gale *et al.* [19] was used to probe the nonlinear phase dependence on phase mismatch. The same crystals as used for optical parametric oscillation were probed in a Z-scan setup. The crystal was rotated around the exact phase matching angle in order to get the cascaded nonlinearity dependence on crystal rotation angle or in other words phase mismatch. The used wavelength was 1030 nm, as the power of the OPO output at 850 nm was too low for Z-scan measurement. This experimentally dictated choice is justified, because crystal angle tolerances and effective nonlinearities  $d_{\text{eff}}$  are similar for both wavelengths and yield similar simulated curves of cascaded phase matching dependence on crystal angle.

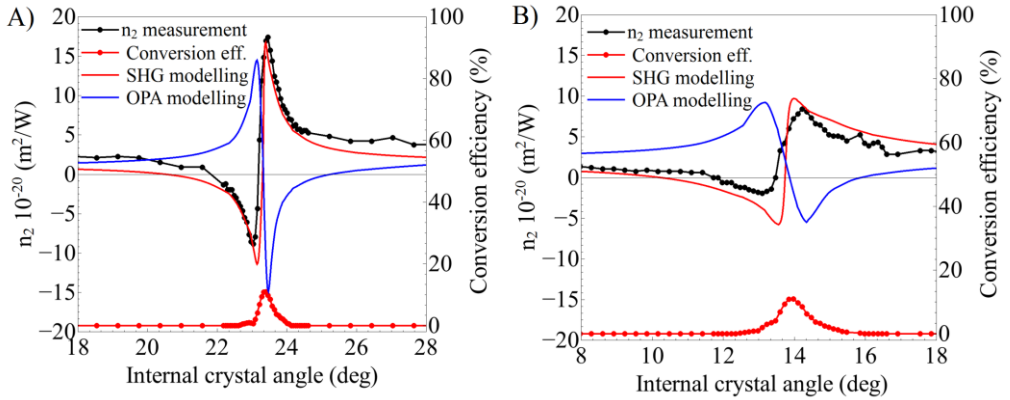


Fig. 4.11.  $n_2$  measurement while rotating the internal angle of the BBO crystal (panel A)) and the LBO crystal (panel B)). The measurement wavelength was 1030 nm. Black solid and symbol curve – experimental  $n_2$  measurement; red solid and symbol curve- conversion efficiency; red solid curve – SHG simulation; blue solid curve – OPA simulation.

The experimental results are presented in Fig. 4.11. Black symbols indicate the experimental results of nonlinear refractive index measurement. The red symbols indicate the conversion efficiency to the second harmonic while nonlinear crystal is rotated. Numerical simulation of the similar experiment in time domain was carried out by using a system of equations (2.59) to (2.61) in a single pass in the second harmonic generation (SHG) mode (signal and idler wavelength 1030 nm, pump 515 nm, with amplitude of pump starting from noise). The phase mismatch was varied and the nonlinear phase after parametric interaction was extracted from the split-step algorithm. The numerical modelling results are depicted by a red smooth line in Fig. 4.11. The results are consistent with the classic nonlinear cascaded phase matching behavior, which can be approximated with formula  $-d_{\text{eff}}^2 / \Delta k$  as shown in reference [82]. This formula also explains the difference between the LBO and BBO. Wider acceptance angle of LBO results in wider range of crystal rotation angle; in the meantime, higher effective nonlinearity  $d_{\text{eff}}$  in BBO produces larger peak to peak nonlinear refractive variation. However, the most striking observation is that this SHG-induced nonlinear refractive index variation is exactly opposite to the numerical modelling results given by Fig. 4.9B. Increasing nonlinear refractive index should lead to decrease of pulse duration as given by the soliton duration equation

(2.100). However, the comparison of the Fig. 4.6B and the steep central range of Fig. 4.11 shows exactly the opposite. In order to explain this discrepancy, the system of equations (2.59) to (2.61) was again modelled in single pass in optical parametric amplification (OPA) mode (signal and idler wavelength 1030 nm, pump 515 nm, with amplitude of idler starting from noise and  $E_{0 \text{ pump}} \gg E_{0 \text{ signal}}$ ). Nonlinear phase is again extracted after split step algorithm. The resulting nonlinear refractive index is plotted in Fig. 4.11 with blue line and is inverted with respect to the SHG induced nonlinearity. As can be seen from the graph, the OPA induced nonlinear phase result is much better suited for the explanation of solitonic behaviour in optical parametric oscillation, especially if parametric amplification is phase mismatched.

In the Fig. 4.12 (left axis), the experimentally measured pulse duration is plotted as a function of phase mismatch, while crystal is rotated or resonator length is changed, both for LBO and BBO. Solid lines (right axis) indicate numerical modelling results of total nonlinear refractive index dependence on phase mismatch. The results are calculated in single-pass OPA regime, with pump wavelength 515 nm, signal 850 nm and idler 1300 nm. The total nonlinear refractive index is composed of material nonlinear refractive index (its value is given when phase mismatch is zero) and a larger part originating from the cascaded nonlinearity. As can be seen from the trend of experimental results, if positive/negative phase mismatch is induced in the parametric conversion, the pulse experiences nonlinear phase that has to be compensated by the linear phase of the resonating signal, meaning shorter/longer pulse width and broader/narrower spectrum. This soliton-like formation occurs regardless of how the phase mismatch changing is varied (crystal rotation or central wavelength change). The limit of pulse shortening is imposed by parametric amplification bandwidth (calculated from the difference of inverse group velocities of signal and idler) which in our experiment is 49 nm for 2 mm length of BBO and 101 nm for 2.5 mm of LBO at signal wavelength of 850 nm. Experimentally, the SPOPO could be tuned over the range of more than 100 nm with fixed crystal angle. Negative nonlinear refractive index produces nonlinear phase modulation not compensated by negative linear dispersion and produces distorted spectra shown in the Fig. 4.4 and Fig. 4.5. The increased pulse duration in the conditions corresponding to the negative nonlinear refractive index range also decreases the output power of the optical parametric oscillator (Fig. 4.3A), because the intensity is decreasing.

OPO with negative GDD and CQN

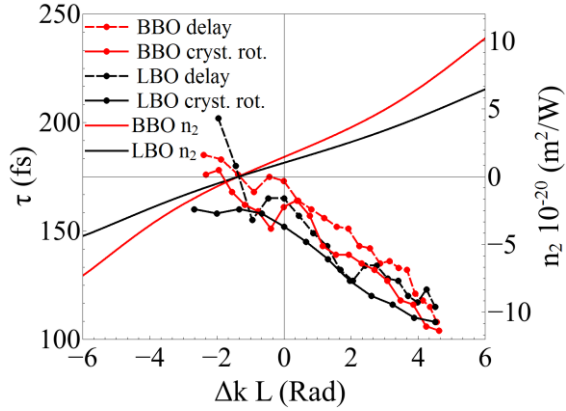


Fig. 4.12. Left axis shows the dependence of pulse duration on the phase mismatch for BBO (red) and LBO (black). Solid lines show the dependence while crystal is rotated keeping the central wavelength fixed at 850 nm. Dashed lines show the results when central wavelength is changed, keeping the crystal angle fixed at  $23.1^\circ$  for BBO and  $12.6^\circ$  for LBO. Right axis, solid lines are the simulation of effective nonlinear refractive index while phase mismatch is changed for LBO (black) and BBO (red).

### 4.3 Summary

High average power femtosecond optical parametric oscillator pumped by the second harmonic of Yb: KGW solid state oscillator was investigated. The tuning behavior of the OPO turned out to be governed by the phase mismatch. Identical tuning behavior was observed, irrespective of whether the phase mismatch to resonating signal pulse was induced by rotating the nonlinear crystal or changing signal central wavelength with fixed crystal angle. The high and low pump power regimes were compared, deviation from soliton equation was observed when intracavity power is varied. The measured pulse durations were lower than the classical soliton duration, indicating that the pulses are not classical solitons. The time bandwidth product was measured to be close to the bandwidth limited value, proving that linear round trip phase is partially compensated by nonlinear phase, allowing soliton-like pulse formation below the soliton threshold. It was demonstrated that in the case of optical parametric amplification, the cascaded nonlinear refractive index shows the dependence on the phase mismatch inverted compared to the case of second harmonic generation. The observed changes in the spectrum, power and pulse duration of the OPO output radiation could be interpreted in terms of competing effects of different cascaded nonlinearities. The phase mismatch induces nonlinear refractive index change and soliton-like pulse changes duration. Using the numerical model including these cascaded nonlinear effects allowed us to explain why and how the output power, spectrum and pulse duration vary in an OPO operating under soliton-like pulse formation conditions below and above soliton threshold.

## 5 OPO with positive GDD and CQN

In this chapter, a novel approach is investigated of soliton generation in an all-positive-dispersion femtosecond OPO pumped by the second harmonic of Yb:KGW femtosecond oscillator. As shown in chapters 3 and 4, high intracavity intensity of OPOs leads to self-phase modulation induced spectral broadening which usually needs to be compensated by negative group delay dispersion created by a prism pair [19, 72] or chirped mirrors [80, 83]. Design of broadband chirped mirrors is complicated, because increasing the bandwidth leads to lower reflection coefficient and larger GDD oscillations across the spectrum. Such GDD irregularities have a negative impact on pulse duration, power and spectral characteristics of the OPO output [73]. The manifestation of this effect was presented in chapter 3. On the other hand, GDD compensator employing a prism pair requires large physical separation between the prisms, resulting in a larger device footprint. A novel approach of SPM compensation is to use a negative cascaded quadratic nonlinearity (CQN). Negative CQN was exploited in a comb generation [24], supercontinuum generation [22, 84], CW pumped optical parametric oscillators [28] and ultrafast laser oscillators with varying levels of pulse energies [29 - 33]. The evidence of the CQN impact to pulse characteristics was also observed in the femtosecond optical parametric oscillators while operating with negative and positive group delay dispersion in a soliton regime, but a more detailed investigation is still lacking [23, 82].

In this chapter, three series of experiments are presented. In the first series A) the CQN was induced by changing the phase matching angle of the OPO crystal, i.e. running OPO at non-optimal conversion efficiency. In addition to lower efficiency, another drawback of this method is the fact that amplification and negative CQN are coupled and independent control of both parameters cannot be achieved. We did observe soliton-like pulses with low time bandwidth product even below the first soliton energy threshold. This effect was ascribed to temporal domain filtering with short duration synchronous pump pulses, as shown in [76]. In the second group of experiments B), an additional doubling crystal was placed in the second intracavity focus. The second nonlinear crystal was cut for frequency doubling the signal wave, and the phase matching was detuned to low conversion efficiency. Contrary to the first series of experiments, the OPO crystal was now exactly phase matched and the OPO was operated at optimal conversion efficiency. This configuration allowed independent control of amplification and negative CQN parameters. Finally, in the

third series of experiments C), the wavelength tuning characteristics are demonstrated of all positive dispersion femtosecond optical parametric oscillator with two negative CQN methods – either rotating OPO crystal, or SHG crystal.

Parts of the material covered in this chapter have been published in publications P1 and P5.

## 5.1 Experimental procedures

The optical setup used in the experiments is shown in Fig. 5.1. The optical parametric oscillator is pumped by the second harmonic of Yb: KGW based femtosecond oscillator (Flint, Light Conversion). The pump oscillator emits 12 W of output power with 140 fs pulse duration at 1030 nm central wavelength and 76 MHz repetition rate. The pump light is frequency doubled in 2.5 mm length LBO crystal with AR coatings (1030+515 nm), where 6 W of output power at 515 nm is generated with 50% conversion efficiency. The pulse duration of the 515 nm light is 135 fs. The fundamental light is filtered out and the 515 nm beam is delivered to the OPO crystal. The pump light is focused to the spot size of 50  $\mu\text{m}$  (radius  $1/e^2$ ) to match the resonating mode's radius. The cavity design includes the second focus, where CQN crystal can be placed. The calculated mode radius in the second focus is the same as in the amplifying crystal with the spot size of 50  $\mu\text{m}$  (radius  $1/e^2$ ). Cavity mirrors M7, M8, M9, M10 are high reflective in the range from 770 nm to 970 nm, the used mirror design is a simple  $\lambda/4$  stack with a low group velocity dispersion through the wavelength range (decreasing from +20 fs<sup>2</sup> at 770 nm to -20 fs<sup>2</sup> at 970 nm). The used concave mirrors (M5, M6, M7, M8 with radius  $R = -200$  mm) focus the resonating beam in the nonlinear crystals. Mirrors M5, M6 were highly reflective in 770-970 nm range with high transmission at 515 nm and a similar group velocity dispersion as the plane mirrors. The output coupler OC has 10 % of transmission in the wavelength range of 770-970 nm.

Multiple fused silica windows (GP1, 14 mm thickness, AR coated for 650-1000 nm,  $R < 0.5$  %) allowed to coarsely vary the positive group velocity dispersion of the resonator. In most experiments with fixed resonator GDD, two fused silica glass plates were used and the total calculated group delay dispersion of the cavity was  $\sim 1800$  fs<sup>2</sup> at 860 nm. In the GDD tuning experiments, up to 7 fused silica plates (GP1) were inserted into the cavity to allow the maximum GDD value of 5500 fs<sup>2</sup> at 860 nm. Up to 2 fused silica windows (GP2, 3.5 mm thickness, AR coated for 650-1000 nm,  $R < 0.5$  %) were inserted intracavity to finely vary positive group velocity dispersion of the resonator. To keep the resonator losses the same with varying number of intracavity glass plates, a 0.5 mm thick uncoated fused silica glass plate BP was rotated out of the Brewster's angle to induce additional reflection losses, which were measured by power meter. The OPO crystal was a 2.5 mm thick LBO (type I,  $\theta = 14^\circ$ , Eksma Optics). The crystal was AR coated at 1030+515 nm. In the second and third part of the experiments, an additional 0.7 mm thick BBO crystal

was used in the second focus (type I,  $\theta=24^\circ$ , Eksma Optics). The crystal was AR coated at 1030+515 nm. The reflection coefficient at the signal wavelength range 770-970 nm was experimentally measured to vary from 2.5 % (770 nm) to 1 % (970 nm) for BBO and from 5 % (770 nm) to 2 % (970 nm) for LBO. Both crystals were mounted on precision rotation stages allowing the control of the phase matching angle, which was later recalculated to internal angle.

In order to minimize the effect of crystal tilt on the cavity alignment, the resonator stability was optimized for the lowest misalignment sensitivity, following ABCDEF matrix formalism calculations [67],[85]. The misalignment sensitivities for rotation of both crystals were calculated to be similar in magnitude, and the crystals were rotated in opposite directions to keep the output beam position unchanged during tuning. Nevertheless, the pump beam direction had to be slightly adjusted during this procedure indicating, that the compensation was not exact. Beam dump discarded the remaining pump and idler beams and the second harmonic of the signal beam after the second pass through the BBO crystal. The power of the doubled signal beam was measured after the first pass through the BBO crystal. The coatings of M8 mirror were not optimized for UV transmission, the transmission was measured to be 70 % at 430 nm and the measured power was recalibrated. OPO cavity length was adjusted by moving the output coupler placed on a translation stage, to enable synchronous pumping conditions. The movement of translation table is also used to stabilize the central wavelength of OPO generation. Ambient temperature deviations lead to the pump and OPO resonators' length changes. For OPO to generate, the synchronous pumping condition has to be always satisfied. Under small temperature changes, the generation shifts to signal wavelengths with larger or smaller group velocities, determined by the cavity GDD. Therefore, the central wavelength is used as a feedback signal for the movement of the translation stage.

When phase mismatch is induced either with OPO or SHG crystals, the beam quality is not changed if resonator is operated in the center of the  $(A+D)/2$  stability parameter range, with a stable zone defined as a  $-1 < (A+D)/2 < 1$ . When operated near the resonator's stability edge with  $(A+D)/2 \sim \pm 1$ , the resonator is sensitive to the spatial focusing / defocusing induced by the CQN. This leads to the change of resonator's mode size. The detailed analysis of spatial effects are presented in chapter 7 of this dissertation. In the remainder of the experiments, we have operated the resonator at the center of the  $(A+D)/2$  parameter stability range with  $(A+D)/2 \approx 0$  for both coordinates, where the spatial distortions of the mode due to CQN are minimal.

Average power of the output radiation was measured using a power meter (Nova-2, Ophir) with a thermopile detector (30(150)A-BB-18, Ophir). Spectra were

recorded using a spectrometer (STS-NIR, Ocean Optics), pulse durations were measured using scanning autocorrelator (Geco, Light Conversion), and the pulse trains were measured with a photodiode (DET10A2, Thorlabs) connected to an oscilloscope (TDS 3054, Tektronix).

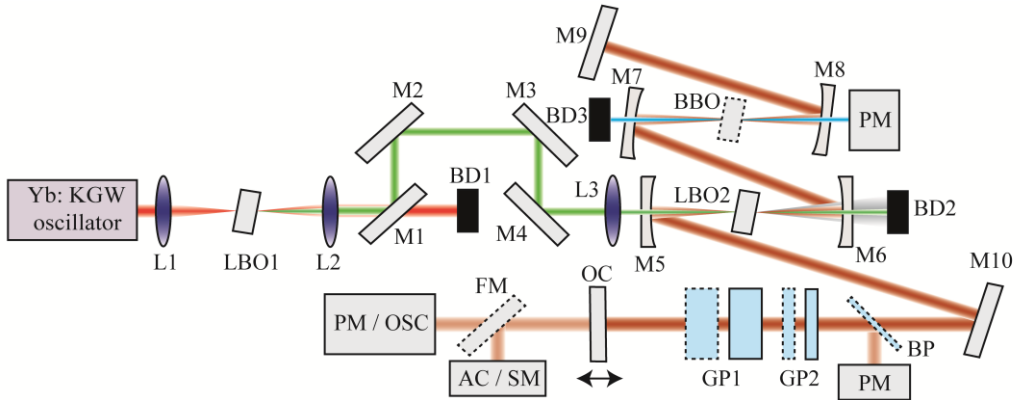


Fig. 5.1. Experimental setup. L1, L2, L3 – lenses for second harmonic generation, collimation and pump light focusing respectively. M1, M2, M3, M4 – mirrors for pump light delivery with high transmission at fundamental wavelength. M5, M6, M7, M8 – curved resonator mirrors. M9, M10 – plane resonator mirrors. OC – output coupler on a translation stage. LBO1 – second harmonic crystal. LBO2 – intracavity LBO crystal on a rotation stage. BBO – intracavity BBO crystal on a rotation stage used in experiment parts B) and C). GP1, GP2 intracavity fused silica glass plates. BP – intracavity fused silica glass plate near to Brewster's angle. BD1, BD2, BD3 – beam dump, FM – flip mirror, PM – power meter, OSC – oscilloscope, AC – autocorrelator, SM – spectrometer.

## 5.2 Results and discussion

### 5.2.1 Single nonlinear crystal scheme with DFG CQN

In the first part of the experiments, the OPO crystal is phase mismatched by angle tuning while the central wavelength is fixed at 860 nm. The resonator length is changed for precise wavelength control. The induced cascaded quadratic nonlinearity originates from phase-mismatched difference frequency generation. The mode radius in LBO crystal is  $\omega=50 \mu\text{m}$  and with zero crystal phase mismatch intensity reaches  $20 \text{ GW/cm}^2$ . The second focus is formed in air with the same intensity. This intensity is four orders of magnitude below the ionization threshold of air. In addition, nonlinear refractive index of air is four orders of magnitude lower than that of BBO [86]. It can thus be expected that the self-action of the focused beam propagating in air does not significantly affect the output characteristics of the OPO. In order to explain the measured pulse and spectrum characteristics, the nonlinear phase was computed using the numerical model (equations ((2.59) to (2.61)) by simulating a single pass through the OPO crystal with varying crystal angles. An input signal pulse was injected with experimentally observed steady state OPO parameters at the center of the tuning curve: pulse duration  $\tau = 200 \text{ fs}$  and intracavity average power  $P = 8 \text{ W}$ . A single-pass optical parametric amplifier (OPA) simulation nonlinear phase was used instead of full OPO model, because it produced more consistent results of nonlinear phase while phase mismatch was changed. In OPO case, the steady state pulse shape changes as phase mismatch is induced and this complicates the determination of maximum nonlinear phase in the time-domain. In a single-pass OPA, on the contrary, the signal pulse shape is nearly constant and this leads to easily extractable maximum of time-domain nonlinear phase. As the Kerr-like nonlinearity and OPA are coupled, the crystal rotation changes average power and induced nonlinear phase, but we used fixed pulse parameters to aid better comparison with double-crystal experiment.

Two fused silica glass plates (GP1) are inserted into the cavity to ensure positive group delay dispersion, the total calculated resonator GDD is  $\sim 1800 \text{ fs}^2$  at 860 nm. The results are shown in Fig. 5.2A. The soliton order is calculated by equation (2.99) with fixed dispersive length and nonlinear length calculated from nonlinear phase. The angle is rotated around phase matching angle  $\theta_{\text{OPO LBO}} = 12.7^\circ$  for wavelength 860

nm. The results show that the CQN manifests itself at positive crystal angles, and its magnitude is  $\sim 4$  times larger than intrinsic third-order nonlinearity of the material. Soliton order shows that with a fixed positive group delay dispersion the negative nonlinearity supports 1<sup>st</sup> order soliton (given by red color coding zone I). In contrast, the CQN of zone 0 only partially compensates positive GDD. Fig. 5.2B compares experimentally measured and numerically simulated output spectra. It is evident that lower crystal angles induce positive cascaded nonlinearity which distorts the spectra through self-phase modulation. Larger crystal angles induce negative nonlinearity which, together with positive GDD, produces Gaussian spectra with transform-limited time-bandwidth product (Fig. 5.2D). As the spectra are deformed, the bandwidths are calculated using standard deviation  $2\sigma$ , which for Gaussian spectrum relates to FWHM as  $\sim 2.35\sigma$ . The discrepancy between the measured and numerically simulated spectra could be caused by an overestimated intracavity intensity, because as spatial mode distribution is not accounted for. The overestimated intracavity intensity leads to more severe spectrum distortion caused by the self-phase modulation. The corresponding output power tuning curve and the output pulse durations are presented in Fig. 5.2C. The soliton durations and powers, calculated by equations (2.100) and (2.101) are plotted as zones in red color coding. The output power is too low and pulse duration is too short to support the 1<sup>st</sup> order soliton threshold (zone I) with a fixed resonator GDD. Even though numerical simulation reaches the 1<sup>st</sup> order threshold, it does not show any pronounced differences in power and pulse duration. However, another feature of soliton behavior – the time-bandwidth product – reaches its minimum value of  $\sim 0.44$ . Using this approach, the time-bandwidth product could be reduced to the value of  $\sim 0.55$  from  $\sim 0.8$  with around  $\Delta\theta_{OPO\ LBO} = 0.25^\circ$  angle detuning (or  $\Delta k_{OPO}L = -0.5\pi$ ) and average output power of 720 mW, which is around 20 % lower compared to the exact phase matching  $\Delta k_{OPO}L = 0$ . It must be noted that despite non-optimal operation conditions, the pulse durations are decreased from 215 fs to 185 fs and the pulse peak power is only 5 % lower compared to the phase-matched case.

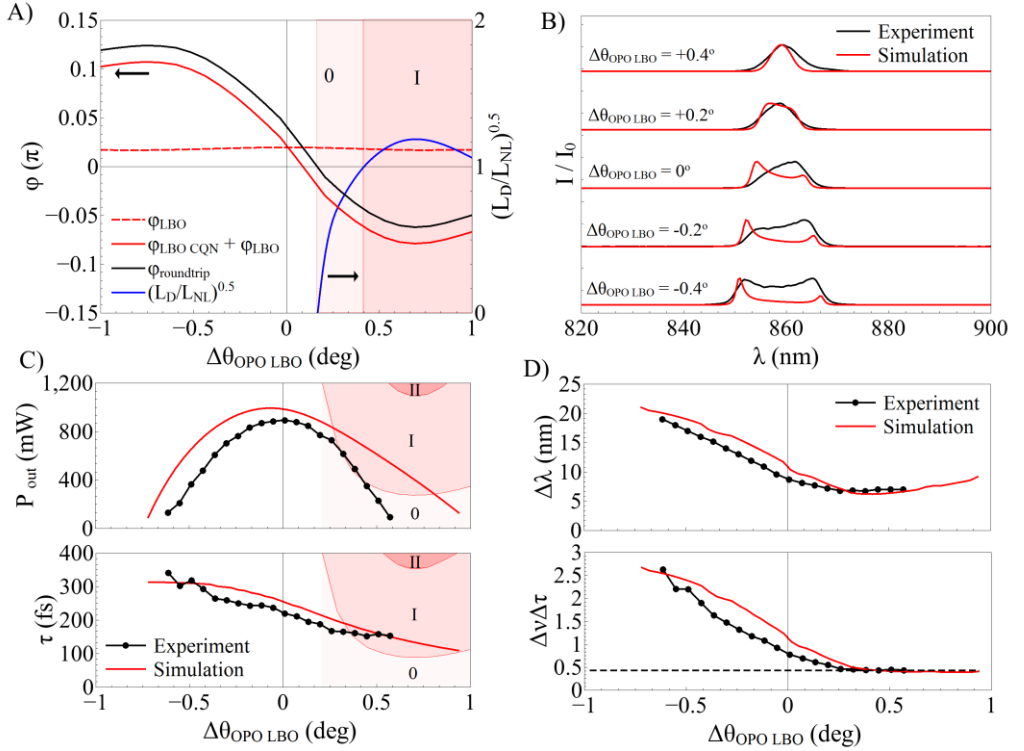


Fig. 5.2. A) OPO nonlinear phase and soliton number dependence on LBO crystal angle. B) Experimental and simulated spectra when OPO LBO crystal angle is detuned from the exact phase matching at 860 nm. C) Experimental and simulated signal output power and pulse duration dependence on crystal angle. D) Experimental and simulated signal spectrum bandwidth (calculated as  $2\sigma$ ) and time-bandwidth product dependence on crystal angle, dashed line indicates minimum for Gaussian pulses TBP  $\sim 0.44$ . In panels A) and C) negative CQN areas (0, I, II) with red color tones indicate output powers / pulse durations large enough to support soliton of corresponding order  $N = 0, 1, 2$ . In all panels signal central wavelength is fixed at 860 nm.

## 5.2.2 Double nonlinear crystal scheme with SHG CQN

In the second part of the experiments, an additional nonlinear BBO crystal is inserted in the second focus, where it is used to frequency-double the signal wave.

Crystal angle is varied to control SHG-induced CQN. The calculated signal intensity reaches  $20 \text{ GW/cm}^2$  in both crystals. The BBO crystal is used for the SHG crystal because of its higher  $d_{\text{eff}}$  coefficient ( $\sim 2 \text{ pm/V}$ ) which induces higher maximum negative cascaded nonlinearity than LBO ( $\sim 0.78 \text{ pm/V}$ ). In the meantime, LBO is used as OPO crystal because of its smaller spatial walk-off value and lower nonlinear refractive index ( $n_2 \sim 2 \times 10^{-20} \text{ m}^2/\text{W}$ , twice lower than BBO, where  $n_2 \sim 4 \times 10^{-20} \text{ m}^2/\text{W}$  [37]). The positive cavity GDD and positive material nonlinearity require that CQN induces negative refraction. In order to operate with as low as possible SHG conversion efficiency (after all, the generated second harmonic of the signal only increases OPO losses), large phase mismatch and short crystal is required as shown in [29]. The shortest signal pulse duration obtained from the part A) experimental setup was 150 fs. Based on this pulse duration, the SHG crystal length was chosen. 150 fs OPO signal pulses have broad enough spectrum to make the local conversion efficiency minimum vanish as minima and maxima are averaged throughout the spectrum amplitudes. This precludes employing the approach of operating the nonlinear crystal in a local conversion efficiency minimum by Keller et al. [29]. The BBO crystal with the length of 0.7 mm was chosen. This length was not limited by spatial walk-off:  $L_{sp \text{ walkoff}} \sim 1.5 \omega / \rho \sim 1.3 \text{ mm}$ , where  $\omega$  is beam radius and  $\rho$  is extraordinary pump beam walk-off as shown in [76], and group velocity walk-off between fundamental and second harmonic length  $L_{gv \text{ walkoff}} = 2 \tau / (v_{FM}^{-1} - v_{SH}^{-1}) \sim 1.9 \text{ mm}$  for pulse length of 150 fs. In order to operate at positive resonator GDD, two fused silica glass plates (GP1) were inserted intracavity, and the calculated GDD is  $\sim 1900 \text{ fs}^2$  at 860 nm.

The LBO crystal angle was fixed at  $\theta_{OPO \text{ LBO}} = 12.7^\circ$  for the optimal conversion efficiency and  $\Delta k_{OPO} L = 0$  for the wavelength of 860 nm. The BBO crystal was rotated to change internal angle  $\pm 4^\circ$  around optimal SHG angle  $\theta_{SHG \text{ BBO}} = 27.3^\circ$  for 860 nm to 430 nm wavelength generation. The central wavelength was fixed at 860 nm by adjusting the resonator length to compensate the tilt of SHG BBO crystal. The resonator was realigned after each adjustment of the crystal angle for the optimal output power. In order to explain the observed characteristics of the pulse, the nonlinear phase was computed using the numerical model (equations (2.59) to (2.61)) by simulating a single pass through the SHG / OPA crystals with varying crystals' angles. The signal pass through the SHG crystal was solved with the equations written for the signal SHG generation, as shown in [87]. An input signal pulse was injected with experimentally observed steady state OPO parameters at the center of the tuning curve: pulse duration  $\tau = 200 \text{ fs}$  and intracavity average power

$P = 8$  W. The results are given in Fig. 5.3A. The soliton order is calculated by the equation (2.99) with a fixed dispersive length and a nonlinear length calculated from the nonlinear phase. The soliton order shows that with a fixed positive group delay dispersion the negative nonlinearity supports the formation of solitons up to the 2<sup>nd</sup> order. Higher order soliton threshold was not reached because the increase in SHG conversion efficiency decreases the intracavity signal power. The results show that the cascaded negative nonlinearity is in the negative crystal angle offset range and its single-pass peak magnitude is  $\sim 8$  times larger than intrinsic (cubic) material nonlinearity. Operating the crystal in double-pass increases the induced negative nonlinearity two-fold, at a cost of two-fold increased losses.

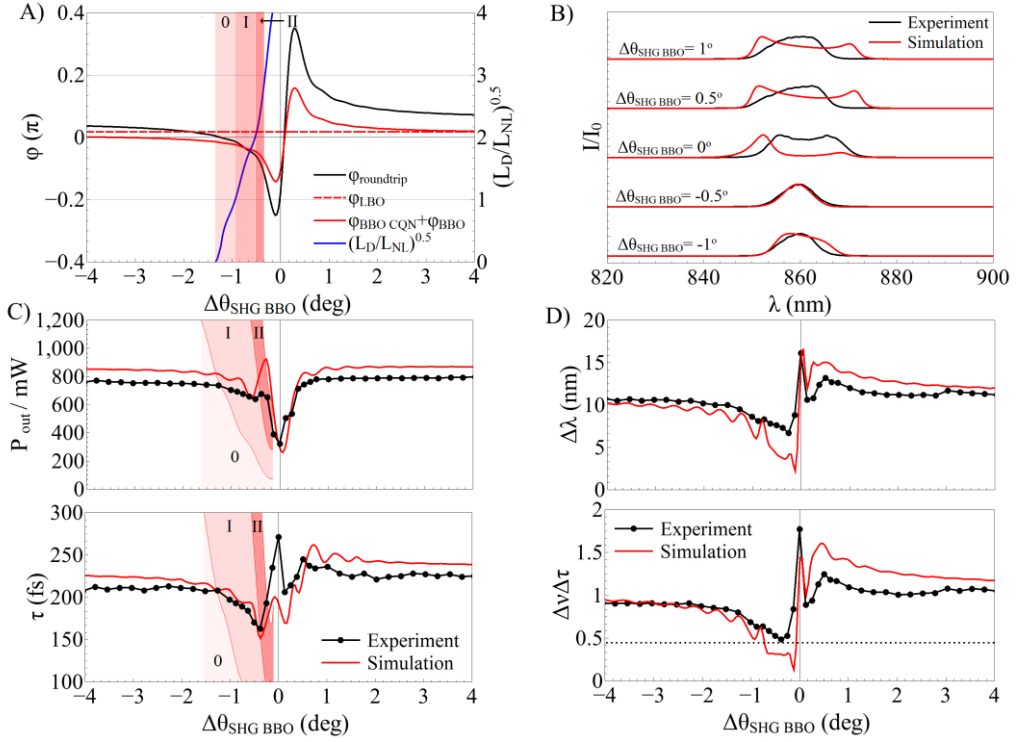


Fig. 5.3. A) OPO LBO and SHG BBO nonlinear phase and soliton number dependence on SHG BBO crystal angle. B) Experimental and simulated spectra when SHG BBO crystal angle is detuned from the exact second harmonic phase matching at 860 nm. C) Experimental and simulated signal output power and pulse duration dependence on SHG BBO crystal angle. D) Experimental and simulated signal spectrum bandwidth and time-bandwidth product dependence on SHG BBO crystal angle. Dashed line indicates minimum for Gaussian pulses TBP $\sim$ 0.44. In panels A) and C) negative CQN areas (0, I, II) with red color tones indicate crystal angles with negative CQN high enough to support soliton of corresponding order  $N = 0, 1, 2$ . In all panels signal central wavelength is fixed at 860 nm and OPO LBO angle is fixed at  $12.7^\circ$  for optimal conversion efficiency to 860 nm.

The measured signal output power and pulse duration are shown in Fig. 5.3C. The nonlinear phase is used for the  $N$ -th order soliton power calculation with fixed experimentally measured pulse duration  $\tau = 200$  fs given by equation (2.101) and  $N$ -th order soliton duration calculation with fixed experimentally measured intracavity average power  $P = 8$  W given by equation (2.100). The main dip at the center of power tuning curve is induced by the SHG losses. The increase of the output power at the zone II angle  $\Delta\theta_{SHGBBO} = -0.3^\circ$  ( $\Delta k_{OPO}L = 4\pi$ ) could be explained by higher pulse energy supported by higher-order soliton as given by equation (2.101). Fig. 5.3B compares the experimentally measured and numerically simulated output spectra. Contrary to the single crystal detuning case, the lower crystal angles induce negative cascaded nonlinearity which balances the cavity group delay dispersion and produces the bandwidth-limited pulses. The discrepancy between measured and numerically simulated spectra could be attributed to the overestimation of simulated intracavity intensity as spatial domain effects are ignored. The curves of spectral bandwidth and time-bandwidth product in Fig. 5.3D correlate well with the spectral narrowing and the reduction in pulse duration induced by the nonlinear phase. At the exact phase matching angle, these parameters suddenly increase again because the spectrum of the pulse becomes distorted. Fig. 5.4 shows the single-pass signal second harmonic wave power as BBO crystal angle is changed. The SHG power curve shifts to the negative crystal angle detuning, because the OPO output power increases at negative crystal offsets. The optimal point is attributed to be  $\Delta\theta_{SHGBBO} = -0.6^\circ$  ( $\Delta k_{SHG}L = 8\pi$ ) at the end of zone I (up to the 2<sup>nd</sup> order soliton formation threshold, zone II). The characteristics of this point can be compared to the case when BBO induces negative nonlinearity equal to its material nonlinearity  $\Delta\theta_{SHGBBO} = -3.8^\circ$  ( $\Delta k_{SHG}L = 48\pi$ ), so that there is no BBO nonlinear effect. At the optimal point, the average output power is ~660 mW, SHG induced power losses are 15 %, pulse duration decreases from 210 fs to 180 fs, and the time-bandwidth product decreases from ~0.98 to ~0.58. In summary, double crystal approach allows to conserve the peak power and the obtained pulses are close to transform-limited.

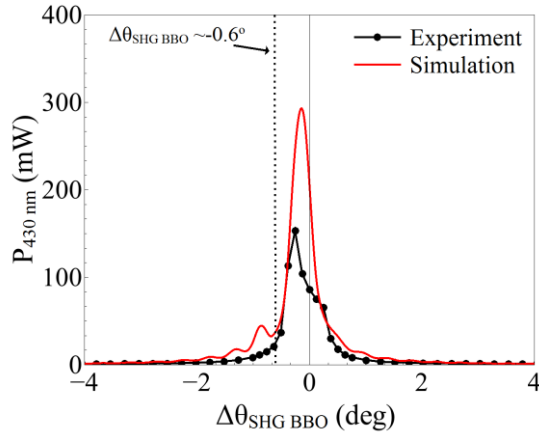


Fig. 5.4. Experimental and simulated single pass signal second harmonic power, dashed line indicates optimal operating point. Signal central wavelength is fixed at 860 nm and OPO LBO angle is fixed at  $12.7^\circ$  for optimal conversion efficiency to 860 nm.

### 5.2.3 Wavelength tuning with DFG and SHG CQN

In the last part of the experiments, the wavelength tuning is demonstrated with two negative CQN approaches, as shown in parts A) and B). In the first case, single LBO OPO crystal is used both as an amplifying medium and a negative DFG CQN source. For the sake of comparison, a 0.5 mm thick fused silica plate is inserted intracavity slightly out of Brewster's angle to induce losses equal to the reflection of SHG BBO crystal at each wavelength. Two intracavity fused silica glass plates (GP1) are inserted to ensure positive resonator GDD, with a roundtrip value of  $\sim 1800 \text{ fs}^2$ . The wavelength is tuned by rotating intracavity LBO crystal. For each wavelength, the LBO crystal angle is offset into negative nonlinearity range for the time-bandwidth product  $< 0.6$  with as high as possible conversion efficiency. In the second case, LBO OPO crystal is used as an amplifying medium and a SHG BBO crystal as a negative SHG CQN source. The 0.5 mm thickness glass plate is rotated to Brewster's angle and two intracavity fused silica glass plates (GP1) are inserted to ensure positive resonator GDD, with a roundtrip value of  $\sim 1900 \text{ fs}^2$ . The wavelength is tuned by rotating intracavity LBO crystal to ensure the maximum

conversion efficiency and negligible LBO-induced CQN. For each wavelength, the SHG BBO crystal angle is optimized for the time-bandwidth product  $<0.6$  with as low as possible SHG conversion efficiency.

Fig. 5.5A shows the BBO SHG and OPO LBO crystal rotation angles in three experimental modes: a) minimum time-bandwidth product with OPO LBO; b) minimum time-bandwidth product with SHG BBO; c) BBO nonlinear phase equals 0 and LBO is in optimal conversion efficiency. Additionally, a BBO SHG and OPO LBO angles are shown for which the frequency conversion is phase matched. The nonlinear phase is extracted from a numerical simulation of a single pass through the SHG / OPO crystal with varying crystal angles with fixed pulse duration  $\tau = 200$  fs and fixed intracavity average power  $P = 6$  W. This power value (25% lower than in the cases A) and B)) was chosen to account for the fact that the OPO power drops when tuning away from the optimum wavelength. The reason for this drop is large reflection losses in the mirror and crystal coatings when operating away from the central wavelength. The central wavelength is varied and the SHG / OPO crystal angles are calculated at which the negative nonlinear phase is high enough to reach the  $N$ -th order soliton threshold, calculated by equation (2.99). These are named as  $N$  zones and plotted in different shades of red. As can be seen from the graph, the experimental SHG / OPO angles are in zone 0 / I (supporting 1<sup>st</sup> order soliton) throughout the entire tuning range.

For SHG BBO, increasing the wavelength requires slightly larger crystal offsets, which lead to lower values of induced negative CQN to compensate the decreasing cavity GDD ( $\sim 2200$  fs<sup>2</sup> at 770 nm and  $\sim 1500$  fs<sup>2</sup> at 970 nm, not including the resonator cavity mirrors). For the same reason, OPO LBO crystal offsets slightly decrease. For a given resonator GDD and intracavity intensity, the optimal wavelength average OPO LBO angle crystal offset is attributed to be  $\Delta\theta_{OPO\ LBO} = 0.25^\circ$  (or  $\Delta k_{OPO}L = -0.5\pi$  at 860 nm). The optimal wavelength average SHG BBO crystal angle offset from the exact phase matching is attributed to be  $\Delta\theta_{SHG\ BBO} = -0.6^\circ$  ( $\Delta k_{SHG}L = 8\pi$  at 860 nm). The OPO LBO and SHG BBO  $\Delta k_{SHG}L$  sign difference stems from the opposite signs of SHG and DFG CQN induced phase shifts as shown in [61, 76].

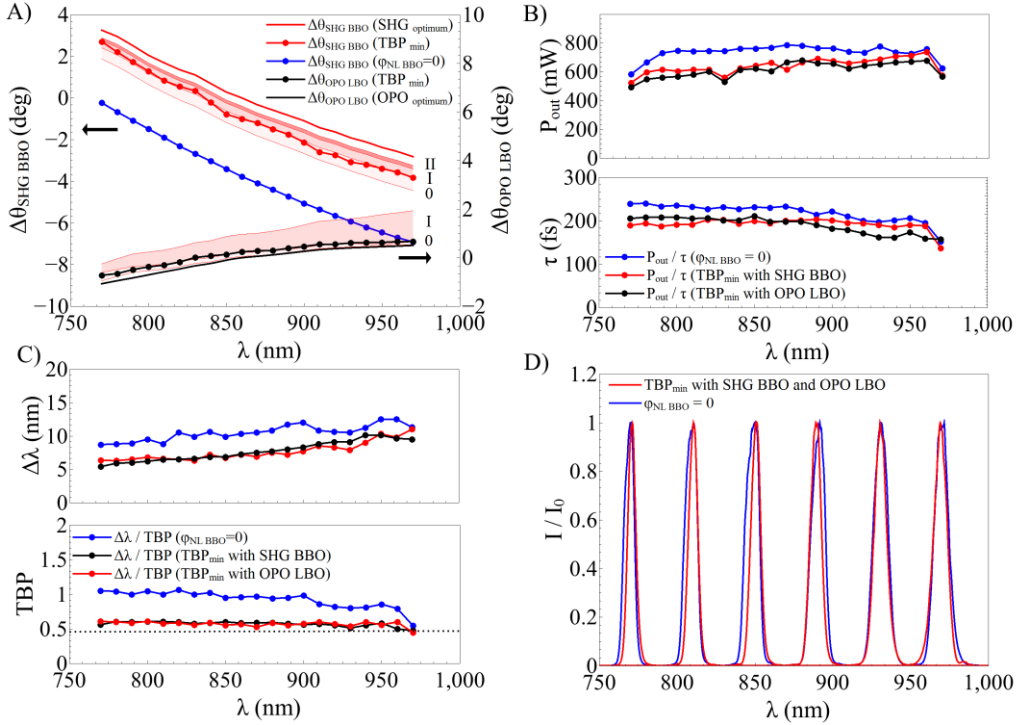


Fig. 5.5. A) Experimental SHG BBO and OPO LBO internal angle dependence on signal wavelength while the wavelength is tuned. Negative CQN areas (0, I, II) with red color tones indicate SHG BBO and OPO LBO angles with negative CQN high enough to support soliton of corresponding order  $N = 0, 1, 2$ . B) Output power and pulse duration dependence on signal wavelength while SHG BBO and OPO LBO angles are varied. C) Dependence of signal bandwidth and time-bandwidth product on the signal wavelength at different SHG BBO and OPO LBO crystal angles. Dashed line indicates minimum for Gaussian pulses TBP $\sim$ 0.44. D) Signal spectra while SHG BBO and OPO LBO angles are varied compared to the case without negative CQN. In all panels crystal angles are tuned in three modes – no negative CQN (blue), negative CQN from SHG BBO (red), negative CQN from OPO LBO (black). In panel D) spectra of negative CQN from SHG BBO and negative CQN from OPO LBO overlap and are shown with red color as one line.

Fig. 5.5B shows the output power and pulse duration of three experimental modes. Up to 25 % power losses are induced in the OPO LBO and up to 20 % power

losses are induced in the SHG BBO cases compared to the power when BBO nonlinear phase equals 0 and LBO is at optimal conversion efficiency. If the optimized AR coatings were used both for LBO and BBO ( $R < 0.25\%$ ), the additional BBO crystal reflection losses would decrease the double-crystal configuration output power by 10 %. On the other hand, the optimal compression SHG losses are 5 % smaller than the phase-mismatched OPO LBO power losses. Therefore, both set-ups would produce similar output powers if optimized AR coatings were used. The compressed pulse durations in both cases are  $\sim 190$  fs compared to the  $\sim 220$  fs when BBO nonlinear phase equals 0, taking an average over the entire investigated spectral range. In other words, the pulses are 15 % shorter with close to transform-limited time-bandwidth product; the average peak power is only slightly decreased. The spectral bandwidths, TBPs and spectra (which are very similar when compressed either with OPO LBO or SHG BBO) of all three experimental modes are shown in Fig. 5.5C and Fig. 5.5D. The uncompressed spectra are broadened and slightly asymmetric, intensity or nonlinearity increase would lead to even more pronounced spectrum deformation induced by SPM as shown in Fig. 5.2B.

In order to investigate the limits of compression on the resonator GDD, the intracavity GDD was varied with multiple numbers of fused silica glass plates (GP1-GP2) at a fixed wavelength of 860 nm. To keep resonator losses the same with decreasing number of glass plates, 0.5 mm thickness glass plate was rotated out of Brewster's angle. In Fig. 5.6A top pane the pulse duration dependence on group delay dispersion is shown. As GDD is increased, crystal is detuned to increase the negative CQN both in SHG BBO (smaller detuning, closer to the optimum SHG conversion efficiency) and in OPO LBO (larger detuning, farther away from the optimum OPO conversion efficiency) experimental modes, shown in the bottom pane of Fig. 5.6A. In both cases, the compensation of the increasing cavity GDD leads to the higher effective resonator losses, in a form of SHG or decreased OPO efficiency. With BBO inducing zero nonlinear phase, increasing amounts of GDD stretch the signal pulse and short pump pulse acts as a frequency domain filter narrowing the pulse duration. Interplay between the uncompensated SPM and GDD lead to distorted spectrum and large values of time-bandwidth product. When either OPO LBO or SHG BBO crystal is used for negative CQN, the pulse durations decrease through all the positive GDD range, but SHG BBO crystal acts as a better compressor for positive GDD values  $> 2000$  fs<sup>2</sup>. In order to explain this, the first order soliton duration was calculated by eq. (2.100) with a fixed intracavity power of  $P = 6$  W and fixed pulse duration  $\tau = 200$  fs. Using experimental crystal offsets, the nonlinear phase was calculated from Fig. 5.2A and Fig. 5.3A. The SHG BBO soliton pulse duration in Fig. 5.6A shows that the increasing values of the GDD are

compensated by negative CQN, which results in a shallower slope of the dependence between the pulse duration and GDD. On the other hand, the LBO OPO soliton pulse duration in Fig. 5.6A shows that the magnitude of the negative CQN is not sufficient to compensate the increasing dispersion. The soliton pulse duration increases linearly vs GDD. Moreover, as the OPO LBO conversion efficiency and negative CQN are inherently coupled, the increase of the negative CQN inhibits short pulse soliton formation because of the decrease of the intracavity power. This explains the pulse duration discrepancy observed in Fig. 5.5B – the SHG BBO compresses the pulses to slightly smaller values with higher values of intracavity GDD (shorter wavelengths), while the OPO LBO compresses the pulses to slightly smaller values with smaller values of intracavity GDD (longer wavelengths).

In a decreasing GDD limit, the shortest pulses we could obtain were around 140 femtoseconds at 860 nm, even though calculated soliton durations reach around 50 fs with 300 fs<sup>2</sup> resonator GDD. We attribute this limit to the dispersive nature of the cascaded nonlinearity. The nonlinear phase oscillation period in a wavelength domain is linked to SHG crystal amplification bandwidth, given by  $\Delta\omega = \pi / L_{crystal} / (k'_{SHG} - k'_{SIG})^{-1}$ , where  $k'_{SHG}$  and  $k'_{SIG}$  are the first derivatives of a wavevector at second harmonic and fundamental wavelength. Calculating in wavelength domain at 860 nm the equation results in  $\Delta\lambda \sim 12$  nm SHG crystal amplification bandwidth, or 95 fs pulse duration. To further reduce the pulse duration, the crystal should be shortened or the group velocity mismatch between fundamental and second harmonic decreased. Bache et al. have shown that the limits to CQN pulse compression to single-cycle is caused by group velocity mismatch between the fundamental wavelength and the second harmonic [88]. Even though OPO regime is far from single cycle, the parallels of the compression limits could be drawn. The phase mismatch has to be higher than the value of  $\Delta k_{sr} = (k'_{SHG} - k'_{SIG})^2 / 2k''_{SHG}$  to ignore the group velocity mismatch caused oscillatory CQN response. In our case for the SHG BBO exactly phase matched to the wavelength of 860 nm, the  $\Delta k_{sr}$  phase mismatch would correspond to a SHG crystal angle offset of  $\Delta\theta_{SHGBBO} = -2.9^\circ$ . At this non-phase matched crystal angle the nonlinear phase oscillations are greatly reduced. On the other hand, at this point with a given OPO intensity reaching  $\sim 20$  GW/cm<sup>2</sup> the negative nonlinearity is too small to compensate the resonator intracavity dispersion and the intrinsic nonlinearity of resonator materials.

## OPO with positive GDD and CQN

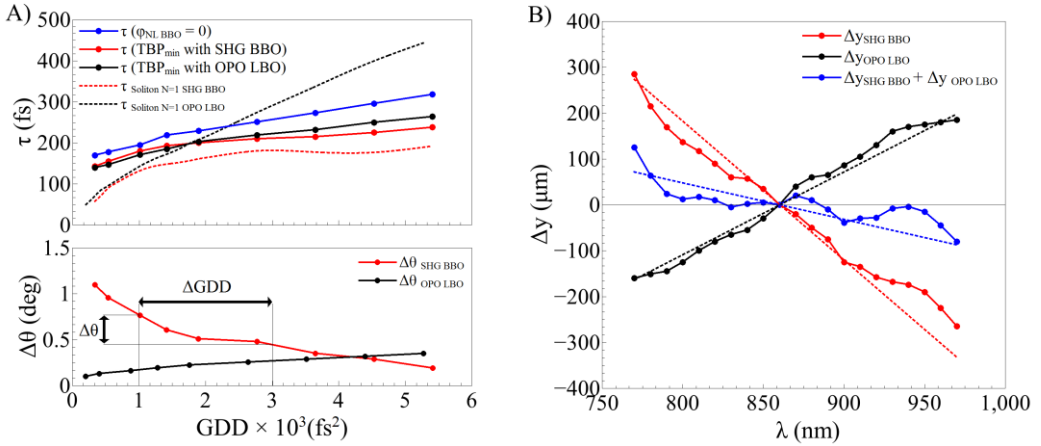


Fig. 5.6. A) Dependence of signal pulse duration, soliton order  $N=1$  pulse duration and experimental SHG BBO and OPO LBO angle detunings on resonator GDD.  $\Delta\text{GDD}$  indicate the  $\pm 1000$  fs<sup>2</sup> range which is compensated by SHG crystal  $\Delta\theta$ . Crystal angles are tuned in three modes – no negative CQN (blue), negative CQN from SHG BBO (red), negative CQN from OPO LBO (black). B) Experimentally measured and calculated (dotted curves) output beam spatial walk off dependence on signal wavelength in three modes - SHG BBO is rotated (red), OPO LBO is rotated (black), both SHG BBO and OPO LBO are rotated simultaneously (blue). In both panes signal wavelength is fixed at 860 nm.

One of the practical considerations of the OPO design is the misalignment of the optical resonator while a birefringent OPO crystal is rotated. This is especially true for a broadly wavelength tunable source where crystal offsets become larger. In our experimental parts A) and B), while the crystals were rotated, the resonator had to be realigned to keep the output beam in the same position. Fig. 5.6B shows the spatial beam walk-offs when the crystals are independently or mutually rotated while the wavelength is changed. The second SHG BBO crystal was inserted with an oppositely orientated crystal axis, so that the rotation would lead to opposite shift of the beam position at the output coupler. In this manner, the simultaneous rotation of both of the crystals leads to the near-compensation of the output beam position. As the compensation is not exact, the beam deviates slightly through the tuning range (given by blue curve) and the pump direction has to be slightly aligned for a maximum output power. By using ABCDEF matrix formalism the beam offsets are calculated with experimental crystal lengths, detunings, and resonator parameters. These are shown in Fig. 5.6B with dotted curves. Empirical position offset ratio

equation of two foci, two crystal resonator can be derived:  $\Delta y_1/\Delta y_2 \sim (L_1 \Delta \theta_1 R_2)/(L_2 \Delta \theta_2 R_1)$ , where  $L_N$ ,  $\Delta \theta_N$ ,  $R_N$  are  $N$  crystal length, crystal detuning angle and mirror radius which forms the focus in crystal  $N$ . The resonator stability is excluded as its contribution to misalignment sensitivity is equal for both crystal detunings. This equation shows that careful choice of resonator mirror radii and crystal lengths would exactly compensate the output beam position shift ( $\Delta y_1/\Delta y_2 = -1$ ) if detuning angle functions are linear. For the experimentally used crystal rotation ranges, the slopes of the LBO and BBO were similar through the wavelength tuning range. As shown in Fig. 5.6A, the compensation of  $\pm 1000 \text{ fs}^2$  intracavity group delay dispersion around resonator GDD of  $2000 \text{ fs}^2$  would require only  $\pm 0.17^\circ$  SHG BBO crystal detuning and would induce only  $\pm 10 \text{ }\mu\text{m}$  beam output position shift. From Fig. 5.3B, the SHG BBO crystal offset of  $\pm 0.17^\circ$  would induce additional average power losses of  $\pm 5\%$ . For comparison, using only OPO LBO to compensate  $\pm 1000 \text{ fs}^2$  at  $2000 \text{ fs}^2$  intracavity GDD requires angle detuning of  $\pm 0.08^\circ$ , which leads to additional average power losses of  $\pm 10\%$ . On the other hand, misalignment issue could as well be solved by generating the OPO with temperature tunable periodically poled nonlinear crystals as OPO and SHG pair, which may provide collinear interaction without resonator misalignment [89].

Both these approaches lead to an efficient way to optimize negative nonlinearity, for instance, to the GDD ripples of broad reflection bandwidth intracavity mirror if operating the device with a broad tuning range. For the spectral widths used in our experiment, the impact of the third order dispersion (TOD) on the spectral phase is weak, and the uncompensated TOD could be ignored. It is important to emphasize that suitable choice of crystal lengths would allow to compensate both the GDD and the spatial beam offsets in a much broader wavelength range. Operating the BBO crystal as a SHG crystal in a wavelength range of 690-1020 nm would require the crystal internal angle rotation range of  $\Delta \theta \sim 10.7^\circ$ . Simultaneous rotation of LBO crystal as an OPO crystal would require rotation of  $\Delta \theta \sim 4^\circ$ , with the rotation angle ratio being similar to the one in our experiment. The same approach can be transferred to different wavelength ranges as long as the OPO and SHG crystal rotation ranges are quasi-linear through the wavelength range.

### 5.3 Summary

The tuning characteristics were investigated of high average power femtosecond optical parametric oscillator with an additional intracavity focus where a nonlinear crystal cut for frequency doubling the signal wave is placed. Either OPO, or second intracavity SHG crystal mismatching leads to negative CQN which can be exploited for soliton generation in a positive GDD resonator to generate pulses with minimum time-bandwidth product. The mode of OPO crystal mismatching leads to a simple approach, with a cost of higher power losses, coupled amplification / nonlinearity, and a spatial beam position walk-off when crystal is tuned. Decoupling of optical parametric amplification part and negative nonlinearity with an additional SHG crystal allows independent control of both of these parameters to operate in a solitonic regime with varying wavelength. Throughout the wavelength tuning range, the time bandwidth product  $<0.6$  and pulse durations  $<200$  fs were demonstrated while the CQN induced average power losses were less than 20 % with peak power conserved. Two-crystal approach leads to a two-fold improvement: quasi passive output beam stabilization while both crystals are rotated in opposite directions as wavelength is changed; a way to compensate for varying levels of the resonator intracavity group delay dispersion (GDD offsets of  $\pm 1000$  fs<sup>2</sup> with  $\pm 5$  % SHG power losses) with negligible beam position drift.

## 6 Soliton formation effects with GDD compensated CQN

As shown in chapters 4 and 5, evidence of the CQN impact on femtosecond optical parametric oscillators pulse characteristics was observed while operating with negative and positive group delay dispersion in a soliton regime [23, 82]. If intracavity intensity is high enough, higher order solitons can be supported by the cavity. OPOs operating in a multi-soliton regime exhibit multi-pulsing and time and frequency domain oscillations as reported in [74, 77, 90 – 92]. Recently, a number of works have investigated the generation of solitons and solitonic behaviour in synchronously pumped femtosecond OPOs. In a work by Ning et al. [91], degenerate OPO was investigated with negligible cavity GDD, multiple solitons were generated by matching nonlinear group delay to linear group delay. The finite pump gain time domain window allowed the formation of the solitons. In a work by O'Donnell et al. [92], solitons were generated in a single-mode fiber-feedback cavity in the spectral range of anomalous dispersion. In normal dispersion regime, solitons were generated by finite pump gain window and dispersive wave side-bands were demonstrated. In a work by Tamuliene et al. [93], chaotic and stable oscillations were numerically simulated, with threshold / period of oscillations depending on pulse energy, intracavity dispersion and cavity nonlinearity. In this dissertation chapter 5, the wavelength tuning characteristics were investigated of an OPO with positive resonator dispersion and intracavity negative CQN adjustable up to 2<sup>nd</sup> soliton threshold. In this chapter, we demonstrate the exploitation of CQN in a femtosecond optical parametric oscillator while operating with a positive group delay dispersion and its impact to higher order soliton regimes. The resonator was designed to include a second intracavity focus where another nonlinear crystal could be placed. The second nonlinear crystal was chosen to frequency double the signal wave, and the phase matching was detuned to low conversion efficiency. Experimentally, the crystal was rotated or the central wavelength was changed, in both cases resulting in a phase mismatch. Higher order soliton formation was evident near the zero of phase mismatch. Further investigation has revealed that decreasing second harmonic crystal phase mismatch to zero leads to CQN large enough to reach 3rd order soliton formation threshold. The soliton dynamics leads to output power increase, pulse splitting under perturbations of higher orders of nonlinear phase, self-phase modulation phase matched dispersive wave formation, time and spectral domain oscillations with soliton period. These results provide a deeper understanding of the

effects observable in a high power all positive dispersion femtosecond optical parametric oscillator with a tunable negative nonlinearity.

Parts of the material covered in this chapter have been published in publications P3 and P6.

## 6.1 Experimental procedures

The used optical setup is identical to the one shown in Fig. 5.1 with differences described below. Fused silica windows GP1 - GP2 (14 mm thickness, AR coated for 650-1000 nm,  $R < 0.5\%$ ) allowed to coarsely vary positive group velocity dispersion of the resonator. In the crystal rotation experiments, two fused silica glass plates were used, and the total calculated group delay dispersion of the cavity was  $\sim 1900 \text{ fs}^2$  at 860 nm. In the wavelength tuning experiment, the resonator group delay dispersion was varied by using one ( $\sim 1200 \text{ fs}^2$ ), two ( $\sim 2000 \text{ fs}^2$ ) and four ( $\sim 3700 \text{ fs}^2$ ) windows.

OPO crystal was 2.5 mm thick LBO (type I,  $\theta = 14^\circ$ , Eksma Optics). The crystal was AR coated at 1030+515 nm. BBO crystal was used in the second focus (type I,  $\theta = 24^\circ$ , Eksma Optics), two different thicknesses were investigated – 0.7 mm and 2 mm. The crystals were AR coated at 1030+515 nm. The reflection coefficient at the signal wavelength range 770-970 nm was experimentally measured to vary from 2.5% (770 nm) to 1% (970 nm) for BBO and from 5% (770 nm) to 2% (970 nm) for LBO. Both crystals were mounted on precision rotation stages allowing the precise control of the phase matching angle, which was later recalculated to internal angle. The thicker crystal length (2 mm BBO) was chosen based on group velocity walk-off between fundamental and second harmonic length  $L_{gv \text{ walkoff}} = 2\tau / (v_{FM}^{-1} - v_{SH}^{-1}) \sim 1.9 \text{ mm}$  for pulse length of 150 fs. The calculated spatial walk-off length  $L_{sp \text{ walkoff}} \sim 1.5 \omega_{radius} \rho_{walkoff} \sim 1.5 \text{ mm}$  should limit the effective crystal length while operating with the thicker SHG crystal, and was accounted for in numerical simulations. The length of the thinner crystal (0.7 mm) was chosen to limit the negative CQN and prevent the formation of higher order solitons.

## 6.2 Results and discussion

The experimental results are divided into three sections: A) CQN tuning by the SHG BBO crystal rotation with fixed cavity GDD. B) CQN tuning by wavelength change with varying amounts of cavity GDD. C) CQN tuning spectral and time-domain behaviour. In section A), an unexpected output power increase was observed when negative nonlinearity was induced by tuning the crystal angle towards exact SHG. In section B), wavelength was finely tuned around the exact SHG phase matching to investigate if an increase of output power correlates with calculated power thresholds of the higher order solitons. The GDD was varied to test if an increasing GDD leads to a shift of soliton formation thresholds. In section C), time and pulse domain behaviour of higher order solitons was investigated, with observed effects of pulse splitting under perturbations of higher orders of nonlinear phase and stable time / spectral domain oscillations with soliton period.

### 6.2.1 CQN tuning by crystal rotation with fixed cavity GDD

In the first section of the results, the LBO crystal angle was fixed at  $\theta_{OPO\ LBO} = 12.7^\circ$  for the optimal conversion efficiency and  $\Delta k_{OPO} L = 0$  for the wavelength of 860 nm. The BBO crystal was rotated to change internal angle  $\pm 5^\circ$  around the optimal SHG angle  $\theta_{SHG\ BBO} = 27.3^\circ$  for 860 nm to 430 nm wavelength generation. The central wavelength was fixed at 860 nm by changing the resonator length as SHG BBO crystal was adjusted. The measured signal output power and pulse duration for both of the SHG BBO crystal lengths are shown in Fig. 6.1. The pulse durations follow the classical CQN induced nonlinear refractive index behaviour  $n_2^{eff} \sim 1/\Delta k$ , switching from negative to positive and compensating / adding up to the positive cavity SPM. The positive material's nonlinearity is exactly compensated by the CQN induced negative one at the two SHG BBO crystal rotation points – near the exact phase matching and at the negative angle offsets, denoted by the start of zone 0 in both panels Fig. 6.1B, D. At these two points the total cavity nonlinearity is 0 and the pulse characteristics are determined solely by the linear dispersion and OPA gain. The pulse duration increases at the exact phase matching

because of the increased SHG efficiency and the distortion of the signal spectrum. In the negative crystal angle offset range, the CQN exceeds material nonlinearity and the total cavity nonlinearity becomes negative. It compensates the positive cavity GDD and allows soliton formation. In order to explain the observed characteristics of the pulses, the nonlinear phase is computed using the numerical model (2.59) to (2.61)) with the equations written for the signal SHG generation, as shown in [87], by simulating a single pass through the SHG crystal with varying SHG BBO crystals' angles. An input signal pulse is injected with approximate experimentally observed steady state OPO signal pulse parameters near the soliton formation threshold: pulse duration  $\tau = 200$  fs and intracavity average power  $P = 8$  W. Even though the experimental pulse duration and intracavity power vary with changing SHG BBO crystal angles, an approximate fixed values are used to more intuitively interpret the nonlinear phase and soliton power / duration dependence on the crystal angle. The nonlinear phase is used for the  $N$ -th order soliton power and  $N$ -th order soliton duration calculation given by the equations (2.101) and (2.100). In order to operate at a positive resonator GDD, two glass plates are inserted intracavity, and the calculated GDD is  $\sim 2000$  fs<sup>2</sup> at 860 nm. The comparison of the 0.7 mm vs 2 mm SHG BBO crystal lengths (Fig. 6.1A,B vs. Fig. 6.1C,D) reveals these features of the thinner crystal: decreased SHG efficiency at the exact phase matching, pronounced numerically simulated SHG efficiency oscillations further away from the exact phase matching, narrower crystal angle rotation range inducing negative CQN, and smaller number of the soliton orders which are supported by a cavity. The optimal operating point for the 0.7 mm BBO crystal is attributed to be up to 2<sup>nd</sup> order soliton formation threshold (end of zone I) at  $\Delta\theta_{SHG\ BBO} = -0.6^\circ$  ( $\Delta k_{SHG}L = 8\pi$ ). At that point the SHG induced power losses are 15%, pulse duration is compressed from 210 fs to 180 fs, time-bandwidth product decreases from  $\sim 0.98$  to  $\sim 0.58$ . The optimal point of the 2 mm BBO crystal (end of zone I) is attributed to be at  $\Delta\theta_{SHG\ BBO} = -1^\circ$  ( $\Delta k_{SHG}L = 13\pi$ ). The SHG induced power losses are 10%, pulse duration is compressed from 240 fs to 200 fs, time-bandwidth product decreases from 0.95 to 0.55. The thinner crystal compresses the pulses to shorter durations with near optimum time-bandwidth product, but induces larger SHG losses. The thicker crystal induces negative CQN large enough to investigate higher-order soliton effects.

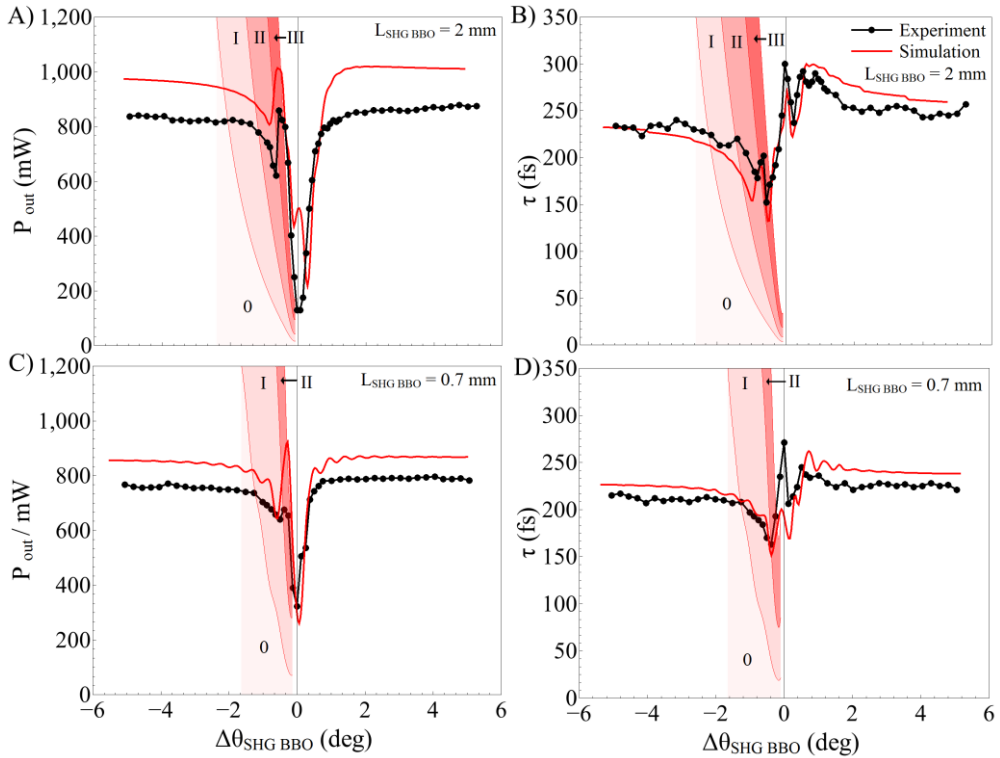


Fig. 6.1. A), C) – experimental and simulated signal output power dependence on SHG BBO crystal angle with two SHG crystal lengths. B), D) – experimental and simulated signal pulse duration dependence on SHG BBO crystal angle with two different crystal lengths. In both panels negative CQN areas (0, I, II, III) with red color tones indicate output powers / pulse durations large enough to support soliton of corresponding order  $N = 0, 1, 2, 3$ . In both panels signal central wavelength is fixed at 860 nm and OPO LBO angle is fixed at  $12.7^\circ$  for optimal conversion efficiency to 860 nm.

For both crystal thicknesses, the main dip at the center of power tuning curve is induced by the SHG losses. Unexpectedly, the output power for the thicker crystal abruptly increases at the end of soliton zone II angle  $\Delta\theta_{SHG\ BBO} = -0.6^\circ$  ( $\Delta k_{SHG}L = 8\pi$ ) and the pulse durations increase just before this point at  $\Delta\theta_{SHG\ BBO} = -0.8^\circ$  ( $\Delta k_{SHG}L = 10.5\pi$ ), at the middle of zone II. The thin crystal experiment shows only a small power increase (Fig. 6.1C, black dots), whereas the simulation indicates sharp increase (Fig. 6.1C, solid red curve). This mismatch could be caused by an

overestimated intracavity intensity in numerical modelling. The power increase correlates with soliton formation threshold (as will be shown in chapter 6.2.2) and further investigation was needed to clarify this peculiar effect.

## 6.2.2 CQN tuning by central wavelength change with varying intracavity GDD

In order to understand the observed power increase near the exact SHG phase matching, further experiments were carried out with finely tuned CQN by varying central wavelength. Moving the output coupler placed on a translation stage, enables the synchronous pumping condition for different signal wavelengths if the gain bandwidth is large enough. Under small resonator length changes, the generation shifts to signal wavelengths with larger or smaller group velocities, determined by the cavity GDD. The gain bandwidth of the OPO crystal is inversely proportional to the crystal length and difference of inverse group velocities of signal and idler waves. Calculating the LBO crystal gain bandwidth at the signal wavelength of 860 nm results in a bandwidth of  $\sim 100$  nm. If this tunable 810-910 nm signal range is used for the second harmonic generation with a fixed SHG BBO crystal angle, the covered SHG BBO phase mismatch range is  $\Delta k_{SHG}L = \pm 20\pi$  at wavelengths of  $860 \pm 50$  nm. One important advantage of wavelength tuning by changing cavity length instead of crystal angle is an ability to probe the impact of nonlinearity without the realignment of the cavity.

During wavelength tuning experiment, the LBO crystal angle was fixed for the optimal conversion efficiency ( $\Delta k_{OPO}L = 0$ ) for the wavelength of 860 nm and BBO crystal was fixed at  $\Delta\theta_{SHGBBO} = -0.6^\circ$  ( $\Delta k_{SHG}L = 8\pi$ ) which resulted in  $\Delta k_{SHG}L = 0$  for the wavelength of 881 nm. Changing the signal wavelength around 860 nm with small steps from 830 nm up to the SHG wavelength allowed probing the pulse and spectrum formation characteristics under increasing amount of negative cascaded nonlinearity. As negative nonlinearity was induced together with positive cavity group delay dispersion, soliton generation could be presumed whenever soliton condition was satisfied. The soliton order was calculated from equation (2.99) with a fixed dispersive length (with  $\sim 2000$  fs<sup>2</sup> resonator GDD and  $\tau = 180$  fs) and nonlinear length estimated from the nonlinear phase. The nonlinear phase was computed using the numerical model (2.59) to (2.61)) with the equations written for

the signal SHG generation, as shown in [87], by simulating a single pass through the OPA and SHG crystal with varying signal wavelengths. An input signal pulse is injected with approximate experimentally observed steady state OPO signal pulse parameters near the higher-order soliton formation threshold: pulse duration  $\tau = 180$  fs and intracavity average power  $P = 5.5$  W. The nonlinear phase and the resultant soliton order is shown in Fig. 6.2A. The same nonlinear phase calculation procedure was carried out for a thin BBO crystal, shown in Fig. 6.2B. As a thinner crystal has larger coherence length, the oscillatory nonlinear phase structure is more evident. The value of nonlinear phase is lower in the thinner crystal and the roundtrip phase is just sufficient to reach 1<sup>st</sup> order soliton threshold. The results also show that for a thin BBO crystal the SHG CQN single pass peak phase shift is  $\sim 8$  times larger than phase shift induced by the intrinsic cubic nonlinearity of the material. The maximum LBO DFG-induced CQN single-pass phase shift is  $\sim 4$  times larger than intrinsic material nonlinearity's phase shift. If crystal length ratio is taken into account, the BBO has  $\sim 5.6$  larger than LBO cascaded nonlinearity to material's nonlinearity ratio. Inserting the effective nonlinearity  $d_{\text{eff}}$  of LBO (0.78 pm/V) and of BBO (2 pm/V) into an approximate CQN nonlinear refractive index scaling relationship  $d_{\text{eff}}^2 / \Delta k$  produces a ratio of  $\sim 6.5$ . This result is consistent with the simulation values.

Changing wavelength leads not only to the BBO SHG cascaded nonlinearity but also to the LBO DFG-induced cascaded nonlinearity as  $\Delta k_{\text{OPO}} L = 0$  is only for a wavelength 860 nm. It is interesting to note that for a thick crystal the mutual effect of SHG and DFG induced nonlinearities leads to the plateau of negative nonlinearity in the range of 800 nm to 850 nm, while at longer wavelengths, SHG nonlinearity starts to dominate as shown in Fig. 6.2A.

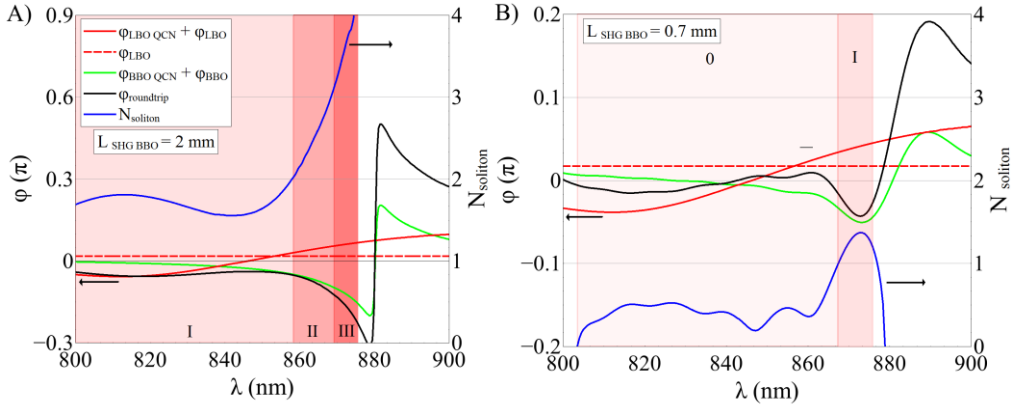


Fig. 6.2. A), B): OPO LBO and SHG BBO nonlinear phase and soliton number dependence on the signal wavelength with intracavity GDD  $\sim 2000 \text{ fs}^2$  and with two different SHG BBO crystal lengths. Negative CQN areas (0, I, II, III) colored with different red shades indicate wavelengths with negative CQN high enough to support soliton of corresponding order  $N = 0, 1, 2, 3$ . In both panels, OPO crystal angle is fixed at  $12.7^\circ$  for optimal conversion efficiency to 860 nm and SHG crystal angle is fixed at  $26.6^\circ$  for optimal conversion efficiency to 881 nm.

The experimentally measured output power and pulse duration dependence on the wavelength with differing amounts of intracavity GDD is shown in Fig. 6.3 for both crystal lengths. The cavity GDD was varied by inserting different numbers of fused silica plates: a) one plate ( $\sim 1200 \text{ fs}^2$ ), b) two plates ( $\sim 2000 \text{ fs}^2$ ) and c) four plates ( $\sim 3700 \text{ fs}^2$ ). The nonlinear phase was computed using the numerical model (1) to (3) and (2.59) to (2.61)) with the equations written for the signal SHG generation, as shown in [87], by simulating a single pass through the OPA and SHG crystal with varying signal wavelengths. An input signal pulse is injected with approximate experimentally observed steady state OPO signal pulse parameters near the higher-order soliton formation threshold with different amounts of intracavity GDD. The output powers at fixed pulse durations a)  $\tau = 140 \text{ fs}$ , b)  $\tau = 180 \text{ fs}$ , c)  $\tau = 240 \text{ fs}$  and pulse durations at fixed intracavity power values a)  $P = 5 \text{ W}$ , b)  $P = 5.5 \text{ W}$ , c)  $P = 6 \text{ W}$  were investigated. Equations (2.101) and (2.100) provided estimates of the parameters left unfixed. The estimated nonlinear phase was used for calculating the output power and duration of the  $N$ -th order soliton with different amounts of intracavity GDD. The  $N$ -th order soliton extra-cavity powers and durations are depicted as  $N$  zones and are colored in different shades of red in Fig. 6.3.

Results of thin and thick crystal show the impact of the soliton formation on the output power and pulse duration. It is evident, that the thin crystal output power results in Fig. 6.3A, C, E show no abrupt power changes while the wavelength is tuned towards the exact SHG wavelength. The output power decreases as the exact SHG phase matching wavelength is approached and the SHG losses increase. In other words, the negative CQN of the thin crystal is too low to support higher order solitons with their correspondingly higher output powers.

Changing the cavity GDD enables probing the soliton threshold powers' and durations' dependence on cavity dispersion. Experimental results of Fig. 6.3A, C, E show that with increasing GDD, the threshold of the abrupt power change shifts to the longer wavelengths and correspondingly higher cascaded negative nonlinearities. With varying values of intracavity GDD the abrupt changes of the output power correlates well with multiple order soliton energy calculations, especially in the low GDD range (Fig. 6.3A through D). The abrupt changes of the output power match the thresholds of the transitions from 1<sup>st</sup> (zone I) to the 2<sup>nd</sup> (zone II) order soliton and from the 2<sup>nd</sup> (zone II) to 3<sup>rd</sup> (zone II) order soliton. This indicates that the soliton formation mechanism should be responsible for the measured power and pulse duration peculiarities.

### Soliton formation effects with GDD compensated CQN

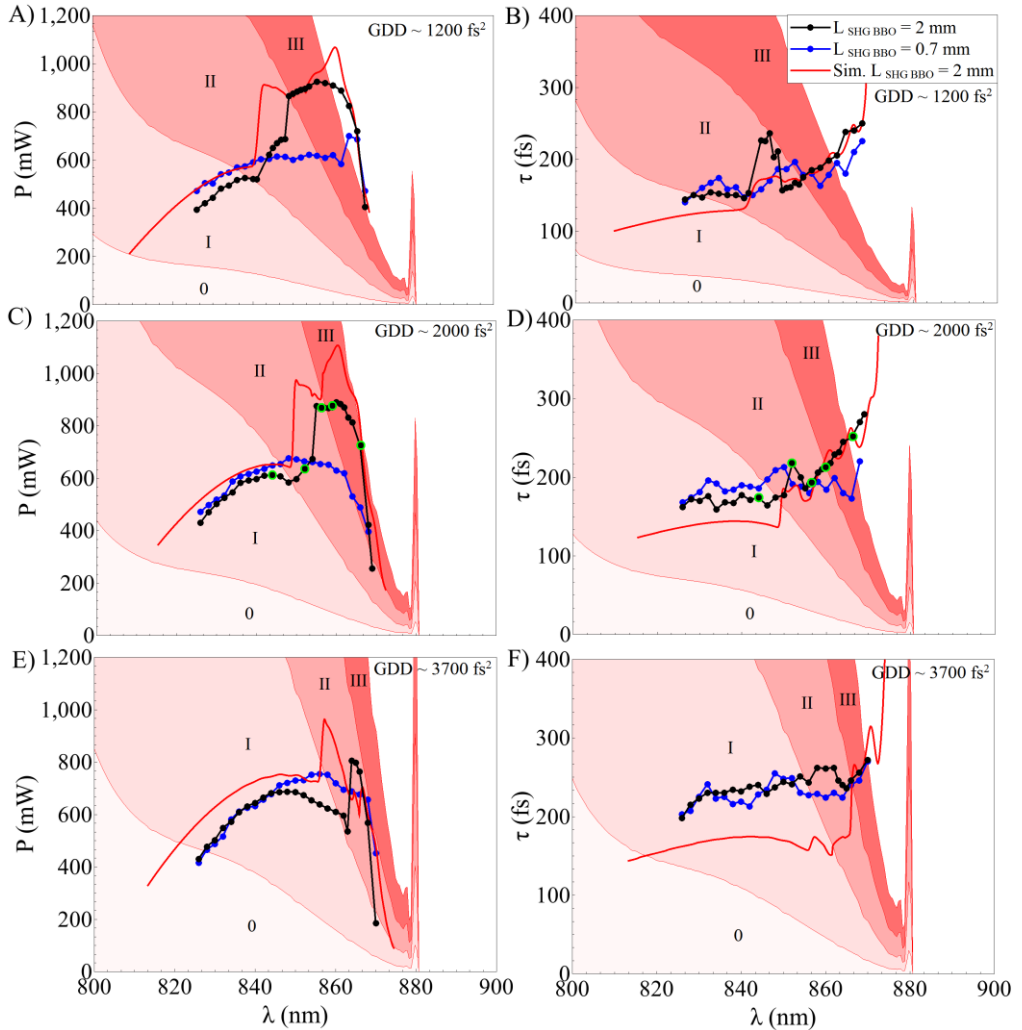


Fig. 6.3. A), C), E): experimental and simulated signal output power dependence on signal wavelength with varying levels of intracavity GDD. B), D), F): experimental and simulated signal pulse duration dependence on signal wavelength with varying levels of intracavity GDD. In all panels negative CQN areas (0, I, II, III) with red color tones indicate output powers / pulse durations large enough to support soliton of corresponding order  $N = 0, 1, 2, 3$ . In all panels OPO LBO angle is fixed at  $12.7^\circ$  for optimal conversion efficiency to 860 nm and SHG BBO angle is fixed at  $26.6^\circ$  for optimal conversion efficiency to 881 nm. In all panels, experimental results of SHG BBO crystal lengths 0.7 mm and 2 mm are shown with numerical simulation of SHG BBO crystal length of 2 mm.

The calculated soliton output power transition from zone II to zone III with the largest GDD of  $\sim 3700 \text{ fs}^2$  in Fig. 6.3E is shifted to the longer wavelengths compared to the experimental results. According to the equation (2.101), to match the calculated and measured soliton power, one needs to increase the pulse duration or decrease of the intracavity GDD. The increase of the pulse duration alone does not match the calculated soliton power to the experimental results. This observation motivated seeking for an additional nonlinear phase-induced GDD term, which would explain the experimental results.

The 2 mm length SHG BBO nonlinear phase dependence on wavelength with varying intracavity GDD is shown in Fig. 6.4A. Calculating the first derivative of the frequency-dependent nonlinear phase of the SHG BBO crystal provides the nonlinear phase-induced group delay, shown in Fig. 6.4B. The second derivative of the nonlinear phase results in the nonlinear phase-induced GDD, shown in Fig. 6.4C as the sum of the nonlinear GDD term and linear resonator GDD. The oscillation frequency is related to the SHG crystal acceptance bandwidth and the peaks of the oscillations in frequency domain are separated by  $\Delta\omega = \pi / L_{crystal} / (k'_{SHG} - k'_{SIG})$ , where  $k'_{SHG}$  and  $k'_{SIG}$  are the first frequency derivatives of the wavevector at the second harmonic and fundamental wavelength. In wavelength domain, the equation results in  $\Delta\lambda \sim 5 \text{ nm}$  oscillation period at 860 nm for a thick 2 mm BBO crystal. From Fig. 6.4C, it is evident that the increase of the resonator GDD leads to the increase in the oscillations of the nonlinear term. As the resonator GDD increases, the pulse bandwidth is reduced, and the oscillatory structure of the nonlinear phase is no longer averaged out by the different frequencies contained in the pulse spectrum. Additional moving average filter (with spectrum bandwidth) is applied to the nonlinear GDD to recover average nonlinear GDD “seen” by the pulse. The average nonlinear GDD term is negative, so the total resonator GDD (sum of linear positive and nonlinear negative GDD) is decreasing rapidly with increasing wavelength. At the wavelength of 865 nm, the averaged nonlinear negative GDD term is of the order of  $1000 \text{ fs}^2$ , so the total GDD is decreased by 25%. This value, together with the increase of the output power, would shift the calculated soliton powers (Fig. 6.3E) to the shorter wavelengths and better match the experimental results.

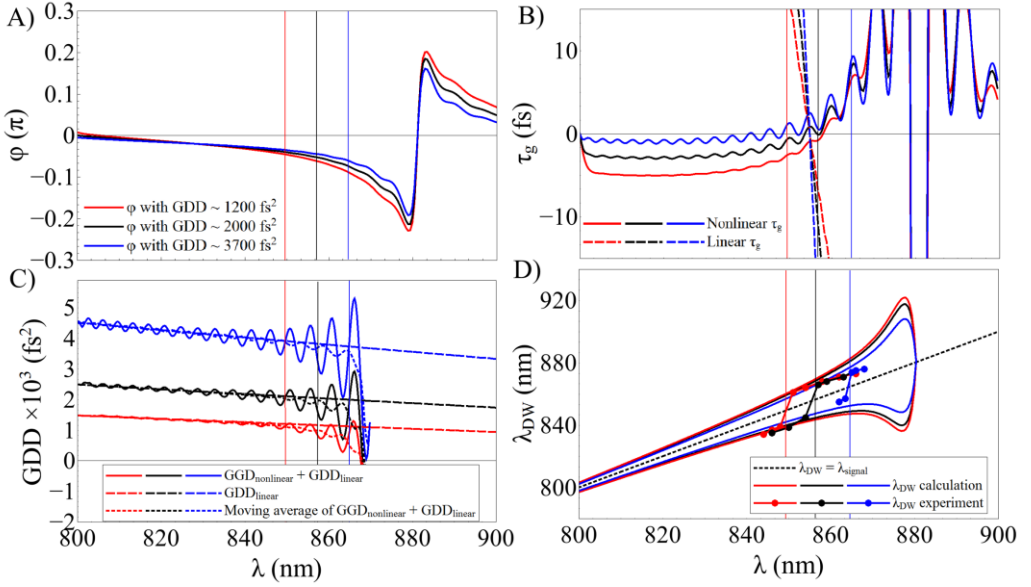


Fig. 6.4. A) Calculated 2 mm thickness SHG BBO crystal nonlinear phase dependence on wavelength with varying amounts of intracavity GDD. B): linear (dashed lines) and nonlinear (solid lines) group delay dependence on signal wavelength, nonlinear delay is calculated as the first frequency derivative of the nonlinear phase. C): linear (dashed lines), nonlinear + linear (solid lines) and moving filter average of nonlinear + linear (dotted lines) GDD as a function of signal wavelength, nonlinear GDD is calculated as the second frequency derivative of the nonlinear phase. D): experimental and calculated dispersive wave wavelength dependence on the signal central wavelength. In all panels vertical lines indicate wavelengths of experimentally observed shift of 2<sup>nd</sup> to 3<sup>rd</sup> order soliton, all line colors are plotted corresponding to varying levels of intracavity GDD. In all panels, OPO crystal angle is fixed at 12.7° for optimal conversion efficiency to 860 nm and SHG crystal angle is fixed at 26.6° for optimal conversion efficiency to 881 nm.

When soliton energy is increased above the soliton threshold, higher order soliton sheds part of its energy to a dispersive wave at a specific frequency determined by the higher orders of dispersion as shown in [47, 94]. The energy of the dispersive wave remains negligible until an appropriate phase-matching condition is satisfied [95]:

$$k(\omega) = k(\omega_s) + k'(\omega - \omega_s) - \frac{1}{2} \frac{n_2^{\text{eff}} \omega_s}{c A_{\text{eff}}} P_0, \quad (6.1)$$

where  $\omega_s$  is a soliton frequency,  $k'$  is a first derivative of a wave vector. The phase matching condition states that in a perturbing medium, wave vectors of a linear dispersive wave and a soliton with a nonlinear phase term should be equal. When soliton wavelength is in positive group delay dispersion range, dispersive wave is emitted in negative group velocity range. In our experiment, the used soliton wavelength range of 770-970 nm in BBO crystal should emit a corresponding range of 2940-1800 nm some of which falls in an absorption band of the crystal (>2600 nm), as shown in [95]. On the other hand, negative nonlinearity allows phase matching in positive group delay dispersion range, albeit with much smaller wavelength offsets proportional to the magnitude of the nonlinear phase. This effect has been shown equivalent to self-phase modulation phase matched degenerate four-wave mixing with Stokes and anti-Stokes components emerging as signal and idler beams [96]. Naming these generated sidebands “dispersive waves” is questionable as they are partially dispersive because of their low energy content, but we used the “dispersive wave” terminology throughout the paper.

Fig. 6.4D shows calculated dispersive wave wavelengths as Stokes and anti-Stokes branches and experimental wavelength shifts for a thick 2 mm BBO crystal. Different colors correspond to different amounts of positive cavity GDD. The dispersive wave solutions are obtained from the equation (6.1) with SHG BBO crystal wavevector and nonlinear phase from single pass SHG BBO crystal shown in Fig. 6.4A. Only SHG BBO crystal was included as it is the main contributor to the negative nonlinearity, which allows dispersive wave generation phase matched by the self-phase modulation. It is interesting to note that even though dispersive wave phase matching supports both Stokes and anti-Stokes branches, experimentally only one of them is observed at any one time. The anti-Stokes shifts to Stokes after soliton transitions from 2<sup>nd</sup> to 3<sup>rd</sup> order soliton with higher intracavity pulse energy. The shift could be explained by recalling that both Stokes and anti-Stokes waves fall under the amplification bandwidth of the LBO crystal ( $\Delta\lambda \sim 100$  nm at 860 nm), and they may get amplified by the pump in LBO crystal if their group velocity is matched to the signal synchronous to pump. As shown in [97 - 99], the nonlinear phase of the CQN induces an intensity dependent group velocity which may even lead to positive or negative self-steepening, hence delaying or accelerating the peak of the pulse. Fig. 6.4B shows nonlinear phase-induced group delay, while the linear group delay is shown by dashed lines with much higher slope. It is evident that nonlinear group delay increases with increasing wavelength and has a sign opposite to the linear

group delay. Even though the induced nonlinear delay is small compared to the linear one, this could be the reason why red shifted Stokes pulse could be better group velocity matched to the signal. Furthermore, as shown in [100], in the presence of large group velocity mismatch, the CQN induce non-instantaneous nonlinear phase shifts which mimic the Raman response and act as a controllable red- or blue-shift of the spectrum. Further investigation is needed to confirm if these effects are contributing to the experimentally observed red- or blue- shifted Stokes and anti-Stokes dispersive waves in OPO.

It is interesting to compare the Fig. 6.4C and Fig. 6.4D: with varying cavity GDD, the transitions from 2<sup>nd</sup> to 3<sup>rd</sup> order soliton happens at the nodes of nonlinear GDD, the vertical red, blue and black lines indicate these points and correspond to increasing values of linear GDD. The nonlinear third order dispersion is maximum at these points, so this could be an indicative feature of soliton fission induced by nonlinear third order dispersion, as suggested in [47].

As shown in this section, soliton dynamics lead to a wide range of physical effects which are observed with slow averaging detectors (spectrometer, autocorrelator, power meter). Pulse to pulse measurement with oscilloscope should be done for completeness and this was investigated in the last experimental results' section.

### 6.2.3 CQN tuning spectral and time-domain behaviour

To investigate the higher order soliton transitions further, pulse spectra and oscilloscope traces were recorded at the transition points indicated by green circles in Fig. 6.3C and Fig. 6.3D. The cavity was configured to include 2 glass plates ( $\sim 2000 \text{ fs}^2$  resonator GDD). A SHG BBO crystal with a thickness of 2 mm was used, the same measurement routine as in section 6.2.2 was used with fixed OPO and SHG BBO crystal angles and varying central wavelength. The measurement data are presented in Fig. 6.5, where the wavelength is increased towards exact SHG matching wavelength and spectra / oscilloscope traces are measured. The 2000 ns oscilloscope measurement window consists of  $\sim 152$  resonator roundtrips as the pulse period is 13.2 ns. The numbers' panel next to the spectra of Fig. 6.5B indicate the measured characteristics of the pulse – output average power, pulse duration and time-bandwidth product.

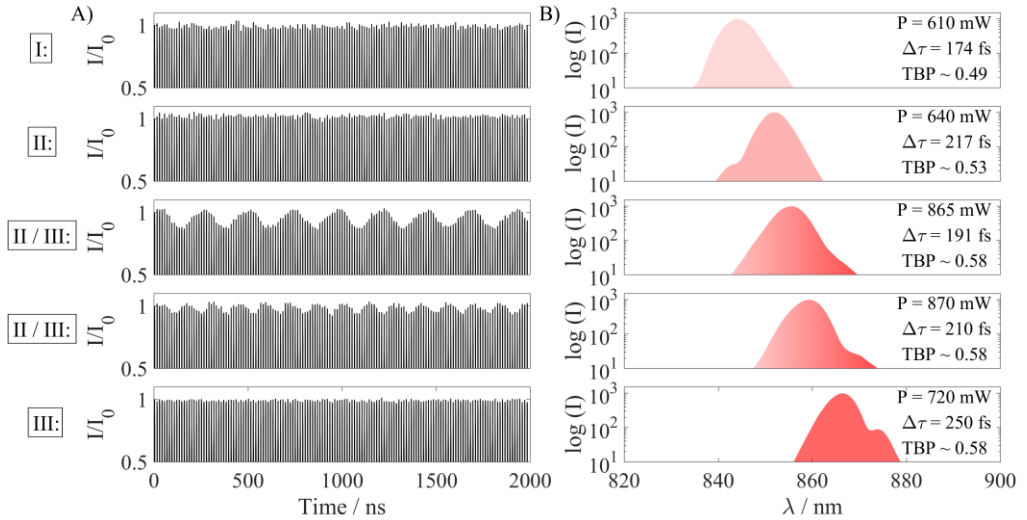


Fig. 6.5. A): oscilloscope traces while signal wavelength is increased top to bottom. B): corresponding experimental spectra while signal wavelength is increased top to bottom. In both panels the traces and spectra correspond to the green designated power and pulse duration measurements of Fig. 6.3C and Fig. 6.3D. The number boxes on the left indicate the soliton order of a pulse with corresponding oscilloscope trace and spectrum. In both panels OPO LBO angle is fixed at  $12.7^\circ$  for optimal conversion efficiency to 860 nm and SHG BBO angle is fixed at  $26.6^\circ$  for optimal conversion efficiency to 881 nm.

The complementary numerical simulations were also carried out, steady state pulse time domain intensity and spectra dependence on the number of resonator round trips are shown in Fig. 6.6. The panels on the right show time domain intensity and spectra averaged through the 200 roundtrips, which should correspond to the experimentally measured spectra and autocorrelation traces. The panels cover zones / soliton orders in which the output power change peculiarities were measured. Zone I (1<sup>st</sup> order soliton) show well behaved Gaussian-like spectrum and pulse train. Transition to zone II (2<sup>nd</sup> order soliton) leads to blue shifted dispersive wave emitted by higher order soliton, an increase of the output power and increase of the pulse duration. The Fig. 6.6 zone II shows blue shifted dispersive wave and stable time domain pulse splitting effect as an indicative feature of soliton fission to individual solitons [47]. An increase of the soliton order allows higher intracavity soliton power as given by equation (2.101). This leads to more efficient energy extraction from the

pump pulse and increases output power / overall conversion. Similar high order soliton generation process supported by cavity is discussed in [91].

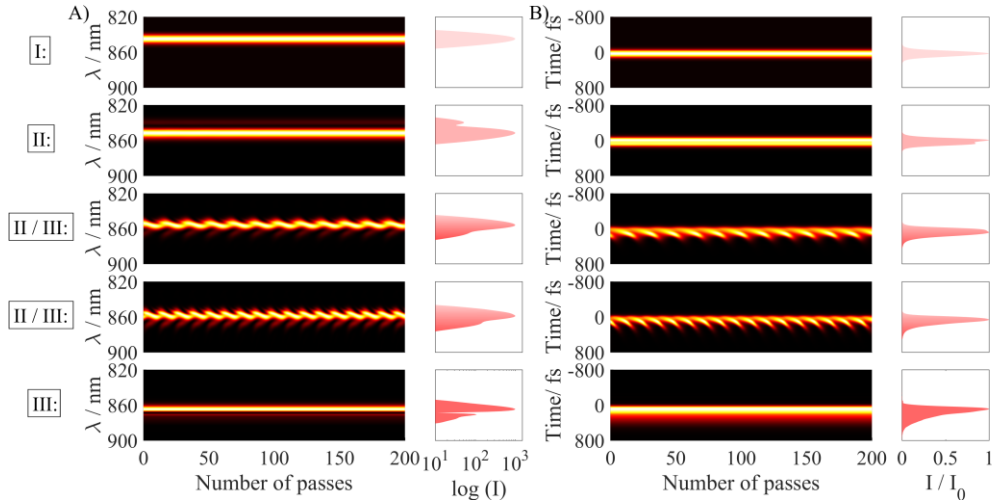


Fig. 6.6. A): simulated steady-state spectra of the OPO at different signal wavelengths (increasing from top to bottom); corresponding average spectrum is shown on the right. B): simulated time domain pulse evolution in a steady state of the OPO while signal wavelength is increased top to bottom with corresponding time domain average intensity to the right. In both panels, the spectra and time domain intensity correspond to the green designated power and pulse duration simulations of Fig. 6.3C and Fig. 6.3D. The number boxes on the left indicate the soliton order of a pulse with corresponding spectrum and time domain intensity evolution. In both panels OPO LBO angle is fixed at  $12.7^\circ$  for optimal conversion efficiency to 860 nm and SHG BBO angle is fixed at  $26.6^\circ$  for optimal conversion efficiency to 881 nm.

The transition between 2<sup>nd</sup> (zone II) and 3<sup>rd</sup> (zone III) order solitons lead to time and spectral domain oscillations as shown measured in Fig. 6.5 and numerically simulated in Fig. 6.6. The period of these oscillations decreases rapidly when the central wavelength is slightly increased by 5 nm and corresponding negative nonlinearity is increased. The measured periods vary from 18 to 11 resonator roundtrips. Higher order solitons have a feature of periodic temporal and spectral shape evolution when they are not perturbed by higher orders of dispersion. The

number of rounds trips after which the pulse shape is restored can be calculated according to the equation [101]:

$$N_{\text{soliton period}} = \frac{\tau^2}{2|GDD|}, \quad (6.2)$$

where  $\tau$  is pulse duration, GDD is the total resonator round trip group delay dispersion. Inserting numbers in to the equation (6.2) we get soliton period value at the transition point of 2<sup>nd</sup> to 3<sup>rd</sup> soliton of 15 periods. Rapid decrease of the oscillation period with the growing output power could be explained by the rapid decrease of resonator GDD when an additional negative nonlinear GDD term is included as shown in Fig. 6.4C. 5 nm wavelength shift of the transition wavelength corresponds to  $\sim -500 \text{ fs}^2$  additional GDD (25% decrease of the total resonator's GDD). Inserting the numbers into equation (6.2) provides a period change from 15 to 11, which is close to the experimentally observed value. Disappearance of the oscillations could mean that the nonlinear phase higher orders are large enough to perturb soliton and break it into constituent low order solitons. The wavelength range at which the oscillations are observed is also consistent with nonlinear GDD oscillations period  $\Delta\lambda \sim 5 \text{ nm}$  as shown in Fig. 6.4C.

The 3<sup>th</sup> order solitons (zone III) show red shifted dispersive waves and increased pulse durations, and the OPO output power is increased. The oscillations are no longer observed – this could be a feature of a soliton fission to individual solitons. As shown in Fig. 6.7, the experimental autocorrelation measurements of zone II show distinct wings, a feature of pulse splitting behavior. Zone III measurements show overall longer pulse durations, presumably as time offsets between individual pulses are too small to differentiate.

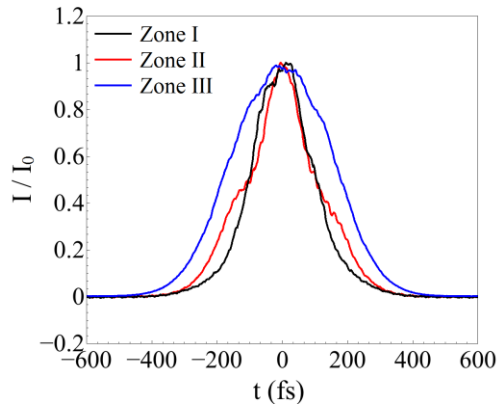


Fig. 6.7. Experimental autocorrelation traces measured in zone I, zone II and zone III with 2 mm BBO and 2000 fs<sup>2</sup> intracavity GDD.

From the practical point of view, the experimental data demonstrates that operating in 2<sup>nd</sup> or 3<sup>rd</sup> soliton regime lead to deteriorated pulse and spectrum characteristics, along with an increased output power of the device. In order to avoid these effects, the cascaded nonlinearity and intracavity intensity should be limited up to 2<sup>nd</sup> order soliton threshold.

### **6.3 Summary**

The soliton formation mechanisms were investigated in high average power femtosecond optical parametric oscillator pumped by the second harmonic of Yb: KGW solid state oscillator. The negative cascaded nonlinearity was used to compensate positive intracavity GDD. Two different SHG crystal lengths were experimentally investigated, with thick crystal leading to the negative nonlinearity large enough to reach the threshold of higher order solitons. The observed soliton related effects include output power increase, pulse splitting under perturbations of higher orders of nonlinear phase, self-phase modulation phase matched dispersive wave generation, time and spectral domain oscillations with soliton period. The numerical modelling was used to confirm the observed experimental results. These results provide deeper understanding of the effects observed in a high power all positive dispersion femtosecond optical parametric oscillator with adjustable negative nonlinearity.

## 7 Spatial domain CQN effects

High intracavity intensities in femtosecond optical parametric oscillators induce not only temporal but also spatial nonlinear effects in the crystals used for amplification. The nonlinear spatial domain effects such as self-focusing and defocusing remain largely unexplored in optical parametric oscillators, but are well analyzed in a number of other single-pass and laser resonator applications. Spatial domain modelling of optical parametric amplifiers shows that the nonlinear spatial domain effects are too weak to have an impact to a single pass OPA system if the peak power is lower than the critical power. If the peak power is larger than the critical power, self-refraction distorts beam quality [102, 103]. Intracavity self-focusing is well analyzed and is a mechanism underlying the ubiquitous Kerr lens mode-locking in laser oscillators. The resonator stability is sensitive to minute changes of the self-focusing lens, so spatial effects are important even at powers well below critical [104, 105]. The self-focusing and defocusing is observed in a single pass quadratic medium pulse compressors, where cascaded effect leads to high values of effective nonlinearity [21, 22, 106]. In addition to that, the classical Z-scan setup was used to directly observe CQN induced spatial domain effects [76, 82].

In this chapter, impact is demonstrated of CQN induced effective focusing / defocusing nonlinear lenses reaching focal lengths of  $f \sim 30 \text{ mm}$  ( $D \sim 33 \text{ m}^{-1}$ ) /  $f \sim -110 \text{ mm}$  ( $D \sim -9 \text{ m}^{-1}$ ). Such large lens dioptric powers inevitably change the stability of resonator. Both operation near the stability range and resonator astigmatism lead to the deterioration of spatial beam properties. Generation of axially asymmetric or pass-to-pass unstable resonator modes were observed. It was shown that operating the crystal with phase mismatch changes the physical operation of resonator from linear to ring-like with two nonlinear crystals having two different focusing powers. Calculations showed that the CQN induced spatial nonlinear phase should lead to severe longitudinal chromatic aberrations for broad spectrum pulses. These findings lead to a better understanding of how to design a high power femtosecond optical parametric oscillator with optimal beam characteristics.

Parts of the material covered in this chapter have been published in publication P7.

## 7.1 Experimental procedures

The optical setup used for the experiments is shown in Fig. 7.1. The optical parametric oscillator is pumped by the second harmonic of Yb: KGW based femtosecond oscillator (Flint, Light Conversion). Pump oscillator emits 12W of average power with 140 fs pulse duration at 1030 nm central wavelength and 76 MHz repetition rate. Pump light is frequency doubled in 2.5 mm length LBO crystal with AR coatings, where 6 W of average power at 515 nm is generated with 50 % conversion efficiency, the pulse duration of the second harmonic is 135 fs. Fundamental light is filtered out, and pump light is delivered to pump the optical parametric oscillator. Pump light is focused to the spot size of 50  $\mu\text{m}$ , which is the size of resonating signal mode's radius. When operating at maximum output power, the calculated signal intensity reaches 20  $\text{GW}/\text{cm}^2$  in LBO crystal. Cavity mirrors M6, M7, M8, M9 are highly reflective in the range from 770 nm to 970 nm. The used mirror design is a simple  $\lambda/4$  stack with a low group velocity dispersion throughout the wavelength range (decreasing from +20  $\text{fs}^2$  at 770 nm to -20  $\text{fs}^2$  at 970 nm). The used concave mirrors ( $R = -200$  mm) focus the resonating beam into the nonlinear crystal. The angle of incidence to spherical mirrors is  $3^\circ$ . This angle determines the astigmatism of the resonator. We will adopt the term 'tangential plane' or 'X plane' further in the paper to denote the plane in which this angle is formed. One of the curved mirrors, M5, is highly reflective in 770 to 970 nm range and has high transmittance at the pump wavelength of 515 nm. The output coupler OC with 10 % of transmission in the wavelength range from 770 to 970 nm was used. Nonlinear 2.5 mm long LBO crystal (crystal =  $14^\circ$ , type I, Eksma Optics) was used as OPO gain material. The crystal was AR coated at 1030+515 nm. It was mounted on precision rotation stage allowing the control of phase matching angle, which was later recalculated to internal angle. The pump beam is polarized in sagittal plane (Y) and the crystal is rotated in this plane for angular phase matching. Since the rotation of the LBO crystal slightly misaligned the resonator cavity, the end mirror M9 was adjusted to realign the resonator to the maximum output power after each angle change. Beam dump discarded the remaining pump and idler beams. OPO cavity length was adjusted by moving the output coupler placed on a translation stage, to enable finding synchronous pumping conditions. Fused silica windows GP1 and GP2 (14 mm thickness, AR coated for 650-1000 nm,  $R < 0.5\%$ ) were inserted into the cavity to ensure positive group delay dispersion. The total calculated group delay dispersion of the cavity was  $\sim 1900 \text{ fs}^2$  at 860 nm. The two curved mirrors M5

and M6 are put on the translation tables to allow changing the stability of the resonator.

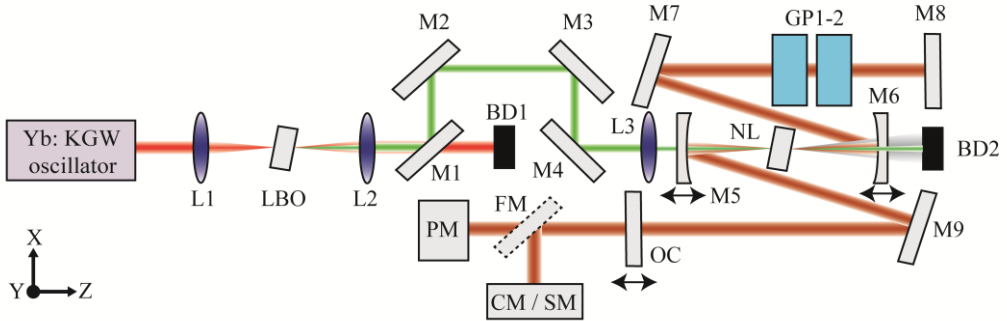


Fig. 7.1. Experimental setup. L1, L2, L3 – lenses for second harmonic generation, collimation and pump light focusing respectively. M1, M2, M3, M4 mirrors for pump light delivery with high transmission at fundamental wavelength. M5, M6 – curved resonator mirrors on a translation table. M7, M8, M9 – plane resonator mirrors. OC – output coupler, NL – nonlinear crystal. BD1, BD2- beam dump. FM – flip mirror, PM – power meter, CM – camera, SM – spectrometer. GP1-2 intracavity Fused Silica glass plates.

Average power of output radiation was measured using a power meter (Nova-2, Ophir) equipped with a thermopile detector (30(150)A-BB-18, Ophir). Radiation spectra were recorded using a spectrometer (STS-NIR, Ocean Optics), pulse durations were measured using a scanning autocorrelator (Geco, Light Conversion), and the beam profile was measured with FLIR Chameleon camera (CMLN-13S2C-CS) at 30 cm distance from the output coupler.

In order to compare the experimental beam measurements done by a camera to the simulated ones for the case of an unstable resonator, the last 20 passes of the simulated beam were averaged when steady output power state was reached. In the case of stable resonator, the mode radii remain the same pass to pass and no averaging was needed.

The nonlinear phase was extracted from the nonlinear part of the system of equations (2.80)-(2.82). During each step of the split step algorithm, this nonlinear part is solved and nonlinear phase shift is extracted independently from linear phase. The nonlinear phase dependence on the spatial coordinate results in a spatial nonlinear phase shift. Fitting this nonlinear phase shift to a parabola allows

approximating the effect of nonlinearity as a nonlinear lens which is accurate for the center of the beam. Both coordinates were fit independently and the extracted lens powers were later used for ABCD matrix resonator stability calculation.

To save the computational cost, the coupled equations are solved in spatial domain only, with time domain effects, such as dispersion and finite pulse width, excluded. This induces calculation error, but the model is accurate enough for the calculation of the spatial domain mode parameters. The ratio between simulated and experimentally measured output powers provides approximate overestimation of the intracavity intensity - around 25 %. The temporal walk-off between the signal (860 nm) and the second harmonic pump (515 nm) pulse in the 2.5 mm LBO crystal is 110 fs. The pump pulse width was 135 fs, the generated signal had a pulse width of 180 fs. If the pulses coincide at the center of the crystal for the most optimal temporal overlap (signal delayed by half the walk-off value of 55 fs at the entrance of the crystal), the walk-off is 30 - 40 % of the signal and pump pulse durations. Therefore, an overestimated

simulated intensity should stem from the overestimated effective gain which should be decreased because of a temporal walk-off. This was not accounted for, because of the semi empirical origin of the effective gain damping term and acceptable correspondence between simulated and experimental results. Moreover, a quasi-CW model that uses the peak gain of the pulsed pump was shown to be quite accurate estimate of the simulated gain of the OPO [107].

The resonator stability was calculated using the ABCD matrix formalism. The stable resonator is obtained when the round-trip matrix terms are in the range of  $-1 < (A + D)/2 < 1$ . The  $(A + D)/2$  parameter is calculated separately for each of the transverse coordinates. The four-mirror folded resonator consists of two stability zones with different mode sizes in the output coupler and in the nonlinear crystal. Throughout the paper, the terminology of zone I and zone II was used, the transition of both zones happens when  $(A + D)/2$  reaches -1. The resonator was operated around this transition point in the experimental setup, as being close to the stability limit makes the resonator more sensitive to the nonlinear focusing / defocusing. Operation near the stability limit of  $(A + D)/2 \sim 1$  makes the resonator just as sensitive to the focusing / defocusing and should produce similar results. On the other hand, experimentally probing both stability zones near this stability limit would be hard to perform, as both zones would be separated by whole stability zone width, as will be further shown in a linear stability map of Fig. 7.2A.

One important observation is that when the OPO is operated at phase mismatch, the nonlinear lenses for forward and backward propagations are different. On a forward pass, nonlinear focusing / defocusing stems from material plus cascaded nonlinearity and on a backward pass only material nonlinearity contributes to the nonlinear focusing. This means that in effect the investigated resonator is not a linear one, but rather acts as a ring resonator with two nonlinear crystals having two different focusing powers, because the resonating beam experiences a different nonlinear lens during its return pass. To account for this, the resonator was analyzed as a ring resonator with ABCD formalism as shown in [67]. A nonlinear lens was included as a simple lens matrix with a known focal length, calculated from the parabolic part of simulated nonlinear phase. A further stability analysis needs to be done while using the ABCD matrix of a self-focusing nonlinear medium as shown in [67], but our approach of using a simple lens matrix was sufficient to allow interpretations of the first experiments.

It is interesting to note, that only with the account of nonlinear focal lengths the stability and mode sizes could be matched to the values observed experimentally. The  $(A_y + D_y)/2$  parameter for a resonator without nonlinear focal length was  $\sim -0.85$ . Insertion of the nonlinear focal lengths with zero phase mismatch ( $f_{NL} \sim 55$  mm for zone II) shifted the resonator close to the stability limit with a  $(A_y + D_y)/2$  value of  $\sim -0.98$ . The calculated nonlinear focal length depends on the mode size as seen from equation (2.106). The mode sizes in a crystal were  $62 \mu\text{m}$  (zone I) and  $50 \mu\text{m}$  (zone II). A return pass nonlinear focal length with zero phase mismatch  $\Delta\theta \sim 0^\circ$  was calculated to be 125 mm in zone I and 55 mm in zone II. A forward pass parabolic fit of the cascaded nonlinear phase depends on the crystal detuning. It was calculated to be: zone I focal lengths ranged from +125 mm ( $\Delta\theta \sim -0.25^\circ$ ) to infinity ( $\Delta\theta \sim 0.4^\circ$ ) and back to -250 mm ( $\Delta\theta \sim 0.65^\circ$ ). Zone II focal lengths ranged from +30 mm ( $\Delta\theta \sim -0.5^\circ$ ) to infinity ( $\Delta\theta \sim 0.25^\circ$ ) and back to -110 mm ( $\Delta\theta \sim 0.9^\circ$ ). As the nonlinear lenses were inserted in an approximate geometrical focus of the linear resonator, the effect of the lenses was not as evident, but nevertheless experimentally observable. A major difference in forward and backward propagation nonlinear focal lengths clearly indicates that ring resonator formalism is more suitable for a phase mismatched optical parametric oscillator description, even though experimentally it is assembled as a linear one.

The parabolic fit of the focal length of this nonlinear lens can also be calculated using the equation (2.106). Direct calculation of equation (2.106) while inserting zone radii  $62 \mu\text{m}$  (zone I) and  $50 \mu\text{m}$  (zone II), internal peak powers at the

peak of the tuning curve  $\sim 630$  kW and nonlinear refractive index of  $n_2 \sim 2 \times 10^{-20}$  m<sup>2</sup>/W results in nonlinear focal lengths of  $f_{NL}=98$  mm (zone I) and  $f_{NL}=42$  mm (zone II), which are close to numerically simulated values for a returning pass with material's contribution only.

## 7.2 Results and discussion

In order to analyze the nonlinear focal length's impact to resonator's mode formation, the stability of phase-matched operation was investigated. The signal wavelength was fixed at 860 nm and the OPO crystal angle was fixed at  $\theta \sim 12.6^\circ$ . The phase mismatch was minimized for maximum output power and low cascaded nonlinearity influence to the resonator stability. The distance between resonator's curved mirrors was changed (both of the mirrors were translated simultaneously by  $\Delta L$ ) and resonator output mode was measured with a camera. The results are shown in Fig. 7.2. Fig. 7.2A shows the measured and numerically simulated second-moment radii ( $2\sigma$ ) in both tangential (X) and sagittal planes (Y). Fig. 7.2B shows measured and Fig. 7.2C shows numerically simulated beam profiles. The discrepancy between the measured and numerically simulated beam profiles (especially at the distance of  $\Delta L = +0.2$  mm) could be explained by an error of estimating the exact angles of incidence on the curved mirrors. This could lead to more astigmatic cavity in the experiment which would lead to higher ellipticity of the output beam. When the mirrors are translated, the resonator stability approaches a stability limit at  $(A+D)/2 = -1$ . The non-zero angle of incidence of the resonator curved mirrors lead to different stability diagrams for both planes, shown in Fig. 7.2A. As described in the experimental procedures section, the nonlinear focal lengths arising from cubic nonlinearity were included in ABCD matrix calculation and the  $(A+D)/2$  parameter was calculated. The -1 value of the stability parameter is approached in different  $\Delta L$  detuning values for both of the tangential (X) and sagittal (Y) planes. That leads to strong changes in the ellipticity of the beam as the distance  $\Delta L$  and stability is changed. The red colored zones show the regions of experimentally observed highly elliptical X and Y beams, named correspondingly zone I and zone II.

It is interesting to note, that the insertion of the nonlinear lenses shifts the calculated stability below values of -1 to a range where resonator is unstable. The calculated mode sizes in a crystal are  $62 \mu\text{m}$  (zone I) and  $50 \mu\text{m}$  (zone II) and these lead to largely different nonlinear focal lengths because of the 4<sup>th</sup> power dependence as shown in equation (2.106). The calculated nonlinear focal lengths are much smaller in zone II ( $f_{\text{NL}} = 125$  mm in zone I and 55 mm in zone II), so the stability is stronger shifted below -1 in zone II than zone I. This leads to a larger sagittal plane (Y) beam ellipticity in zone II.

### Spatial domain CQN effects

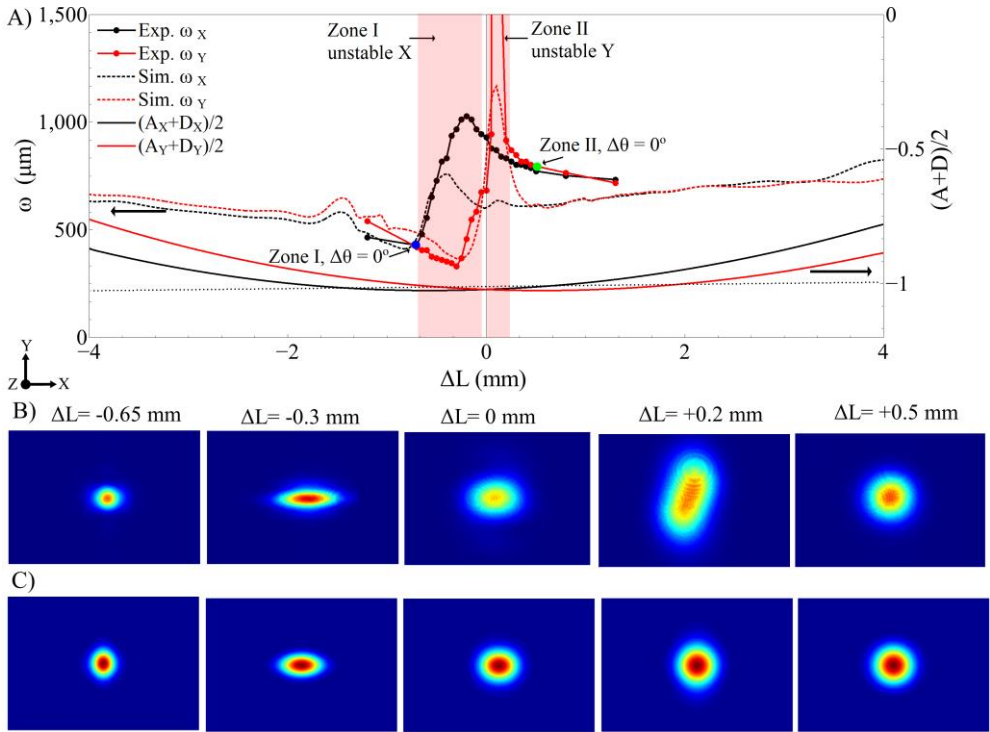


Fig. 7.2. A) The experimentally measured and numerically simulated second-moment radii ( $2\sigma$ ) dependence on the distance between curved resonator mirrors and resonator stability parameter  $(A+D)/2$ . The radii and stability are calculated separately for tangential (X) and sagittal (Y) planes. Blue and green points indicate the distances  $\Delta L$  where the resonator was aligned for the zone I and zone II cascaded nonlinearity experiments. B) Experimentally measured beam profiles corresponding to different values of  $\Delta L$ . C) Numerically simulated output beam profiles corresponding to different values of  $\Delta L$ . In all panels signal central wavelength is fixed at 860 nm and the crystal angle is fixed at  $\Delta\theta=12.6^\circ$ .

In order to probe the influence of cascaded nonlinearity to the mode formation, the mirror distance was fixed at two stable resonator points:  $\Delta L=-0.8$  mm (close to unstable zone I) and  $\Delta L=0.6$  mm (close to unstable zone II). The points are indicated in Fig. 7.2A as blue and green dots. This allowed working with a stable resonator but being close enough to the edge of the stability zone to probe the nonlinear focusing / defocusing effects. As the nonlinear crystal was rotated, the resonator was realigned to maximum output power by the end mirror and resonator length was

adjusted to resonate the wavelength of 860 nm. The measured output power dependence on crystal rotation angle is given in Fig. 7.3 for both zone I and zone II. The measured pulse duration at the peak of the tuning curve is 180 fs, the pulse is chirped with a pulse quality of  $\Delta\nu\Delta\tau \sim 0.85$ . The mode radius at the crystal is smaller in zone II, making the effect of pump beam walk-off more evident. The walk-off decreases the effective crystal length, which, in turn, increases the acceptance angle of the crystal. This leads to increase in the width of the power tuning curve. On the other hand, shorter effective crystal length leads to the decrease of the output power as is evident from the Fig. 7.3. The positive angle offsets of zone II starting at  $\Delta\theta \sim 0.5^\circ$  lead to an asymmetry of the otherwise symmetric tuning curve. Further investigation will reveal that this angle range leads to unstable resonator. Surprisingly, the interaction of the unstable signal beam with the pump is sufficient to support the generation and even be at higher power levels than those resulting from the stable signal beam, at the same crystal detuning.

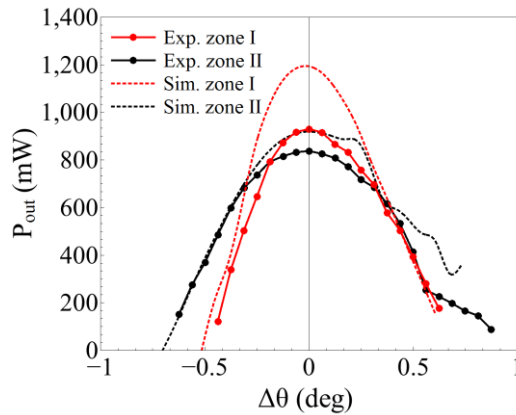


Fig. 7.3. The experimentally measured and numerically simulated output power dependence on the nonlinear crystal detuning when the resonator was aligned for the zone I and zone II cascaded nonlinearity experiments. Signal central wavelength is fixed at 860 nm.

Since the largest effects of the cascaded quadratic nonlinearities on the output beam of the OPO occur around the edges of the resonator stability range, we investigated the beam properties as a function of angular detuning of the OPO crystal near the instability zones I and II.

*Unstable zone I.* First, the dependence of the output beam profiles on the phase matching angle was measured when the resonator was fixed at  $\Delta L = -0.8$  mm curved mirror distance (close to unstable zone I). The resulting dependencies for sagittal and tangential beam radii are shown in Fig. 7.4A. The blue points correspond to the measured beam profile (Fig. 7.4B), simulated beam profile (Fig. 7.4C) and measured spectra (Fig. 7.4D) at these exact angle offsets. The radii change indicate that the negative crystal offsets lead to positive / focusing cascaded nonlinearity which shifts the stability towards configuration supporting highly elliptical mode in tangential (X) direction. The red area indicates the unstable angle offset region when resonator is pushed towards the unstable part of zone I shown in Fig. 7.2A. The trends of change in the simulated beam profiles closely resemble the experimental ones, albeit the simulated second-moment radii show higher deviation from the experiment. The reason for the discrepancy may be related to the contribution of dot-like vertical mode structure at large negative crystal offsets. The measured spectra in Fig. 7.4D indicate the contribution of SPM to spectral broadening. As the crystal is offset to negative angles, positive cascaded nonlinearity adds up to the material nonlinearity and together with positive cavity group delay dispersion leads to the broadening of the output spectrum. On the other hand, as the crystal is offset to positive angles, the negative cascaded nonlinearity compensates the material nonlinearity and together with positive cavity group delay dispersion lead to the Gaussian output spectrum and soliton-like pulse. This effect is investigated in the chapters 5 and 6 of this dissertation.

### Spatial domain CQN effects

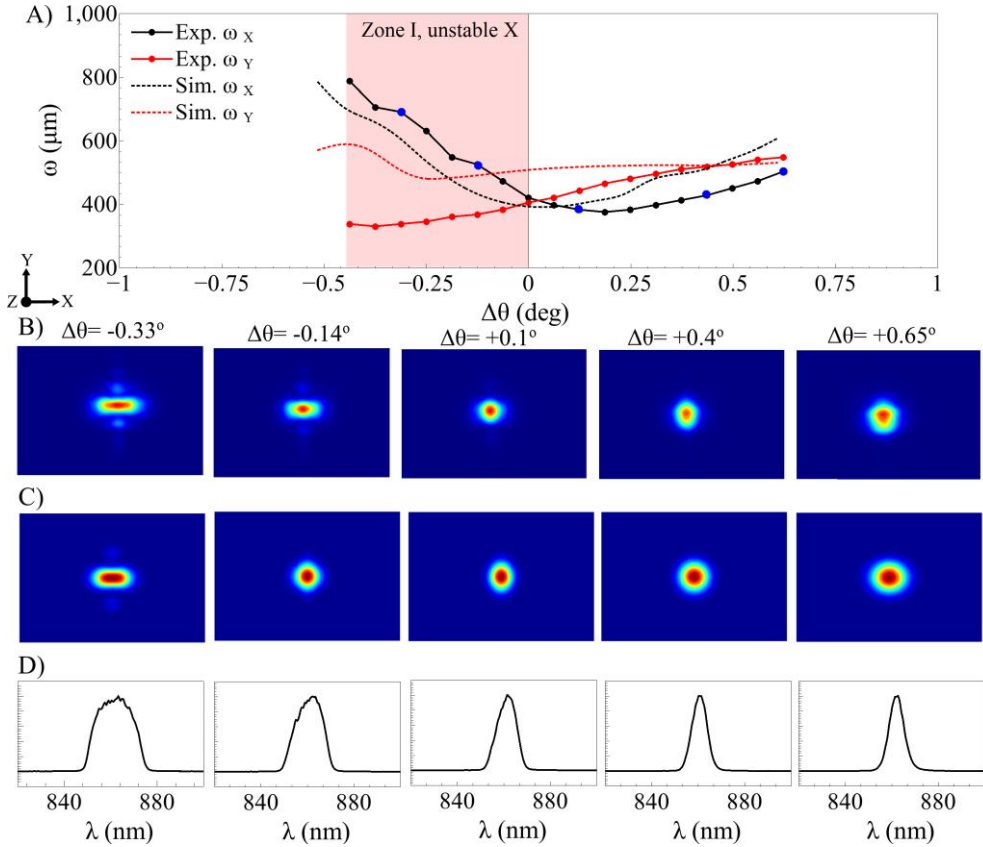


Fig. 7.4. A) The experimentally measured and numerically simulated second-moment radii ( $2\sigma$ ) dependence on the nonlinear crystal angle detuning when resonator is aligned in zone I. The radii are calculated separately for tangential (X) and sagittal (Y) planes. Blue points indicate the crystal angles where experimental, numerically simulated beam profiles and output spectra are shown below. B) Experimentally measured beam profiles corresponding to different values of  $\Delta\theta$ . C) Numerically simulated output beam profiles corresponding to different values of  $\Delta\theta$ . D) Experimentally measured pulse spectra corresponding to different values of  $\Delta\theta$ . The central wavelength is fixed at 860 nm. The red color area indicates the experimentally observed unstable or highly asymmetric tangential (X) plane region in zone I.

*Unstable zone II.* Since the investigated resonator has two instability zones, we also measured the output beam dependence on the phase matching angle with the curved mirror distance fixed at  $\Delta L = -0.6$  mm (close to unstable zone II). The measured sagittal and tangential beam radii are shown in Fig. 7.5A at different values of the phase matching angle. The green points correspond to the measured beam profile (Fig. 7.5B), simulated beam profile (Fig. 7.5C) and measured spectra (Fig. 7.5D) at these exact angle offsets. The observed change in the radii indicates that the positive crystal offsets leads to negative (defocusing) cascaded nonlinearity which shifts the stability towards configuration supporting highly elliptical mode in sagittal (Y) direction. The red area indicates the unstable angle offset region, when the resonator is pushed towards the unstable part of zone II shown in Fig. 7.2A. The simulated beam profiles closely resemble the experimental ones even though the entire numerically simulated region is shifted to smaller crystal offset angles. This can be explained by noting that the simulated output power is higher than experimentally measured, and therefore the impact of simulated cascaded nonlinearity is stronger. The positive crystal offsets lead to highly elliptic beams and TEM<sub>01</sub> like structures. This can be explained by the smaller beam radius at the crystal in zone II compared to zone I: tighter beam produces higher intensity and the defocusing nonlinearity turns into stronger nonlinear lens. Further investigation of the TEM<sub>01</sub>-like structure shows that this is not a stable mode, but an unstable beam which replicates itself every second pass as shown in Fig. 7.6. This clearly indicates that the nonlinear lens is strong enough to push the resonator out of the stability. Essentially each of the sub-beams in the double beam pattern runs at half of fundamental repetition rate with a constant one period offset. The measured spectra in Fig. 7.5D indicate even stronger SPM contribution to spectral broadening when compared to zone I, as the nonlinearity is higher.

### Spatial domain CQN effects

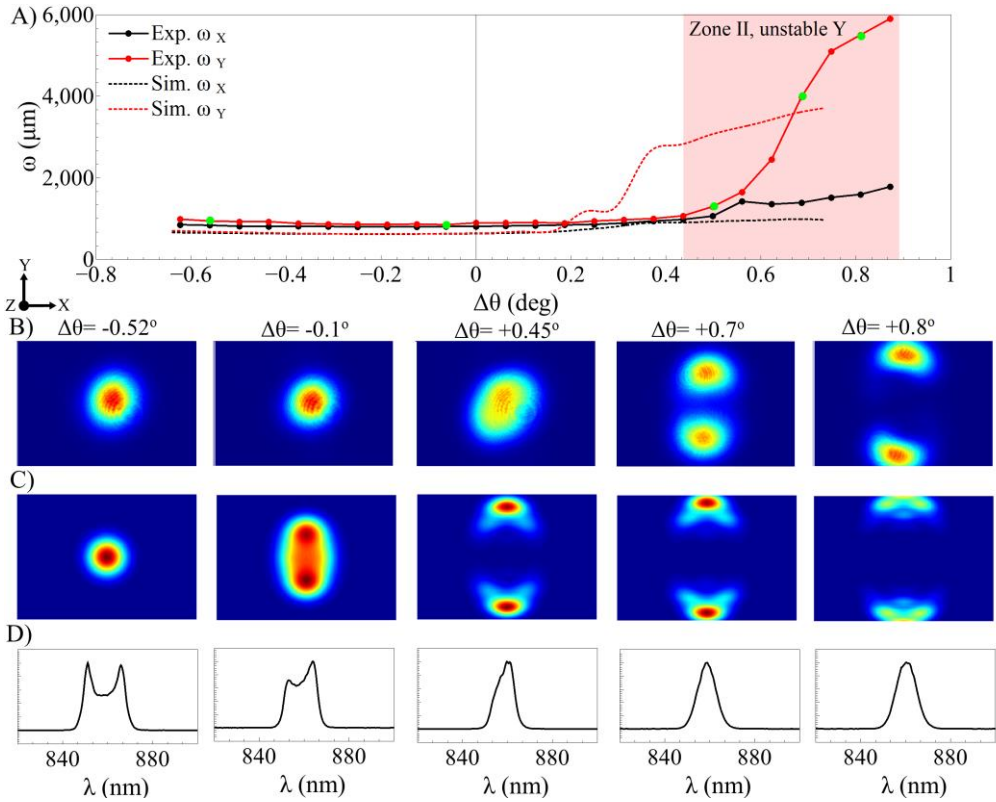


Fig. 7.5. A) The experimentally measured and numerically simulated second-moment radii ( $2\sigma$ ) dependence on the nonlinear crystal angle detuning when resonator is aligned in zone II. The radii are calculated separately for tangential (X) and sagittal (Y) planes. Green points indicate the crystal angles where experimental, numerically simulated beam profiles and output spectra are shown below. B) Experimentally measured beam profiles corresponding to different values of  $\Delta\theta$ . C) Numerically simulated output beam profiles corresponding to different values of  $\Delta\theta$ . D) Experimentally measured pulse spectra corresponding to different values of  $\Delta\theta$ . In all panels signal central wavelength is fixed at 860 nm. The red color area indicates the experimentally observed unstable or highly asymmetric sagittal (Y) plane region in zone II.

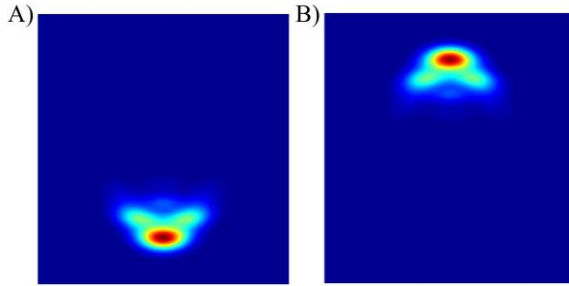


Fig. 7.6. A) The numerically simulated steady state  $N_{th}$  pass output beam profile when resonator is operated in zone II. B) The numerically simulated steady state  $N_{th+1}$  pass output beam profile when resonator is operated in zone II. For both panels the crystal detuning angle is  $\Delta\theta=+0.45^\circ$  and the signal central wavelength is fixed at 860 nm. Steady state defines pass to pass stable output power.

To quantify the nonlinear focusing / defocusing induced by CQN, further simulations were carried out. The nonlinear phase was extracted from numerical model (equations (2.80) - (2.82)). A single pass through the OPO crystal with varying crystal angles was simulated with experimentally observed steady state OPO parameters at the center of the tuning curve: fixed pulse duration  $\tau = 180$  fs, fixed intracavity average power  $P = 8$  W, signal wavelength of 860 nm. The on-axis nonlinear phase was fit with a parabola and from the curvature the nonlinear focal length was calculated. The results are shown in Fig. 7.7A with separate calculation for zone I and zone II. The blue and green calculation points are of the nonlinear focal length values which correspond to the experimentally and numerically simulated beam profiles / spectra shown in the previous figures. The zero of nonlinear phase corresponds to an infinite radius of the curvature of the nonlinear lens, implying that positive material nonlinearity is compensated by negative cascaded nonlinearity.

Fig. 7.7B and Fig. 7.7C shows ABCD matrix stability parameter dependence on nonlinear focal length for both zone I and zone II. The nonlinear lens value from Fig. 7.7A is used as ABCD matrix lens seen by forward propagating beam when optical parametric amplification takes place. The backward propagating beam sees only a fixed positive lens induced by the material nonlinearity. The blue and green points with arrows indicate the shift of nonlinear focal length and corresponding stability while crystal is detuned from negative to positive angles. Blue zone I points are

plotted for the unstable X tangential plane and green zone II points are plotted for the unstable Y sagittal plane. The red areas indicate the unstable region when resonator is pushed towards the unstable zone I or zone II as shown in a linear stability plot of Fig. 7.2A. The stability maps explain the experimental results – in zone I, the initial negative crystal offsets ( $\Delta\theta \sim -0.25^\circ$ ) and mildly focusing cascaded nonlinearity ( $f_{NL} = +125$  mm) lead to unstable resonator at tangential X plane. When the crystal is positively offset ( $\Delta\theta \sim 0.4^\circ$ ), nonlinear focal length becomes infinite and with further crystal angle increase ( $\Delta\theta \sim 0.65^\circ$ ) the resonator is stabilized with weakly defocusing cascaded nonlinearity ( $f_{NL} = -250$  mm). In zone II, the initial negative crystal offsets ( $\Delta\theta \sim -0.5^\circ$ ) and strongly focusing cascaded nonlinearity ( $f_{NL} = +30$  mm) lead to stable resonator at sagittal Y plane. When the crystal is positively offset ( $\Delta\theta \sim 0.25^\circ$ ), nonlinear focal length becomes infinite and with further increase in crystal angle ( $\Delta\theta \sim 0.9^\circ$ ) the resonator becomes unstable with mildly defocusing cascaded nonlinearity ( $f_{NL} = -110$  mm).

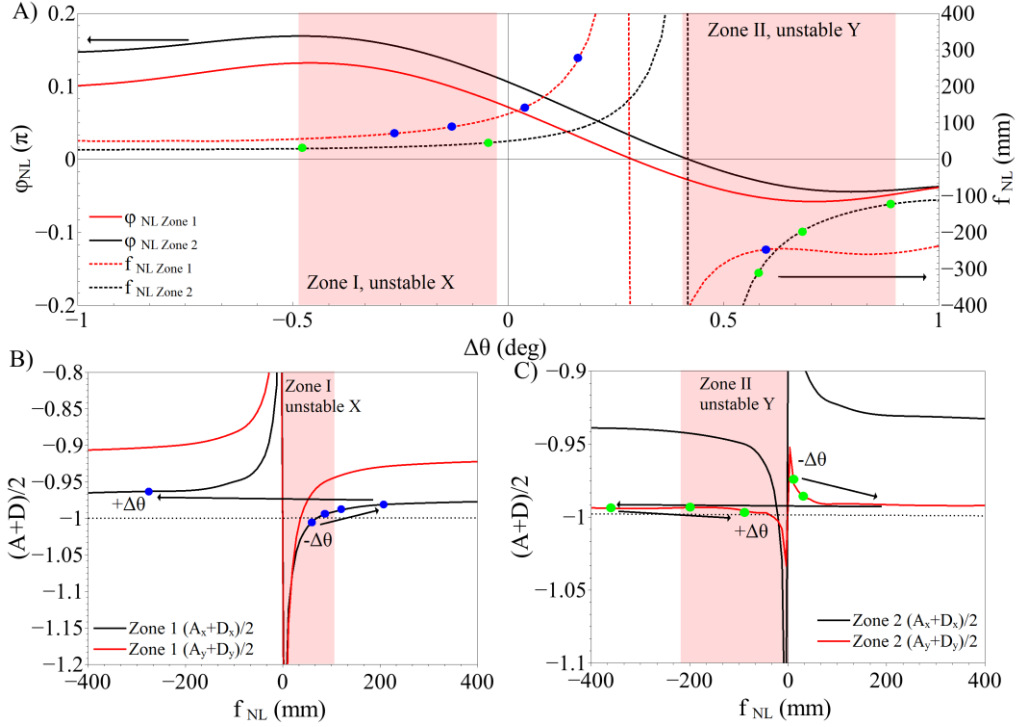


Fig. 7.7. A) The calculated peak nonlinear phase and nonlinear focal length dependence on the nonlinear crystal angle detuning when resonator is aligned in zone I and zone II. B) The calculated tangential (X) and sagittal (Y) resonator stability parameter  $(A+D)/2$  dependence on nonlinear lens focal length when resonator is aligned in zone I. C) The calculated tangential (X) and sagittal (Y) resonator stability parameter  $(A+D)/2$  dependence on nonlinear lens focal length when resonator is aligned in zone II. In all panels signal central wavelength is fixed at 860 nm, the red color areas indicate the experimentally observed unstable or highly asymmetric regions in zone I and zone II. In all panels blue and green points indicate the experimental and simulated beam profiles, spectra measurements shown in Fig. 7.4 and Fig. 7.5.

The tests were also performed to see if the asymmetry of the beam is not induced by resonator misalignment due to the rotation of the crystal. To test this, the central wavelength was tuned away from the exact phase matching by changing the cavity length (i.e. synchronous pumping condition) at fixed crystal angle. This way, the equivalent phase mismatch could be induced as by rotating the crystal, but in this

case the resonator geometry is left intact [76]. In zone I, the wavelength was tuned to 820 nm, in zone II to 900 nm with the crystal angle optimized for 860 nm. The same asymmetric beam patterns were generated, indicating that the process is purely due to focusing / defocusing by cascaded nonlinearity.

Furthermore, it is instructive to quantify the CQN induced nonlinear lens wavelength dependency. Based on the simulations presented in the chapter 6, the nonlinear phase dependence on wavelength was extracted for the LBO adjusted for optimal conversion efficiency at 860 nm. Relative to 860 nm, there is a  $-0.05 \pi$  nonlinear phase shift at 820 nm and a  $0.1 \pi$  nonlinear phase shift at 900 nm. The phase relationship is quasi linear in wavelength range of 820 nm to 900 nm. Therefore, in the spatial domain 820 nm is self-defocused, while 900 nm is self-focused and this acts as a longitudinal chromatic aberration. These phase mismatched wavelengths of 820 nm and 900 nm correspond to the equivalent phase mismatch induced to 860 nm by the angle offsets  $\Delta\theta \sim -0.5^\circ$  and  $\Delta\theta \sim 0.9^\circ$  shown in the Fig. 7.7A. The same nonlinear focal lengths could be attributed to the phase mismatched wavelengths:  $\lambda = 820$  nm would focus with  $f \sim 30$  mm ( $D \sim 33 \text{ m}^{-1}$  at  $\Delta\theta \sim -0.5^\circ$ ) and  $\lambda = 900$  nm would focus with  $f \sim -110$  mm ( $D \sim -9 \text{ m}^{-1}$  at  $\Delta\theta \sim 0.9^\circ$ ). Therefore, the chromatic aberration would be extremely strong for a spectrum bandwidth of  $\Delta\lambda = 80$  nm (14 fs pulse duration pulses), this bandwidth is supported by an amplification bandwidth of a crystal if resonator's group delay dispersion is minimized. Therefore, the CQN induced spatial domain longitudinal chromatic aberration should be an effect limiting the beam quality of generated short pulses not only in femtosecond OPO, but also in optical parametric amplifiers operating with a phase mismatch. On the other hand, the pulse bandwidth generated in our setup was much narrower with  $\Delta\lambda = 6$  nm. The nonlinear phase difference between the side wavelength components is  $\Delta\phi = 0.015 \pi$ , leading to the nonlinear focal lengths of  $f \sim 39$  mm ( $D \sim 25.5 \text{ m}^{-1}$ ) at 857 nm and  $f \sim 35$  mm ( $D \sim 28.5 \text{ m}^{-1}$ ) at 863 nm. There is  $3 \text{ m}^{-1}$  diopters focusing difference across the spectrum bandwidth, which is collimated by the spherical mirrors, so the effect is not evident at the output, nevertheless, it could be pronounced for a broader spectrum. These considerations also hint that full spatial and time domain simulation of the phase mismatched optical parametric oscillators or amplifiers should show the interplay between aforementioned effects, which could lead to such a peculiar effect as simultaneous generation of stable and unstable resonator modes having different wavelengths. Further study is needed to confirm this hypothesis.

It is important to show that the observed effects are not influenced by critical self-focusing. With the measured pulse duration of the OPO  $\tau = 180$  fs, the calculated

peak power is 400 kW at  $\Delta\theta \sim -0.5^\circ$ . Calculation of the maximum nonlinear refractive index from the nonlinear phase at the  $\Delta\theta \sim -0.5^\circ$  leads to  $n_2 \sim 10 \times 10^{-20}$  m<sup>2</sup>/W. The calculated critical power  $P_{crit} = 0.148 \lambda^2 / n n_2$  results in  $\sim 700$  kW [47]. The critical power is defined as the peak power at which the diffraction is balanced by self-focusing. Therefore, our experimental conditions are below the critical self-focusing and the observed mode formation patterns should be influenced only by the cascaded nonlinearity induced stability change and not by mode self-diffraction or filament formation.

Generally, the nonlinear distortions of the spatial laser mode are regarded as harmful and avoided in the design of laser process. However, the success of the now ubiquitous Kerr lens modelocking shows that they could also be applied productively. If the double beam pattern observed in zone II Fig. 7.5 could be made controllable and stable enough, it could lead to some interesting applications. For instance, in Stimulated Raman Microscopy using only one beam which has repetition rate  $f/2$  as a tunable wavelength laser source together with part of fundamental oscillator output with repetition rate  $f$ . The tunable beam could be demodulated with lock-in amplifier at  $f/2$  without an additional fast modulator at  $f/2$ . Another application would be having one of these beams polarization rotated by  $90^\circ$  and recombining them extracavity. This would lead to a tunable wavelength source where every second pulse is with orthogonal polarization. Such a laser source could be used for polarization sensitive nonlinear imaging techniques where difference between the signals from each of the pulse in a pair could be used for background subtraction. Naturally, to enable such applications, nonlinear spatial phenomena occurring in OPO cavities would have to be investigated in much greater detail, finding the ways of their stable generation, control and investigating their applications.

To conclude, design guidelines for high power femtosecond oscillators should be drawn. For example, let us consider the same Z-fold OPO resonator as investigated in this paper. With low pump power and negligible nonlinear lens, resonator could be aligned at the middle of one of the stability zones with the tangential stability of  $(A+D)/2 = -0.5$ . As shown in section 7.1, direct insertion of the experimental parameters to the equation (2.106) leads to the nonlinear focusing power of  $D \sim 24$  m<sup>-1</sup> under the exact phase matching and this value slightly changes the stability of the resonator. The extreme nonlinear lens focusing power of  $D \sim 120$  m<sup>-1</sup> would drive the tangential stability to a value of  $(A+D)/2 = -1$ , leading to an unstable resonator. Simple scaling calculation of equation (2.106) shows that this extreme nonlinear

lens power value could be reached by 5-fold larger intracavity signal power ( $\sim 4$  W of the output signal power) or effective nonlinearity ( $n_2 \sim 15 \times 10^{-20} \text{ m}^2/\text{W}$ ), or 1.5-fold smaller waist size ( $\sim 33 \text{ }\mu\text{m}$  waist size at the crystal) or a combination of all these parameters. The critical self-focusing would as well impact the resonator mode properties and a further study is needed to investigate and decouple the influence of both the linear stability shift and critical self-focusing with increasing intensity or nonlinearity. Therefore, in order to scale the output power and prevent the aforementioned effects, the OPO should be operated with negligible phase mismatch and correspondingly larger mode size at the nonlinear crystal.

### 7.3 Summary

It was shown that the cascaded nonlinearity induced self-focusing and defocusing are strong enough to change resonator's stability. The mode properties are impacted if operating near the resonator's stability edge. With tuning of a phase mismatch, the calculated parabolic part of the cascaded nonlinearity lens focal length changes from  $f \sim 30$  mm ( $D \sim 33$  m<sup>-1</sup>) to infinity and back to  $f \sim -110$  mm ( $D \sim -9$  m<sup>-1</sup>). Such high lens dioptric powers, operation near stability range and resonator astigmatism promoted generation of axially asymmetric or pass-to-pass unstable resonator modes. It was shown that phase mismatched optical parametric oscillation changes the physical operation of resonator from linear to ring-like with two nonlinear crystals having two different focusing powers. A numerical simulation in XYZ spatial domain and a calculation with ABCD matrix approach confirmed the experimental results and allowed interpreting the investigated peculiarities. Calculations showed that the CQN induced spatial nonlinear phase should lead to severe longitudinal chromatic aberrations for broad spectrum pulses. Operating the cascaded nonlinearity crystal intra-cavity near the stability limit allowed probing weak nonlinear effects which would be hard to investigate in a single pass extra-cavity setup.

## **8 Applications of the assembled OPO**

Synchronously pumped femtosecond optical parametric oscillators are invaluable in several scientific applications because of the unique combination of these technical attributes: variable central wavelength, high repetition rate, short pulse duration, relatively high output power and good beam quality. Based on the previously discussed scientific findings, several transportable setups were assembled and delivered to various labs to be tried out in different application areas.

In this chapter, the applications of the assembled OPO prototype are presented in fields of nonlinear microscopy, 2-photon polymerization and 2-photon optogenetics all performed in the field leading laboratories in Lithuania, Germany and United Kingdom.

Parts of the material covered in this chapter have been presented in conference papers CO1 and CO2.

## 8.1 Nonlinear microscopy

Two-photon excitation of molecules is a nonlinear process involving the absorption of two photons whose combined energy is sufficient to induce a molecular transition to an excited electronic state. Excitation occurs when the absorbed photon energy matches the energy gap between the ground and excited state. The same transition can be excited by a two-photon process where the two less energetic photons are simultaneously absorbed. Quantum mechanically, the first photon excites the molecule to a virtual intermediate state and the molecule is eventually brought to the final excited state by the absorption of a second photon.

One of the most important attributes of two-photon microscopy is its inherent 3D sectioning capability. The sectioning capability of this method originates from the quadratic and higher-order dependence of the fluorescence signal upon the excitation intensity distribution [108].

Two-photon absorption efficiency can be measured by  $n_a$ , the number of photons absorbed per fluorophore per pulse [109]:

$$n_a \sim \frac{\sigma I^2 \tau f}{f} = \frac{\sigma P_{ave}^2 NA^4}{f^2 \tau \pi^2 \lambda^4}, \quad (8.1)$$

where  $P_{ave}$  is average pulse train power,  $NA$  is objective numerical aperture,  $f$  is the repetition rate,  $\sigma$  is two-photon absorption cross section,  $\tau$  is the pulse duration and  $\lambda$  is the wavelength.

The design of a multiphoton imaging experiment requires not only high-sensitivity optical instrumentation but also specific and efficient fluorophores. Most fluorophores can be excited in two-photon mode at approximately twice their one-photon absorption wavelength to maximize the two photon absorption coefficient, as shown in chapter 2.1.2.

In this chapter, the nonlinear imaging experiments are presented, which were carried out in University of Oxford, Oxford, United Kingdom, prof. Martin Booth nonlinear imaging laboratory. The prototype of the portable optical parametric oscillator system was assembled at Light Conversion and transported to the destination lab to carry out the experiments.

### 8.1.1 Experimental procedures

The prototype of the optical parametric oscillator (Light Conversion) was based on a cavity including prism-pair dispersion compensator. The pump oscillator had 4 W of output power with 2 W of the second harmonic. The mirrors were highly reflective in the range of 750-1250 nm, output coupler had a reflection of 10% through the tuning range. The output power tuning curve is given in Fig. 8.1. The pulse duration varied between 100 and 160 fs through the tuning range, the central wavelength was changed by rotating the nonlinear crystal. The laser source was tested out in two-photon microscopy and harmonic generation applications.

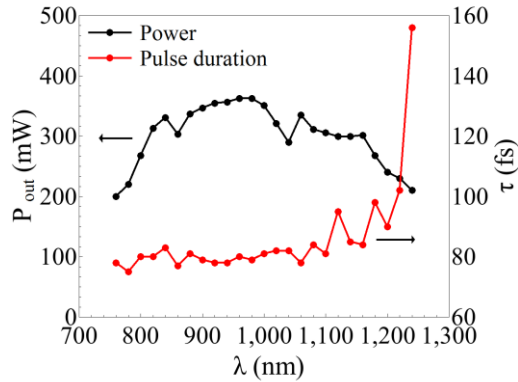


Fig. 8.1. Signal output power and pulse duration dependence on the signal wavelength.

The multi-photon and harmonic generation microscopy experiment was carried out using the experimental scheme shown in Fig. 8.2. The laser source was integrated to already assembled multiphoton microscope, beam width was adapted to overfill the microscope objective aperture.

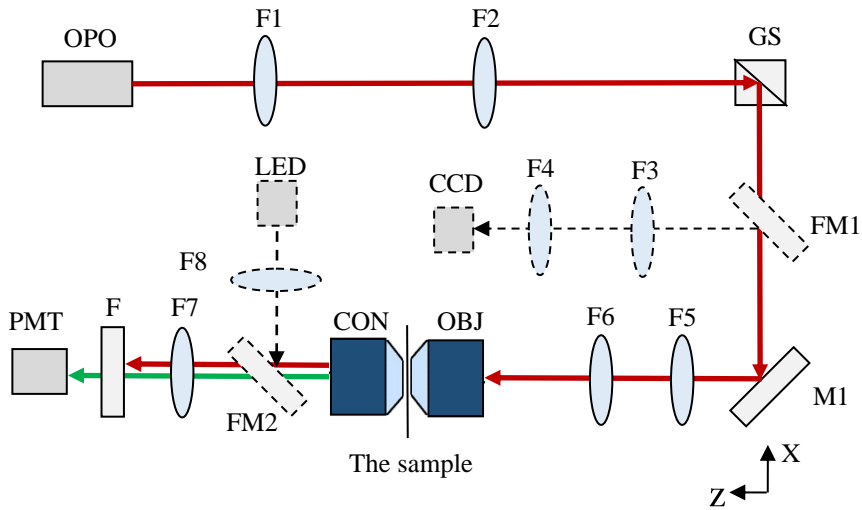


Fig. 8.2. Microscope setup used for two-photon and harmonic generation experiments. OPO – femtosecond optical parametric oscillator; F1, F2 – x3.75 beam expander telescope; GS – “Thorlabs” galvo-scanner; FM1, FM2 – flip mirrors for LED illumination and sample inspection; F8 – Köhler illumination lens; F3, F4 – x0.6 sample imaging telescope; M1 – NIR HR mirror; F5, F6 – x2 beam expander telescope; OBJ – Olympus UApo/340 objective, water immersion, x40, NA=1,15, WD 200  $\mu\text{m}$ ; CON – condenser objective, oil immersion, NA=1,4; F7 – fluorescence focusing lens; F – shortpass “Semrock” “Brightline” filter; PMT – Hamamatsu H7422 photomultiplier.

The scanning is done with galvo-scanners, the sample is also translatable in XYZ space with micrometer translation stage, Z axis positioning is also done with piezo drive translation stage. The field of view is 500 x 500  $\mu\text{m}$ , scanner resolution is 4096 x 4096 pixels, pixel dwell time per pixel could be varied from 2 to 2000  $\mu\text{s}$ . The used filters after the condenser are low-pass, transmitting the visible range and blocking the infrared range. The detection is done with visible range sensitive photomultiplier. In order to align the microscope, the sample is imaged in wide field mode with dashed lines shown in the experimental scheme. LED illumination is used to create a Köhler illumination in the sample plane, the sample is imaged to the CCD camera.

To quantify a quality of the used laser source (with a presumption that microscope objective does not induce additional aberrations), the point spread function is measured. The nano bead 100 nm size sample is used, the nano beads are

imaged with a central wavelength of  $\lambda=1060$  nm. The point spread function is shown in Fig. 8.3, where  $x$  is transversal coordinate and  $z$  is the axial one. The width of the gaussian fit of the measured PSF is  $0.7 \mu\text{m}$  in  $X$  plane and  $2 \mu\text{m}$  in  $Z$  plane, which are close to optimal values for the given  $NA$  of 1.15.

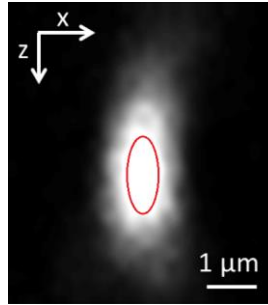


Fig. 8.3. The point spread function measurement of the used nonlinear microscope.  $X$  – transversal sample plane coordinate,  $Z$  – axial sample plane coordinate. Ellipse indicates the gaussian fit FWHM of  $X$  and  $Z$  as minor and major ellipse axis. Image saturation at 0.5 maximum signal level aids to visualize PSF distribution and signal decay further away from the focal point.

## 8.1.2 Results and discussion

Biological sample under intense femtosecond illumination has an intrinsic nonlinear signal - the second and third harmonic generation of incident light. The second harmonic signal is generated in the sample which does not have an inversion center, hence having a non-vanishing second order nonlinear susceptibility. For instance, it is very efficiently generated in periodic structures such as collagen molecules. The third harmonic is generated in any sample without symmetry constraints. As the second and third harmonic microscopy are intensity dependent to second and third order, respectively, the signal is collected from a short region in focal plane, hence the method provides intrinsic confocal  $Z$ -sectioning [108].

The used sample was pollen grain, which is a standard sample for microscope and laser system testing in confocal as well as multiphoton microscopy [110].

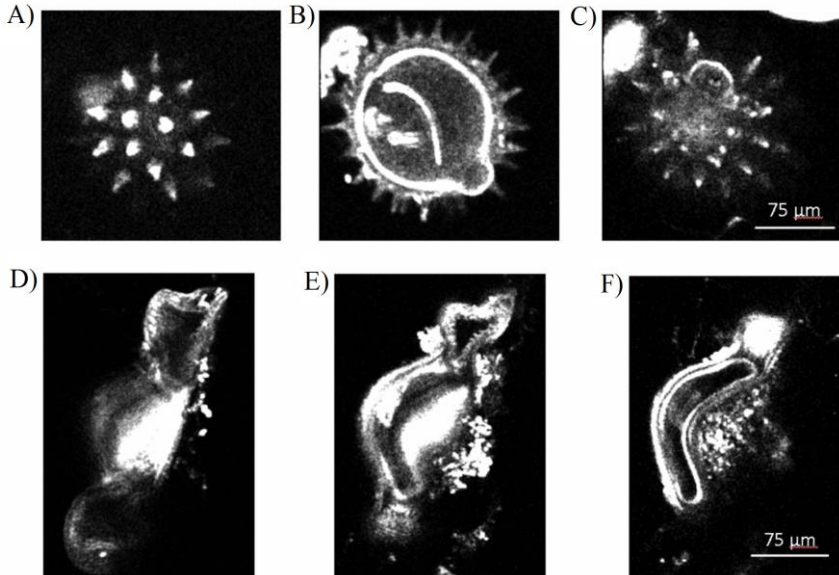


Fig. 8.4. Third harmonic generation images of the pollen grain sample #1 A) to C) and sample #2 D) to F). Sequences of images A) to C) and D) to F) are captured with a step size of 60  $\mu\text{m}$  in the z axis direction. The OPO is tuned to 1235 nm wavelength, the third harmonic is generated and detected at 412 nm.

Fig. 8.4 shows the 3<sup>rd</sup> harmonic generation images recorded with 1235 nm excitation wavelength and collecting light at 412 nm. The three Z sections of two samples are shown in sequences of a) to c) and d) to f).

The incident power to the sample is about 20 mW, 170 x 170 pixels are mapped with 450  $\mu\text{s}$  pixel dwell time resulting in 13 seconds acquisition time. Quite long pixel dwell time is needed, because the third harmonic generation process is not efficient. The point spread function indicated that Z-sectioning should resolve 2  $\mu\text{m}$  steps sections, but the images show features from deeper layers, most probably resulting from pollen autofluorescence and image artifacts resulting from long integration time. One advantage of third harmonic generation microscopy – long

wavelengths are less scattered deep in the tissue, in this experiment up to 120  $\mu\text{m}$  depth was imaged.

After the harmonic generation microscopy experiments, two-photon microscopy experiments were carried out. The optical parametric oscillator wavelength was tuned to match the double wavelength of a single photon absorption peak wavelength. Each dye was imaged serially with a procedure of: a fluorophore absorption matching 2 photon wavelength set to a new value; fluorescence filter changed; image raster scanned. In post procession of the images, all dye colour channels were stitched to produce a single image.

In order to test the optical parametric oscillator, standard samples are imaged:

- „FluoCells“ sample slide #2: bovine pulmonary artery endothelial cells. Antibody BODIPY FL (absorption at  $\lambda=505$  nm, emission at  $\lambda=513$  nm) is labelling microtubules, dye Texas Red-X (absorption  $\lambda=591$  nm, emission  $\lambda=608$  nm) stains F-actin, dye DAPI (absorption at  $\lambda=358$  nm, emission at  $\lambda=461$  nm) stains cell nuclei.
- „FluoCells“ sample slide #1: bovine pulmonary artery endothelial cells. Dye MitoTracker Red CMXR (absorption at  $\lambda=579$  nm, emission at  $\lambda=599$  nm) stains mitochondria, dye Alexa Fluor 488 (absorption at  $\lambda=505$  nm, emission at  $\lambda=512$  nm) stains F-actin, dye DAPI (absorption at  $\lambda=358$  nm, emissin at  $\lambda=461$  nm) stains cell nuclei.
- „FluoCells“ sample slide #6: muntjac skin fibroblast. Dye Alexa Fluor 488 (absorption at  $\lambda=505$  nm, emission at  $\lambda=512$  nm) stains F-actin, dye Alexa Fluor 555 (absorption at  $\lambda=556$  nm, emission at  $\lambda=573$  nm) stains mitochondria, iodide TO-PRO-3 (absorption  $\lambda=642$  nm, emission  $\lambda= 661$  nm) stains cell nuclei.

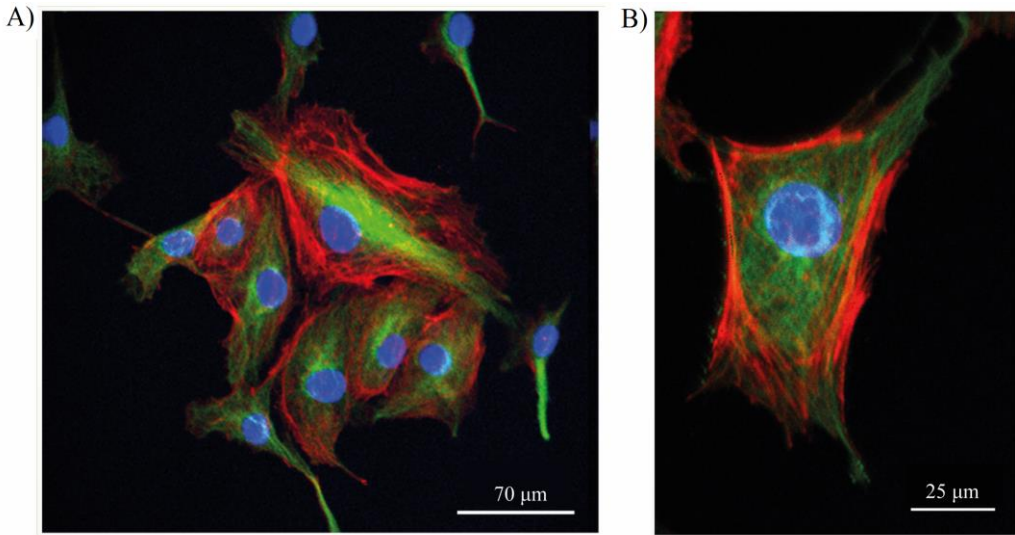


Fig. 8.5. A) and B): Two-photon microscopy image of bovine pulmonary artery endothelial cells, slide #2. Blue dye stains nuclei (excitation wavelength of 760 nm), green dye stains F-actin (excitation wavelength of 1182 nm), red dye stains microtubules (excitation wavelength of 1010 nm).

In Fig. 8.5A, three sequential imaging steps are made with different excitation wavelengths: 760 nm, 1010nm and 1182 nm. The emission filters are manually changed for all three color channel measurements. The image consists of 400 x 400 pixels with 17 μs pixel dwell time and 2.5 s acquisition time for one colour channel. Fig. 8.5B shows zoomed out single cell body from the same sample. Each color was imaged with 5-10 mW in the sample plane.

In picture of Fig. 8.6A, 500 x 500 pixels are imaged with 130 μs pixel dwell time with a total scan time of 38 seconds, the excitation is done with the wavelengths of 760 nm, 1010 nm and 1160 nm. The Fig. 8.6B image is imaged with 990 nm and 1110 nm wavelengths, the laser system did not have enough output power for two photon iodide labelled nuclei imaging at 1280 nm. 340 x 480 pixels are imaged with a pixel dwell time of 93 μs, the total acquisition time is 15 seconds. Each color was imaged with 5-10 mW in the sample plane.

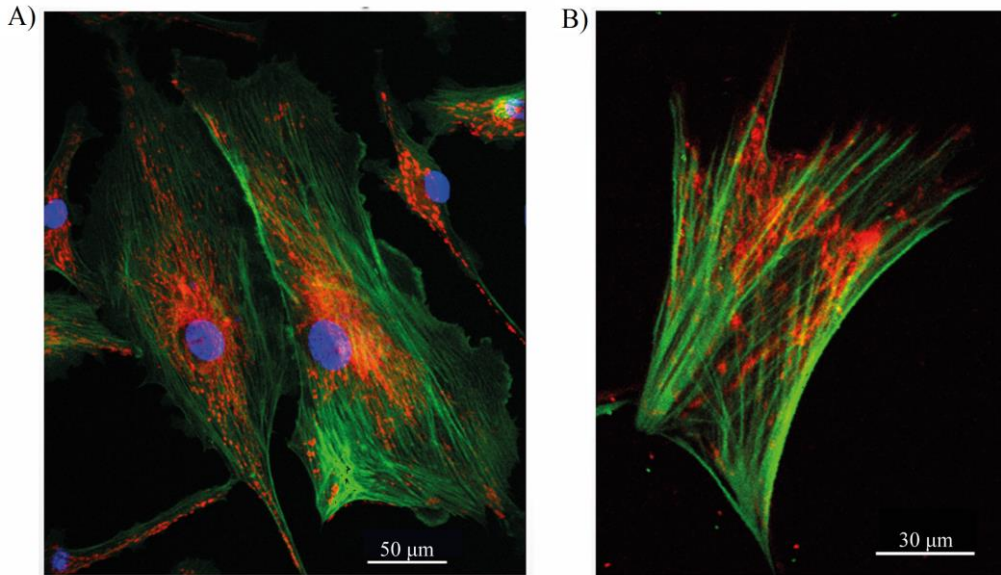


Fig. 8.6. A) Two-photon microscopy image of bovine pulmonary artery endothelial cells, slide #1. Blue dye stains nuclei (excitation wavelength of 760 nm), green dye stains F-actin (excitation wavelength of 1010 nm), red dye stains mitochondria (excitation wavelength of 1160 nm). B) Two-photon microscopy image of muntjac skin fibroblast, slide #6. Green dye stains F-actin (excitation wavelength of 990 nm), red dye stains mitochondria (excitation wavelength of 1110 nm).

### 8.1.3 Summary

The assembled prototype of optical parametric oscillator was shown to nonlinearly excite fluorophores in dyed biological samples and generate intrinsic third harmonic generation signal. The wavelength tunability was exploited for a number of serial excitation experiments, enabling imaging of different cell organelles. The pulse energy and pulse duration proved to be sufficient for such *in vitro* “slow” imaging conditions. The beam quality at the sample plane was inspected and proved to be near diffraction limited.

## 8.2 Two-photon polymerization

Optical physics background of multiphoton polymerization is similar to the two photon microscopy – both depend on multiphoton absorption of the fluorescent probe or photoinitiator. However, the material aspect of the technology is different. The great majority of work in multiphoton fabrication has involved using light to render a material insoluble in the exposed region. A material whose solubility decreases on exposure to light is known as a negative-tone photoresist. Negative-tone photoresists are used widely in photolithography and many of these materials can be adapted to multiphoton fabrication. By exposure of light, negative-tone photoresists which consist of soluble organic monomers, get cross-linked and therefore made insoluble. In two photon fabrication this cross-linking typically follows the light-induced generation of either free radicals or cations. A crucial component of such materials is therefore the photoactive substance which is known as a photoinitiator in radical polymerization. A number of factors affect the efficiency with which two-photon excitation can initiate photopolymerization:

- Cross section of the initiator.
- Initiator quantum efficiency for creation of radicals.
- Initiation reaction velocity.

The resolution of voxel created during two-photon polymerization is dependent on threshold dose for insolubility. This threshold allows for the creation of features with sizes that are smaller than the diffraction limit [111].

In this chapter the two-photon polymerization (2PP) experiments were carried out in Vilnius University Laser Research Center, Vilnius, Lithuania, in the lab of prof. Roaldas Gadonas, using the prototype of the portable OPO assembled at Light Conversion.

The results of this chapter were presented in conference paper CO1.

### 8.2.1 Experimental procedures

Femtosecond light source used in the experiment is a system comprised of two separately pumped optical parametric oscillators (OPOs). The pump source has 10 W of average power and 76 MHz repetition rate, the OPOs are pumped with second harmonic of the fundamental, total 5 W of second harmonic power is available and its total power is split equally to pump both OPOs simultaneously. The output wavelength is tuned in the range of  $\sim 700$ - $960$  nm for first channel and  $\sim 950$ - $1300$  nm for the second channel. The output power tuning curve is given in Fig. 8.7. The output pulse duration ranges from  $\sim 90$  to 140 fs with the maximum achievable power reaching  $\sim 450$  mW. Both channels are available for simultaneous use, but during the experimental procedure, only one channel was used at a time to cover the entire required wavelength range.

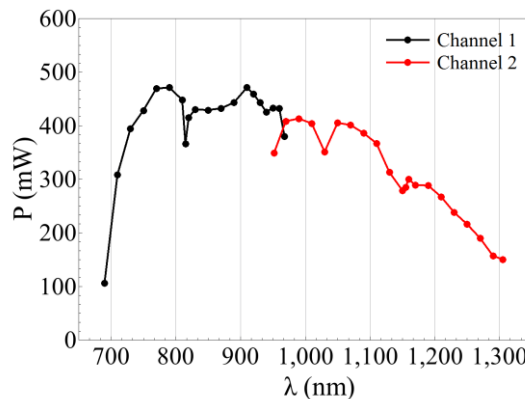


Fig. 8.7. Output power dependence on wavelength of two independently tunable OPOs system.

During this study, the effects of wavelength dependence on the 2PP threshold was investigated. The photo-polymerization and photo-damage threshold dependence at the wavelength range of 700-1250 nm was measured by using OPO tunable radiation. Thresholds of hybrid organic-inorganic photosensitive SZ2080 resist sensitized with a commonly used BIS photoinitiator at 0.5%, 2%, 6% and without the photoinitiator were investigated.

Energy  $E_p$  was calculated at the focal spot from directly measured energy at the entrance of the objective lens and the known transmission of the objective. The cumulative energy irradiation dose  $D_c$  is calculated by the fluence  $F_p$  per pulse factored by the number of pulses  $N_f$ . Fluence is defined as  $I_p = E_p / (A_p)$ , where  $A_p$  is spot area at the focal plane, defined as  $A_p = \pi (d_f / 2)^2 = \pi (0.66 \lambda / NA)^2$ , where  $d_f$  is the spot size and  $NA$  is a numerical aperture of an objective lens  $NA \sim 1.4$ . The number of pulses accumulated per focal spot diameter is  $N_f = t_{dw} f$ , where  $f$  is pulse repetition rate and  $t_{dw} = d_f / v_{sc}$ , where  $v_{sc} = 100 \mu\text{m/s}$  is the scan speed. The cumulative irradiation dose is calculated in a following manner [113],[114]:

$$D_c = \frac{E_p t_{dw}}{f A_p}. \quad (8.2)$$

A judgement on the polymerization threshold was carried out by the onset of a recognizable light scattering of the inscribed linear pattern during optical observation under 630 nm LED light illumination.

## 8.2.2 Results and discussion

An important factor of 3D polymerization is the 3D localization of light occurring via tight focusing. An increase of the skin depth, where much of the energy is absorbed via avalanche ionization of electrons, leads to a decrease of the required dose for polymerization. Energy density absorbed by free electrons (which are seeded by multiphoton absorption) is defined as:

$$W_{abs}(\lambda) \sim \frac{n_e(\lambda)}{n_{cr}(\lambda)} \sim n_e(\lambda) \lambda^2 \sim \lambda^4, \quad (8.3)$$

where  $n_e(\lambda)$  is the electron density and  $n_{cr}(\lambda)$  is the critical plasma density. The critical plasma density has a wavelength dependence of  $n_{cr}(\lambda) \sim \lambda^{-2}$ . The electron density is created by the avalanche and multi-photon processes. If only avalanche processes are considered, the electron density is proportional to an electron

oscillation energy  $E_{osc}$  in an incident electric field. The electron gains more energy if the period of oscillations (or wavelength  $\lambda$ ) is increased, therefore, it has a dependence of  $E_{osc} \sim \lambda^2$ . This means that the energy absorbed by electrons scales as  $W_{abs}(\lambda) \sim \lambda^4$ , as shown in the equation (8.3) [112].

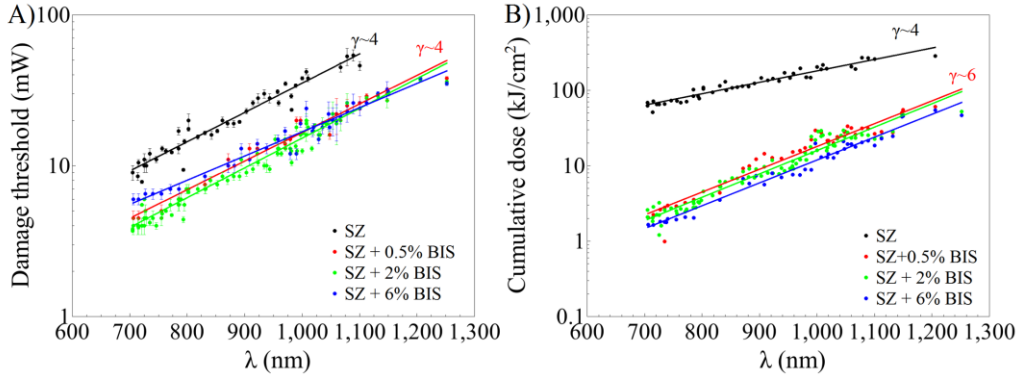


Fig. 8.8. A) Material damage threshold dependence on wavelength. B) Cumulative dose dependence on wavelength. In both panels three different initiator concentrations were investigated and pure SZ without initiator.

The assumption that the electron generation effect is dominated by avalanche and not by multiphoton ionization is based on the earlier research by Malinauskas et al. [113]. They showed that thermal accumulation becomes important when the cooling time of the irradiated spot  $t_c = d_f^2 / D_T$  (where  $D_T$  is temperature diffusivity constant for polymers  $D_T \sim 10^{-3} \text{ cm}^2/\text{s}$ ) is comparable with the time separation between consequent pulses  $1/f$ . For  $NA \sim 1.4$  focusing  $t_c \sim 2 \mu\text{s}$  and the time separation between OPO output pulses is 13 ns. Therefore, the thermal effects are dominating and these favour avalanche ionization. Avalanche ionization is favoured because in polymers, local increase in temperature narrows an effective bandgap  $E_g$ , which increases avalanche ionization, proportional to  $1/E_g$ . The electron recombination rate is also faster at elevated temperatures and creates a positive feedback for polymerization by transferring energy into heat and a local temperature increase [114].

Experimentally, the polymerization threshold is determined by light scattering of simultaneously incident LED light, it is the volume of the polymerized area which is indirectly observed and evaluated as a polymerization threshold volume. Therefore, the evaluation of the dose or threshold required for polymerization at different wavelengths is identical to the evaluation of polymerized sample volume which scatters the same amount of light. From the absorbed energy density equation (8.3):

$$V_{threshold} \sim \frac{E_{abs}}{\lambda^4}, \quad (8.4)$$

where  $E_{abs}$  is the absorbed energy, which is directly related to the experimentally measurable cumulative dose. This equation shows that incident dose (absorbed energy) should scale as  $D \sim \lambda^4$  in order for the polymerized volume threshold to be constant for all the wavelengths. This allows explaining the experimental results of cumulative dose and damage threshold shown in Fig. 8.8A and Fig. 8.8B.

As is evident from Fig. 8.8A and Fig. 8.8B, inclusion of the photoinitiator leads to the deviation from the aforementioned law, most probably because of the additional effect of multiphoton ionization, as the BIS linear absorption spectrum is more red-shifted than the SZ material. Absorption maximum of SZ is centered at 340 nm, whereas the absorption maximum of BIS is centered at 520 nm [114, 115].

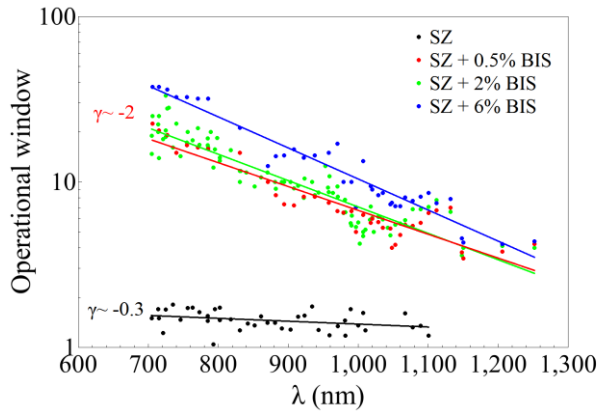


Fig. 8.9. Operational window dependence on wavelength. Three different initiator concentrations were investigated and pure SZ without initiator.

The window of fabrication (shown in Fig. 8.9) is calculated as a ratio of the polymerization threshold to the damage threshold. It is evident that the inclusion of the photoinitiator leads to a wider fabrication window and correspondingly safer regime which is further away from the dielectric breakdown.

### 8.2.3 Summary

The wavelength tunability of the femtosecond optical parametric oscillator was exploited in the two-photon polymerization experiment.

The results indicate that polymerization process is governed by electrons gaining energy through the avalanche ionization. This result could originate from high repetition rate of the pulses leading to strong thermal effects. Further investigation with lower repetition rate pulses needs to be carried out to confirm this hypothesis.

### **8.3 Two-photon optogenetics**

Optogenetics is a novel biological technique that involves the use of light to control the neurons, genetically modified to express light-sensitive ion channels. Therefore, it is named after the combination of two techniques – optics and genetics. In all-optical optogenetics, light of different wavelengths is simultaneously used to modulate and to readout the activity of neurons. Neuronal control is achieved using optogenetic actuators like channelrhodopsin and readout of neural activity is achieved with a help of optogenetic sensors for various specific indicators such as calcium or membrane voltage. In order to readout whole region of neuronal activity and selectively stimulate only the preferred neurons, actuators and sensors should have well separated excitation spectra. The most effective sensors are based on the fluorophore switching from dark state to fluorescent state, which are triggered by an influx of calcium ions as the neuron fires through the neural network [116]. One of the most efficient calcium sensitive genetically encoded calcium indicator GCaMP absorbs blue light and fluoresces in green, with 2-photon excitation it becomes excitable at ~900-1000 nm range [117]. Using the femtosecond lasers and two-photon excitation lead to various benefits compared to the single photon illumination, such as single-cell specificity, improved axial resolution, increased penetration depth and less phototoxicity of NIR light.

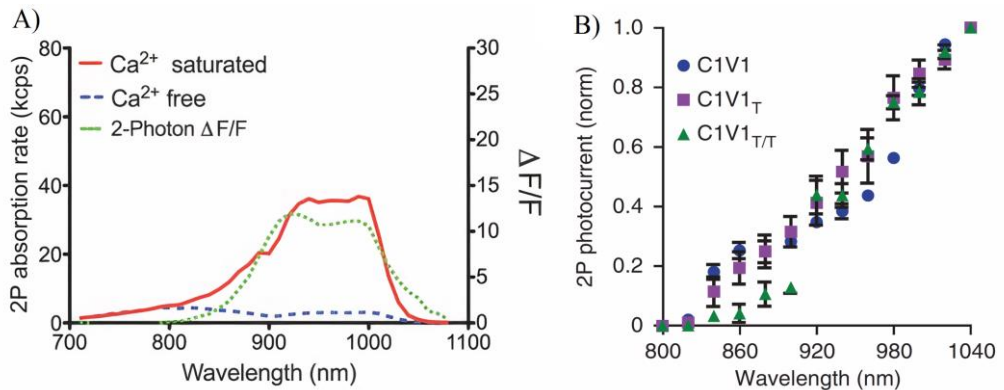


Fig 8.10. A) Genetically encoded calcium indicator GCaMP two-photon absorption rate dependence on wavelength when it bounds to calcium ions (Ca<sup>2+</sup> saturated) and when the calcium ions are absent (Ca<sup>2+</sup> free). The ratio of saturated to free states shows relative change of fluorescence  $\Delta F/F$ , shown in right pane. Adapted from [117]. B) C1V1 opsin generated photocurrent dependence on wavelength absorbed nonlinearly with two photons. A family of genetical modifications of the C1V1 is shown with varying current rise time properties. Adapted from [118].

A two photon absorption spectrum of GCAMP is shown in Fig 8.10A. As is evident from the figure, the saturated state fluorescence is  $\sim 15$  stronger than the dark state, leading to a deterministic excitable fluorescence signal whenever neuron is firing.

The most effective actuators for neuronal control are light gated ion channels. The most popular being blue light activated channelrhodopsin (ChR1) which serves as sensory photoreceptor in green algae. Expressed in cells in other organisms, they allow light to modulate the electrical excitability, calcium influx and other cellular processes. However, being sensitive to blue light, the ChR1 absorption spectrum overlaps with blue light excitable neural activity sensors, such as GCAMP. This leads to a crosstalk of excitation and readout and artifacts in the experiment. To prevent this, red light activated actuators could be used, such as a newly developed C1V1 opsin actuator [118]. The 2 photon light induced current dependence on wavelength of the C1V1 opsin actuator is given in Fig 8.10B. Efficiency of 2 photon

generated current is quite low, therefore large pixel dwell times or multiple covered ion channels are needed to reliably bring the neurons expressing ChR2 to action potential threshold [119]. Therefore, higher femtosecond pulse intensity is required compared to the two photon excitation of the GCAMP sensor. Having a laser source with two spectral outputs would enable selective and independent excitation of both sensor and actuator. This could be enabled with GCAMP sensor with one wavelength of ~900 nm and a C1V1 actuator with another wavelength of >1040 nm where GCAMP remains at its dark state.

Femtosecond optical parametric oscillators are well suited for such application because of their wavelength tuning characteristics and high repetition rate which translates to speed with which the neural activity can be monitored [120]. Having two separately tunable channels allows one to tune the wavelengths for maximum signal and minimum crosstalk compromise. One of the motivations of this comparative study was showing that simultaneous cross-talk free optogenetics excitation and readout could be achieved with a compact one box double - OPO system compared to the bulky state of the art double Ti: Sapphire and single OPO setup.

In this chapter, two-photon optogenetics experiments were carried out in University of Mainz, Mainz, Germany, in the lab of prof. Albrecht Stroh, using the prototype of optical parametric oscillator system assembled at Light Conversion.

The results of this chapter were presented in conference paper CO2.

### **8.3.1 Experimental procedures**

All experiments were carried out in adult female and male C57/BL6 mice. Sensor GCAMP6 was co-expressed with opsin C1V1. Adult mice were anesthetized and virus injections were made during a craniotomy. Viral constructs were delivered through a small durotomy by a glass pipette at a depth of 200  $\mu\text{m}$  targeting brain layer II/III and at the 600  $\mu\text{m}$  depth targeting brain layer V/VI. The skull was exposed to fix the head-holder on the mouse's head and close a skull opening with a chronic 4 mm diameter window.

Live animal imaging was performed four weeks post injection to ensure sufficient co-expression of GCAMP6 and C1V1. The animals were anesthetized before imaging and this led to recording of a persistent brain state. The custom made

2-photon microscope setup was equipped with a resonant scanner for fast full field scanning up to 35 Hz for the GCaMP neural activity imaging with 920 nm laser line. The imaging plane was 250  $\mu\text{m}$  below the cortical surface and the field of view was 466 x 466  $\mu\text{m}$  using Zeiss W-Plan-Apochromatic 20x ( $NA = 1$ ) objective. The maximum applied laser power at the image plane was 30 mW at 920 nm.

C1V1 stimulation was performed using a separate galvo scanner pair for a  $>1040$  nm laser line. Regions of interests were stimulated (20 x 20  $\mu\text{m}$ ) to cover whole neuron cell body. Stimulation was delivered every 10 seconds and was applied for a duration of 68 ms with a pixel dwell time of 6  $\mu\text{s}$ . The maximum applied laser power at the image plane was 200 mW at 1100 nm.

All-optical two-photon interrogations can be achieved by using different light sources and system configurations. Schemes of a custom made 2-P microscope using different configurations and light sources are presented in Fig. 8.11. In all configurations, the imaging wavelength is guided to a resonant scanner for full-field imaging of GCaMP6f at 920 nm and the stimulation wavelength at longer infrared is guided to a temporally uncoupled galvo-scanner for independent optogenetic control. The current state of the art solution of wavelength extension is shown in Fig. 8.11A, it is using Ti: Sapphire output to pump the OPO, which delivers a broader wavelength range for the opsin excitation (1100 nm – 1400 nm). The Ti: Sapphire could be tuned to 920 nm and part of this light could be used to pump the OPO which emits 1100 nm, but the efficiency of the Ti: Sapphire and the OPO drop with this wavelength configuration [121]. Fig. 8.11B shows another configuration having two separate Ti: Sapphire lasers. Two independent laser lines solve this problem as the OPO could be pumped at the peak of the tuning curve of Ti: Sapphire at 760 nm. Another Ti: Sapphire laser could be tuned to 920 nm to enable GCaMP imaging. The main drawbacks of this configuration are price and complexity. The double OPO setup is presented as a third configuration in the Fig. 8.11C, it could be an alternative to double Ti: Sapphire + OPO system.

## Applications of the assembled OPO

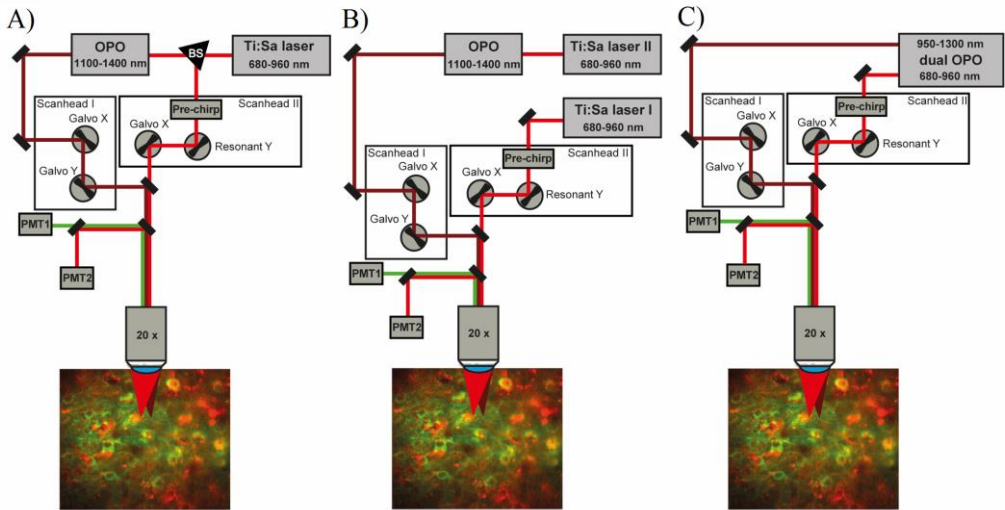


Fig. 8.11. A) Microscope set up based on one Ti:Sapphire laser which is tuned to 920 nm for GCaMP imaging and part of this light is used for pumping the OPO to extend the wavelength for opsin activation. B) Microscope set up based on two independent Ti: Sapphire lasers, one is dedicated to GcaMP6f-imaging and the other one is pumping the OPO. C) Microscope setup with a dual OPO laser, which is delivering two independently tunable laser beams. Imaging wavelengths (680 – 960 nm) are guided to a resonant scanner and stimulation wavelengths (950 – 1300 nm) are guided to a separate galvano scanner. PMT: Photomultiplier Tube, BS: Beamsplitter.

In this investigation, both double Ti: Sapphire + OPO (Fig. 8.11B) and double OPO (Fig. 8.11C) approaches were used for imaging experiments.

The Fig. 8.11B setup used Ti: Sapphire laser Chameleon Ultra II pumping Compact OPO (Coherent, CA, USA) which delivered 1100-1400 nm range wavelengths and a second independent Ti: Sapphire laser Chameleon Ultra II. The OPO emitted up to 700 mW at 1100 nm, the second independent Ti: Sa laser emitted up to 2 W of output power at 920 nm. The laser sources operated at 80 MHz repetition rate and around 140 fs pulse duration.

Femtosecond light source used in the setup of Fig. 8.11C is a system comprised of two separately pumped optical parametric oscillators (OPOs) produced

by Light Conversion. The pump source had 16 W of output average power and 76 MHz repetition rate, the OPOs are pumped with second harmonic of the fundamental, total 8 W of second harmonic power is available and its total power is split equally to pump both OPOs simultaneously. The output wavelength is tuned in the range of  $\sim 700$ -960 nm for the first channel and  $\sim 950$ -1300 nm for the second channel. The output pulse duration ranges from  $\sim 100$  fs to 160 fs. Both channels are available for simultaneous use. The power tuning curve of the double OPO source is given in Fig. 8.12.

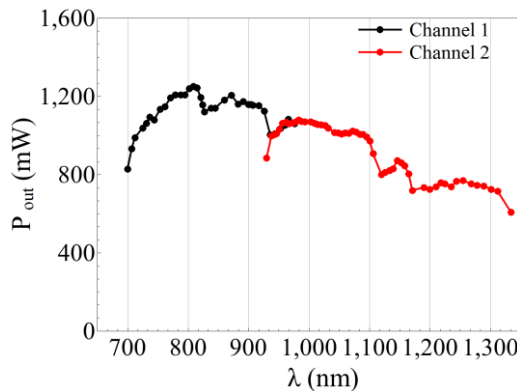


Fig. 8.12. Output power dependence on wavelength of two independently tunable OPOs system.

### 8.3.2 Results and discussion

For an all-optical experiment with minimal cross-talk, it is essential to spectrally separate imaging and stimulation. Therefore, the spectral window needs to be defined allowing for the reliable detection of functional calcium transients. *In vivo* imaging of GCaMP6f-expressing neurons was performed at different wavelengths of the same field of view, in layer II/III of visual cortex in lightly anesthetized mice (Fig. 8.13). The *in vivo* results replicate the two photon absorption spectrum given in Fig 8.10A, showing that imaging wavelength has to be set at approximately 920 nm. Investigation of imaging at the longer wavelengths than 920

nm was limited by the dichroic mirror reflection curve. Despite that, the longer imaging wavelengths should not be used in order not to excite the opsin at its short wavelength absorption tail as shown in Fig 8.10B. Even though the neurons could be visually detected at below 900 nm, spontaneous activity could be hardly observed at these wavelengths. One motivation of this study was trying to image GCAMP with 860 nm wavelength, as this would lead to high enough Ti: Sapphire output power to simultaneously pump the OPO and provide part of the 860 nm light for imaging (as shown in Fig. 8.11A). The results show that a wavelength longer than ~900 nm is needed for GCAMP imaging and a single Ti: Sapphire system is not optimal for simultaneous OPO pumping and imaging.

Applications of the assembled OPO

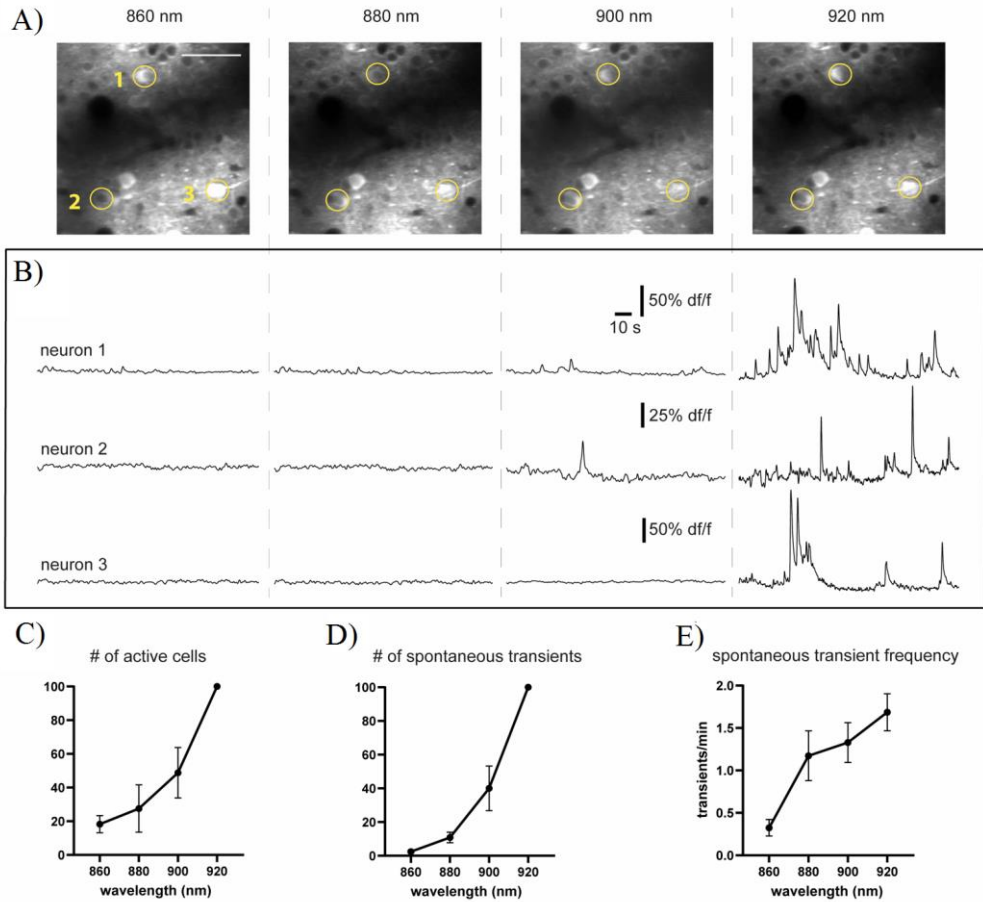


Fig. 8.13. Functional calcium transients can only be detected in a rather narrow spectral window. A) 2-P imaging of GCaMP6f expressing neurons at four different Ti: Sapphire wavelengths (860, 880, 900, 920 nm) in layer II/III of mouse visual cortex. The very same three neurons (yellow circles) are depicted at every wavelength. Scale bar 50  $\mu\text{m}$ . B) Corresponding calcium traces of depicted neurons (measured by electrophysiology with inserted high resistance probe). C) Normalized number of active cells at different wavelengths. D) Normalized total number of calcium transients at tested wavelengths. E) Average transient frequencies at different wavelengths.

As the lower edge of the spectral range for all-optical experiments was now set to 920 nm due to the functional limitations of GCaMP6f discussed before, a light

source was to be used, which flexibly delivered longer wavelengths for cross-talk free optogenetic modulations. Previous work on all-optical physiology used fixed-wavelength Ytterbium lasers typically between 1040 and 1080 nm for the 2-P excitation of opsins [120 - 123]. Investigation was made to probe whether longer wavelength might both reduce cross-talk and improve efficacy. The cross-talk stems from the GCaMP absorption tail at longer wavelengths ~1020 nm as shown in Fig 8.10A. The spectral windows were defined for artifact-free all-optical interrogations by testing different wavelengths for stimulation. To ensure that photostimulation artifacts were not due to mistakenly attributed calcium transients, a stimulation was made on mice which were lacking C1V1 expression and solely expressed GCaMP6f (Fig. 8.14A). Notably, significant artifact in the calcium trace was observed when applying stimulation wavelength at 1020 nm and the power of 40 mW used commonly for all-optical experiments (Fig. 8.14B). Increasing power levels to 80 mW which increases the efficacy of stimulation led to even more pronounced artifacts.

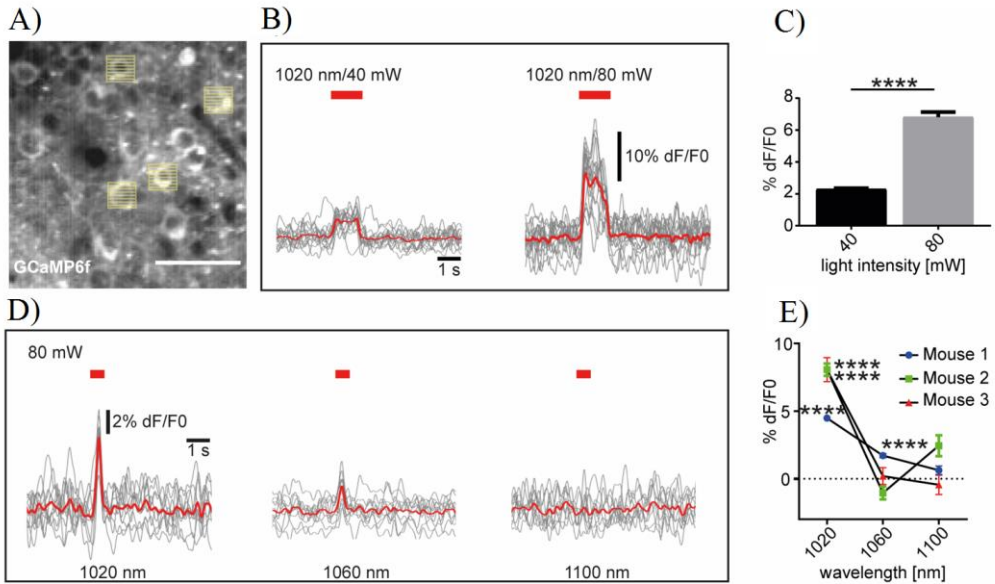


Fig. 8.14. Stimulation artifact of 2-P excitation is wavelength-dependent and absent above 1100 nm. A) *In vivo* 2-P calcium imaging of GCaMP6f expressing neurons in layer II/III of mouse visual cortex and simultaneous raster scan stimulations of selected cells at different wavelengths and light intensities. Scale bar 50  $\mu$ m. B) Average artifact (red line,  $n = 10$  artifacts, single trials are depicted in grey) in a calcium trace of selected neurons upon 40 and 80 mW raster scan stimulations at 1020 nm. The amplitude of the artifact is increasing with increasing stimulation light power. C) Quantification of artifact amplitude at 40 and 80 mW. D) Averaged artifact (red lines,  $n = 10$  artifacts, single trials are depicted in grey) upon 2-P raster scan stimulations (80 mW) at varying stimulation wavelengths (1020 nm, 1060 nm and 1100 nm). E) Quantification of artifact amplitude at different stimulation (80 mW) wavelengths. Average artifact amplitudes are decreasing with increasing wavelength. At 1100 nm no above-noise artifact is observable.

Finally, *in vivo* experiments were conducted in animals expressing high and functional levels of both opsin CIV1 and indicator GCaMP6f in the lightly anesthetized mouse. First, only GCaMP6f imaging was performed. The anesthetic level was set in a way that persistent, desynchronized population activity could be observed. In persistent brain state, cell-specific interventions were made on

genetically-defined CIV1-expressing neurons using 2-P based optogenetic stimulation. Sequential stimulations were carried out of individual cells at the artifact-free wavelength of 1100 nm using aforementioned raster scans while simultaneously imaging GCaMP6f-fluorescence at 920 nm (Fig. 8.15A). The task to be tackled was, whether increasing stimulation wavelength beyond 1100 nm, not being possible with standard Ti: Sapphire or Ytterbium lasers, will lead to an increased efficacy. The early studies in the field revealed a linear increase in photocurrents (shown in Fig 8.10B), until the technical limit of 1040 nm [118]. Surprisingly, it was found that a further increase of the stimulation wavelength from 1100 up to 1300 nm did not yield a significant increase in the rate of evoked calcium transients (Fig. 8.15C) as well as no significant increase in the fraction of responding cells (Fig. 8.15D). However, increasing stimulation power from rather low values ranging at 40 or 80 mW up to values ranging at 120 or 210 mW significantly increased the rate of evoked transient 2-3 fold.

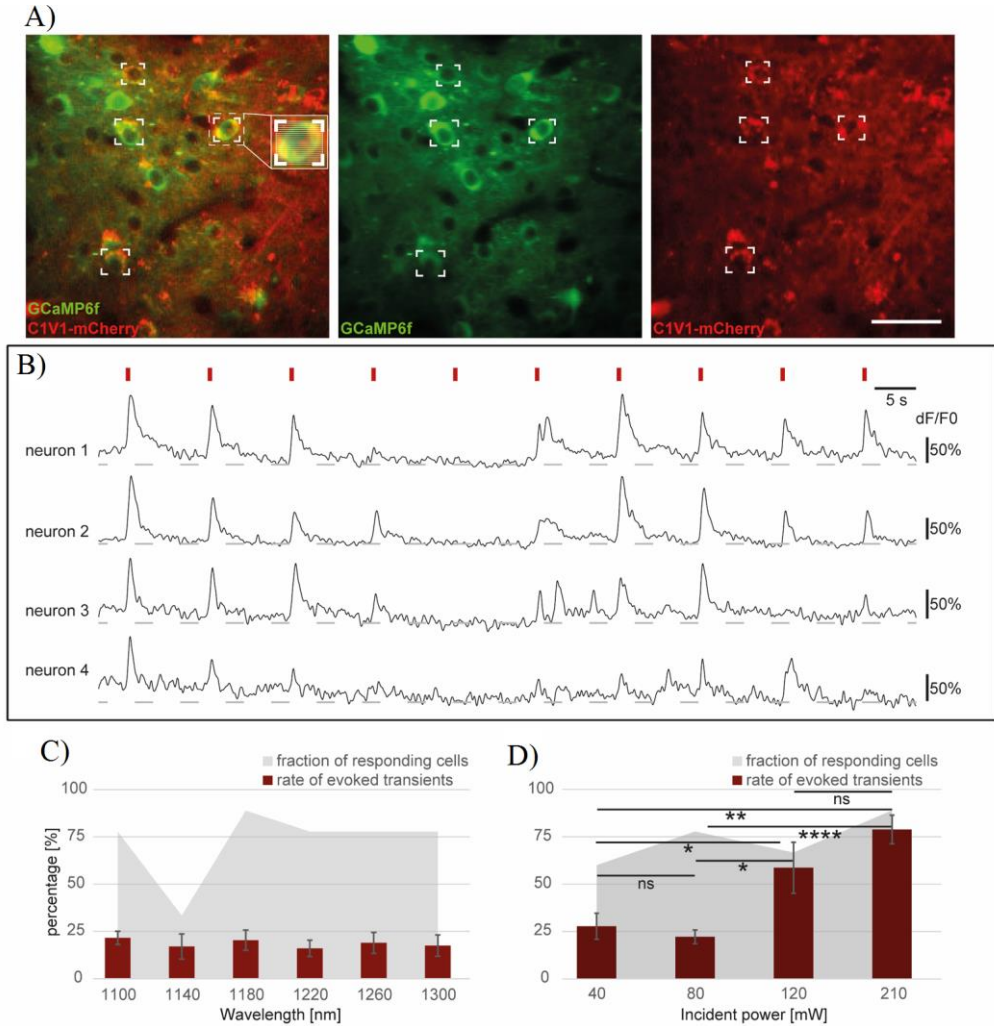


Fig. 8.15. 1100 nm represents the optimal wavelength for effective and cross-talk-free optogenetic control. A) All-optical control of individual GCaMP6f (green) / C1V1<sub>T/T</sub> (red) co-expressing neurons in layer II/III of mouse visual cortex. A 2-P stimulation at 1100 nm of GCaMP6f/C1V1<sub>T/T</sub> co-expressing neurons in layer II/III of mouse visual cortex. Depiction of raster scan patterns as described above. Four individual neurons can be targeted for sequential photostimulation. Scale bar 50  $\mu$ m. B) GCaMP6f calcium transients of four co-expressing neurons upon ten stimulation trials with 1100 nm stimulation wavelength and 200 mW of average power (time of stimulation indicated by red marker, the stimulation period is 10 seconds). C) Average rate of evoked transients (red bars) at varying wavelengths (1100 nm - 1300 nm) at 80 mW. Grey shadow indicates the fraction of responding cells. n = 9

neurons, 5-10 trials each, 1 mouse. D) Same as in C but varying light intensities (40, 80, 120 and 210 mW) at 1100 nm. Same color coding as in C, n = 23 neurons, 5-10 trials each, 3 mice.

### **8.3.3 Summary**

The wavelength tunability of the femtosecond optical parametric oscillator was exploited in the two-photon optogenetics experiment.

Neuronal activity indicated by GCAMP indicator can only be observed with two photon excitation wavelengths larger than ~900 nm. This precludes using common Ti: Sapphire pumping OPO systems because of decrease of Ti: Sapphire power at this wavelength.

GCAMP can be excited with two photons at longer wavelengths and the opsin stimulation wavelength range of 1020-1080 nm leads to imaging artifacts. Wavelengths longer than 1100 nm should be used for such a GCAMP indicator and C1V1 opsin pair, excitation of C1V1 in the wavelength range of 1100-1300 nm was demonstrated.

Simultaneous all-optical readout and excitation was demonstrated; the experiment was shown to be free from cross-talk between stimulation and recording, and did not produce read out artifacts.

## 9 Conclusions

1. Phase-mismatched optical parametric oscillation crystal leads to effective nonlinearity the magnitude and sign of which is adjustable; this can be used to compensate or amplify the self-phase modulation effects inherent in high power femtosecond optical parametric oscillators with both signs of intracavity dispersion. (Chapter 4)
2. A second SHG signal crystal inserted in OPO cavity can be phase-mismatched to induce tunable negative nonlinearity for positive group delay dispersion compensation and allow soliton formation, leading to the pulses of high spectro-temporal quality. (Chapter 5)
3. Large phase shifts produced by cascaded quadratic nonlinearity lead to generation of higher order solitons, exhibiting oscillatory behaviour unless perturbed by higher orders of nonlinear dispersion. (Chapter 6)
4. Optical parametric oscillator crystal cascaded nonlinearity induces nonlinear spatial focusing or defocusing which is strong enough to drive the resonator out of the stability if operating the device near a linear stability limit. (Chapter 7)
5. The prototype of double-beam femtosecond optical parametric oscillator wavelength tunable in the ranges of 700 – 950 nm and 950 - 1300 nm has been successfully applied in nonlinear harmonic generation, two-photon microscopy, optogenetics and two-photon polymerization. Its versatility and feature set stand out as a unique in the field of high-repetition rate tunable lasers. (Chapter 8)

## 10 References

- [1] J. A. Giordmaine and R. C. Miller, "Tunable coherent parametric oscillation in  $\text{LiNbO}_3$  at optical frequencies", *Phys. Rev. Lett.* **14** (24), 973 (1965).
- [2] Majid Ebrahimzadeh, Gordon Robertson, and Malcolm H. Dunn, "Efficient ultraviolet  $\text{LiB}_3\text{O}_5$  optical parametric oscillator", *Optics Letters* **16**, (10), 767-769 (1991).
- [3] C. Gu, M. Hu, J. Fan, Y. Song, B. Liu, L. Chai, C. Wang, D. T. Reid, "High power tunable femtosecond ultraviolet laser source based on an Yb-fiber-laser pumped optical parametric oscillator", *Optics Express* **23**, (5), 6181-6186 (2015).
- [4] Toomas H. Allik, Suresh Chandra, David M. Rines, Peter G. Schunemann, J. Andrew Hutchinson, and Richard Utano, "Tunable 7–12- $\mu\text{m}$  optical parametric oscillator using a Cr,Er:YSGG laser to pump CdSe and ZnGeP<sub>2</sub> crystals", *Optics Letters* **22**, (9), 596-599 (1997).
- [5] S. Chaitanya Kumar, J. Krauth, A. Steinmann, K. T. Zawilski, P. G. Schunemann, H. Giessen, M. Ebrahim-Zadeh, "High-power femtosecond mid-infrared optical parametric oscillator at 7  $\mu\text{m}$  in CdSiP<sub>2</sub>", *Optics Letters* **40**, (7), 1398-1401 (2015).
- [6] M. E. Klein, D.-H. Lee, J.-P. Meyn, K.-J. Boller, and R. Wallenstein, „Singly resonant continuous-wave optical parametric oscillator pumped by a diode laser“, *Optics Letters* **24**, (16) 1142-1144 (1999).
- [7] G. K. Samanta, M. Ebrahim-Zadeh, „Continuous-wave singly-resonant optical parametric oscillator with resonant wave coupling“, *Optics Express* **16**, (10), 6883-6888 (2008).
- [8] S. Chaitanya Kumar, A. Esteban-Martin, T. Ideguchi, M. Yan, S. Holzner, T.W. Hänsch, N. Picqué and M. Ebrahim-Zadeh, „Few-cycle, Broadband, Mid-infrared Optical Parametric Oscillator Pumped by a 20-fs Ti:sapphire Laser“, *Laser and Photonics Reviews* **8** (5), 86-91 (2014).
- [9] R. A. McCracken, D. T. Reid, „Few-cycle near infrared pulses from a degenerate 1 GHz optical parametric oscillator“, *Optics Letters* **40**, (17) 4102-4105 (2015).
- [10] Mark S. Webb, Peter F. Moulton, Jeffrey J. Kasinski, Ralph L. Burnham, Gabe Loiacono, and Richard Stolzenberger, „High-average-power  $\text{KTiOAsO}_4$  optical parametric oscillator“, *Optics Letters* **23**, (15) 1161-1163 (1998).
- [11] Gabriel Amiard Hudebine, Eric Freysz, "Tunable and chirp free femtosecond signal pulses generated by a PPLN OPO pumped by Ytterbium fiber laser

- chirped pulses," Proc. SPIE 10902, Nonlinear Frequency Generation and Conversion: Materials and Devices XVIII, 109020M (4 March 2019)
- [12] T. Petersen, J. D. Zuegel, J. Bromage, "High-average-power, 2- $\mu$ m femtosecond optical parametric oscillator synchronously pumped by a thin-disk, mode-locked laser", Optics Express **25**, (8), 8840-8844 (2017).
- [13] T. Lang, T. Binhammer, S. Rausch, G. Palmer, M. Emons, M. Schultze, A. Harth, U. Morgner, "High power ultra-widely tuneable femtosecond pulses from a non-collinear optical parametric oscillator (NOPO)" Optics Express **20**, (2), 912-917 (2012).
- [14] Tobias P. Lamour, Derryck T. Reid, "650-nJ pulses from a cavity-dumped Yb: fibre pumped ultrafast optical parametric oscillator" Optics Express **19**, (18), 912-917 (2011).
- [15] Shai Yefet and Avi Pe'er, "A Review of Cavity Design for Kerr Lens Mode-Locked Solid-State Lasers", Appl. Sci. **3**, 694-724 (2013).
- [16] O. Pronin, J. Brons, *Kerr-lens mode-locked High power thin-disk oscillators*, IntechOpen (2018).
- [17] O. Pronin, J. Brons, C. Grasse, V. Pervak, G. Boehm, M. C. Amann, V. L. Kalashnikov, A. Apolonski, F. Krausz, "High-power 200 fs Kerr-lens mode-locked Yb:YAG thin-disk oscillator" Optics Letters **36**, (24), 4746-4748 (2011).
- [18] R. DeSalvo, D. J. Hagan, M. Sheik-Bahae, G. Stegeman, W. E. Van Stryland, "Self-focusing and self-defocusing by cascaded second-order effects in KTP," Optics Letters **17**, (1) 28-30 (1992).
- [19] G. M. Gale, M. Cavallari, and F. Hache, "Femtosecond visible optical parametric oscillator," J. Opt. Soc. Am. B **15**, (2) 702-714 (1998).
- [20] V. G. Dmitriev, G. G. Gurzadyan D. N. Nukogosyan, *Handbook of Nonlinear Optical Crystals*, Springer (1999).
- [21] R. Šuminas, G. Tamošauskas, G. Valiulis, A. Dubietis, "Spatiotemporal light bullets and supercontinuum generation in  $\beta$ -BBO crystal with competing quadratic and cubic nonlinearities," Optics Letters **41**, (9) 2097-2100 (2016).
- [22] R. Šuminas, G. Tamošauskas, V. Jukna, A. Couairon, A. Dubietis, "Second-order cascading-assisted filamentation and controllable supercontinuum generation in birefringent crystals," Optics Express **25**, (6) 6746-6756 (2017).
- [23] R. Laenen, H. Graener, A. Laubereau, "Evidence for chirp reversal and self-compression in a femtosecond optical parametric oscillator," J. Opt. Soc. Am. B **8**, (5) 1085-1088 (1991).

- [24] I. Ricciardi, S. Mosca, M. Parisi, F. Leo, T. Hansson, M. Erkintalo, P. Maddaloni, P. D. Natale, S. Wabnitz, M. D. Rosa, "Optical Frequency Combs in Quadratically Nonlinear Resonators", *Micromachines* 11 (2), 230, (2020).
- [25] J. Szabados, D. N. Puzyrev, Y. Minet, L. Reis, K. Buse, A. Villois, D. V. Skryabin, I. Breunig, "Frequency comb generation via cascaded second-order nonlinearities in microresonators", *Phys. Rev. Lett.* 124 (20), 203902, (2020).
- [26] A. S. Kwligy, A. Lind, D. D. Hickstein, D. R. Carlson, H. Timmers, N. Nader, F. C. Cruz, G. Ycas, S. B. Papp, S. A. Diddams, "Mid-infrared frequency comb generation via cascaded quadratic nonlinearities in quasi-phase-matched waveguides", *Optics Letters* 23 (8), 1678-1681, (2018).
- [27] J. Bewersdorf, S.W. Hell, "Picosecond pulsed two-photon imaging with repetition rates of 200 and 400 MHz", *Journal of Microscopy*, 191 (1), 28-38,(1998)
- [28] V. Ulvila, C. R. Phillips, L. Halonen, M. Vainio, "Frequency comb generation by a continuous-wave pumped optical parametric oscillator based on cascading quadratic nonlinearities", *Optics Letters* 38 (21), 4281-4284 (2013).
- [29] F. Saltarelli, A. Diebold, I. J. Graumann, C. R. Phillips, U. Keller, "Self-phase modulation cancellation in a high-power ultrafast thin-disk laser oscillator", *Optica* 5 (12), 1603-1606 (2018).
- [30] A. S. Mayer, C. R. Phillips, U. Keller, "Watt-level 10-gigahertz solid-state laser enabled by self-defocusing nonlinearities in an aperiodically poled crystal", *Nature Communications* 8, 1673 (2017).
- [31] L. J. Qian, X. Liu, F. W. Wise, "Femtosecond Kerr-lens mode locking with negative nonlinear phase shifts", *Optics Letters* 24 (3), 166-168 (1999).
- [32] G. Cerullo, S. D. Silvestri, A. Monguzzi, D. Segala, V. Magni, "Self-starting mode locking of a cw Nd:YAG laser using cascaded second-order nonlinearities", *Optics Letters* 20 (7), 746-748 (1995).
- [33] S. T. Lin, C. H. Huang "Effects of nonlinear phase in cascaded mode-locked Nd: YVO4 laser", *Optics Express* 27, (2) 504-511 (2019).
- [34] Luise Beichert, Yuliya Binhammer, José Ricardo Andrade, Ann-Kathrin Kniggendorf, Bernhard Roth, Uwe Morgner, "Non-collinear Optical Parametric Oscillator for Video Rate Stimulated Raman Spectroscopy of Microplastics", *Conference on Lasers and Electro-Optics Europe and European Quantum Electronics Conference, Munich, Germany* (2019).
- [35] H. Yoshida, H. Fujita, M. Nakatsuka, M. Yoshimura, T. Sasaki, T. Kamimura, K. Yoshida, "Dependences of Laser-Induced Bulk Damage Threshold and Crack Patterns in Several Nonlinear Crystals on Irradiation Direction", *Japanese Journal of Applied Physics* 45, (2A), 766-769 (2006).

- [36] T. Petersen, J. D. Zuegel, J. Bromage, “Thermal effects in an ultrafast BiB3O6 optical parametric oscillator at high average powers”, *Applied Optics* 56, (24), 6923-6929 (2017).
- [37] D. Nikogosyan, *Nonlinear Optical Crystals: A Complete Survey*, Springer, (2015).
- [38] M. S. Bahae, D. C. Hutchings, D. J. Hagan, E. W. Van Stryland “Dispersion of Bound Electronic Nonlinear Refraction in Solids”, *IEEE Journal of Quantum Electronics* 27, (6), 1296-1309 (1991).
- [39] Christian R. Rosberg, Francis H. Bennet, Dragomir N. Neshev, Per D. Rasmussen, Ole Bang, Wieslaw Krolikowski, Anders Bjarklev, and Yuri S. Kivshar, “Tunable diffraction and self-defocusing in liquid-filled photonic crystal fibers”, *Optics Express* 15, (19), 12145-12150.
- [40] Volker Andresen, Stephanie Alexander, Wolfgang-Moritz Heupel, Markus Hirschberg, Robert M. Hoffman, Peter Friedl, “Infrared multiphoton microscopy: subcellular-resolved deep tissue imaging”, *Current Opinion in Biotechnology* 20, (1), 54-62 (2009).
- [41] Robert W. Boyd, *Nonlinear Optics*, Academic Press (2008).
- [42] Jean- Claude Diels, Wolfgang Rudolph, *Ultrashort Laser Pulse Phenomena*, Academic Press (2006).
- [43] Y.R. Shen, *The Principles of Nonlinear Optics*, Wiley (1984).
- [44] R. Trebino, *Frequency-Resolved Optical Gating: The measurement of Ultrashort Laser Pulses*, Kluwer Academic Publishers (2002).
- [45] G. I. Stegeman, D. J. Hagan, “ $\chi^2$  cascading phenomena and their applications to all-optical signal processing, mode-locking, pulse compression and solitons,” *Optical and Quantum Electronics* 28, 1691-1740 (1996).
- [46] J. Wei, *Nonlinear Super-Resolution Nano-Optics and Applications*, Springer (2015).
- [47] G. P. Agrawal, *Nonlinear Fiber Optics*, 5th Edition, Academic Press, (2013).
- [48] William H. Press, Saul T. Teukolsky, *Numerical Recipes in C* Cambridge University Press (2002).
- [49] D. Lowenthal, “CW periodically poled LiNbO optical parametric oscillator model with strong idler absorption”, *Journal of Quantum Electronics*, **34** (8), 1356-1366 (1998).
- [50] A.V. Smith, R. J. Gehr, “Numerical models of broad-bandwidth nanosecond optical parametric oscillators”, *J. Opt. Soc. Am. B*, 14 (4), 609-619, (1999).
- [51] V. Pyragaitė, *Kompiuterinė lazerių fizika*, Vilniaus Universitetas (2013).

## References

- [52] A.V. Smith, W. J. Alford, T. D. Raymond, M. S. Bowers, “Comparison of a numerical model with measured performance of a seeded, nanosecond KTP optical parametric oscillator”, *J. Opt. Soc. Am. B*, 12 (11), 2253-2267, (1995).
- [53] J. Seres, J. Hebling, “Nonstationary theory of synchronously pumped femtosecond optical parametric oscillators”, *J. Opt. Soc. Am. B*, 17 (5), 741-750, (2000).
- [54] T. C. Poon, T. Kim, *Engineering Optics with Matlab*, World Scientific (2006).
- [55] T. C. Poon, P. P. Banerjee, *Contemporary Optical Image Processing with Matlab*, Elsevier (2001).
- [56] V. Magni, G. Cerullo, S. De Silvestri, “High-accuracy fast Hankel transform for optical beam propagation”, *J. Opt. Soc. Am. A*, 9 (11), 2031- 2033, (1992).
- [57] G. Arisholm, “Quantum noise initiation and macroscopic fluctuations in optical parametric oscillators”, *J. Opt. Soc. Am. B*, 16 (1), 117-127, (1999).
- [58] S. M. Saltiel, A. A. Sukhorukov, Y. S. Kivshar, “Multistep parametric processes in nonlinear optics”, *Progress in Optics*, 47, 1-73 (2005).
- [59] M. Bache, *Cascaded nonlinearities for ultrafast nonlinear optical science and applications*, DTU- Department of Photonics Engineering (2017).
- [60] L. Kador, “Kramers–Kronig relations in nonlinear optics”, *Appl. Phys. Lett.*, 66, 2938 (1995).
- [61] C. Conti, S. Trillo, G. Gallot, G. M. Gale, P. Di Trapani, J. Kilius, A. Bramati, S. Minardi, W. Chinaglia, G. Valiulis, “Effective lensing effects in parametric frequency conversion,” *J. Opt. Soc. Am. B* 19, (4) 852-859 (2002).
- [62] P. Di Trapani, A. Bramati, S. Minardi, W. Chinaglia, C. Conti, S. Trillo, J. Kilius, G. Valiulis, “Focusing versus defocusing nonlinearities due to parametric wave mixing”, *Phys. Rev. Lett.*, 87 (18), 2001.
- [63] P. K. Jakobsen, *Introduction to the method of multiple scales*, arXiv.org (2013).
- [64] Ali Hasan Nayfeh, *Introduction to Perturbation Techniques*, John Wiley and Sons (1993).
- [65] F. Saltarelli, A. Diebold, I. J. Graumann, C. R. Phillips, U. Keller, “Self-phase modulation cancellation in a high-power ultrafast thin-disk laser oscillator”, *Optica* 5 (12), 1603-1606 (2018).
- [66] J. T. Verdeyen, *Laser Electronics*, Prentice Hall (1995).
- [67] A. E. Siegman, *Lasers*, University Science Books, (1986).
- [68] D. Metcalf, P. de Giovanni, J. Zachorowski, M. Leduc, “Laser resonators containing self-focusing elements,” *Applied Optics* 26, (21) 4508-4517 (1987).
- [69] V. Magni, “ Resonators for solid-state lasers with large-volume fundamental mode and high alignment stability”, *Applied Optics* 25 (1), 107-117 (1986)

- [70] I. Stasevicius, M. Vengris are preparing a manuscript to be called “Cascaded nonlinearity induced spatial domain effects in high power femtosecond optical parametric oscillator”.
- [71] J. E. Hellstrom, S. Bjurshagen, V. Pasiskevicius, “Laser performance and thermal lensing in high-power diode-pumped Yb: KGW with athermal orientation”, *Appl. Phys. B* 83, 55-59 (2006).
- [72] M. Ghotbi, A. Esteban - Martin, M. Ebrahim - Zadeh, “BiB3O6 femtosecond optical parametric oscillator”, *Optics Letters* 31, (21) 3128-3130 (2006).
- [73] J. Vengelis, I. Stasevicius, K. Stankeviciute, V. Jarutis, R. Grigonis, M. Vengris, V. Sirutkaitis, “Characteristics of optical parametric oscillators synchronously pumped by second harmonic of femtosecond Yb:KGW laser”, *Optics Communications* 338, 277-287 (2015).
- [74] K. Ivanauskiene, I. Stasevicius, M. Vengris, V. Sirutkaitis, “Pulse-to-pulse instabilities in synchronously pumped femtosecond optical parametric oscillator”, *J. Opt. Soc. Am. B* 36 (1), 131-139 (2019).
- [75] I. Stasevicius, M. Vengris are preparing a manuscript to be called “Exploiting optical nonlinearities for group delay dispersion compensation in femtosecond optical parametric oscillator”.
- [76] I. Stasevicius, G. Martynaitis, M. Vengris, “Cascaded nonlinearities in high-power femtosecond optical parametric oscillator”, *J. Opt. Soc. Am. B* 37 (3), 721-729 (2020).
- [77] D. T. Reid, J. M. Dudley, M. Ebrahimzadeh, W. Sibbett, “Soliton formation in a femtosecond optical parametric oscillator,” *Optics Letters* 19, (11) 825-827 (1994).
- [78] M. Jankowski, A. Marandi, C.R. Phillips, R. Hamerly, K. A. Ingold, R. L. Byer, M. M. Fejer, “Temporal simultons in optical parametric oscillators,” *Phys. Rev. Lett.* 120, 053904 (2018).
- [79] X. Zhang, H. Giessen, “Four-wave mixing based on cascaded second-order nonlinear processes in a femtosecond optical parametric oscillator operating near degeneracy,” *Appl. Phys. B*, 79, 441-447 (2004).
- [80] T. Gottschalll, J. Limpert, A. Tunnermann, “Ultra-short pulse fiber optical parametric oscillator,” *Optics Letters* 42, (17) 3423-3426 (2017).
- [81] G. Tsigaridas, M. Fakis, I. Polyzos, P. Persephonis, V. Giannetas, “Z-scan technique through beam radius measurement,” *Appl. Phys. B* 76, (1) 83-86 (2003).
- [82] F. Hache, A. Zeboulon, G. Gallot, G. M. Gale, “Cascaded second-order effects in the femtosecond regime in  $\beta$ -barium borate: self-compression in a visible

- femtosecond optical parametric oscillator,” *Optics letters* 20, (14) 1556-1558 (1995).
- [83] J. Hebling, E. J. Mayer, J. Kuhl, R. Szipocs, “Chirped-mirror dispersion-compensated femtosecond optical parametric oscillator”, *Optics Letters* 20, (8), 919-921 (1995).
- [84] H. Guo, B. Zhou, M. Steinert, F. Setzpfandt, T. Pertsch, H. Chung, Y. Chen, M. Bache, “Supercontinuum generation in quadratic nonlinear waveguides without quasi-phase matching”, *Optics Letters* 40 (4), 629- 632 (2015).
- [85] O. E. Martinez, “Matrix Formalism for Dispersive Laser Cavities”, *IEEE Journal of Quantum Electronics* 25, (3) 296-300 (1989).
- [86] S. Zahedpour, J. K. Wahlstrand, and H. M. Milchberg, “Measurement of the nonlinear refractive index of air constituents at mid-infrared wavelengths”, *Optics Letters* 40, (24) 5794-5797 (2015).
- [87] J. Bromage, J. Rothhardt, S. Hadrich, C. Dorrer, C. Jocher, S. Demmler, J. Limpert, A. Tunnermann, J. D. Zuegel “Analysis and suppression of parasitic processes in noncollinear optical parametric amplifiers”, *Optics Express* 19, (18) 16979-16808 (2011).
- [88] M. Bache, O. Bang, W. Krolikowski, J. Moses, F. W. Wise, “Limits to compression with cascaded quadratic soliton compressors,” *Optics Express* 16, (5) 3273-3287 (2008).
- [89] Kent. C. Burr, C. L. Tang, Mark. A. Arbore, Martin M. Fejer, ”Broadly tunable mid-infrared femtosecond optical parametric oscillator using all-solid-state-pumped periodically poled lithium niobate”, *Optics letters* 22, (19) 1458-1460 (1997).
- [90] D. Descloux, C. Laporte, J. B. Dherbecourt, J. M. Melkonian, M. Raybaut, C. Drag, A. Godard, “Spectrotemporal dynamics of a picosecond OPO based on chirped quasi-phase-matching”, *Optics Letters* 40 (2), 280-283 (2015).
- [91] C. Ning, Z. Zhang, “Multi-soliton formation in femtosecond degenerate optical parametric oscillators”, *Optics Letters* 45 (3), 734-737 (2020).
- [92] C. F. O’ Donnell, S. C. Kumar, T. Paoletta, M. Ebrahim-Zadeh, “Widely tunable femtosecond soliton generation in a fiber-feedback optical parametric oscillator”, *Optica* 7 (5), 426-433 (2020).
- [93] V. Tamuliene, M. Vengris, V. Sirutkaitis, “Theoretical investigation of pulse-to-pulse instabilities in synchronously pumped femtosecond optical parametric oscillator”, *J. Opt. Soc. Am. B* 37 (2), 473-477 (2020).
- [94] A. V. Husakou, J. Herrmann, “Supercontinuum Generation of Higher-Order Solitons by Fission in Photonic Crystal Fibers”, *Phys. Rev. Lett.* 87 (20), 203901 (2001).

## References

- [95] M. Bache, O. Bang, B. B. Zhou, J. Moses, F. W. Wise, "Optical Cherenkov radiation in ultrafast cascaded second-harmonic generation," *Physical Review A* 82, (6) 06386 (2010).
- [96] D. V. Skryabin, A. V. Yulin, "Theory of generation of new frequencies by mixing of solitons and dispersive waves in optical fibers," *Physical Review E* 72, 016619 (2005).
- [97] Y. Chen, W. Lu, Y. Xia, X. Chen, "Dependences of the group velocity for femtosecond pulses in MgO-doped PPLN crystal", *Optics Express* 19, (6) 5213-5218 (2011).
- [98] B. Zhou, J. Ma, J. Wang, P. Yuan, G. Xie, L. Qian, "Ultrafast group-velocity control via cascaded quadratic nonlinearities in optical parametric amplification", *Optics Letters* 43 (15), 3790-3793 (2018).
- [99] J. Moses, F. Wise, "Controllable Self-Steepening of Ultrashort Pulses in Quadratic Nonlinear Media", *Phys. Rev. Lett.* 97 (7), 073903, (2006).
- [100] F. Ilday, K. Beckwitt, Y. Chen, H. Lim, F. Wise "Controllable Raman-like nonlinearities from non-stationary cascaded quadratic processes", *J. Opt. Soc. Am. B* 21 (2), 376-383 (2004).
- [101] F. Salin, P. Grangier, G. Roger, A. Brun, "Observation of High-Order Solitons Directly Produced by a Femtosecond Ring Laser", *Phys. Rev. Lett.* 56 (11), 1132-1136, (1986).
- [102] T. Lang, A. Harth, J. Matyschok, T. Binhammer, M. Schultze, U. Morgner "Impact of temporal, spatial and cascaded effects of pulse formation in ultra-broadband parametric amplifiers", *Optics Express*, 21, (1) 949 (2013).
- [103] G. Arisholm, R. Paschotta, T. Sudmeyer, "Limits of the power scalability of high-gain optical parametric amplifiers", *J. Opt. Soc. Am. B* 21, (3) 578-589 (2004).
- [104] G. Cerullo, S. De Silvestri, V. Magni, L. Pallaro, "Resonators for Kerr-lens mode-locked femtosecond Ti:sapphire lasers", *Optics Letters* 19, (11) 807-809 (1994).
- [105] A. Penzkofer, M. Wittmann, M. Lorenz, E. Siegert, S. Macnamara "Kerr lens effects in a folded-cavity four-mirror linear resonator", *Optical and Quantum Electronics* 28, 423-442 (1996).
- [106] M. Seidel, J. Brons, G. Arisholm, K. Fritsch, V. Pervak, O. Pronin, "Efficient High-Power Ultrashort Pulse compression in Self-Defocusing Bulk Media", *Scientific Reports* 7, 1410 (2017).
- [107] R. Hamerly, A. Marandi, M. Jankowski, M. M. Fejer, Y. Yamamoto, H. Mabuchi, "Reduced models and design principles for half-harmonic generation

- in synchronously-pumped optical parametric oscillators”, *Phys. Rev. A* 94, 063809 (2016).
- [108] P. J. Campagnola, H. A. Clark, W. A. Mohler, A. Lewis, L. M. Loew, “Second-harmonic imaging microscopy of living cells”, *Journal of Biomedical Optics*, 6 (3), 277-286 (2001).
- [109] C. Xu and W. W. Webb, “Measurement of two-photon excitation cross sections of molecular fluorophores with data from 690 to 1050 nm”, *J. Opt. Soc. Am. B*. 13 (3), 481-491 (1996).
- [110] S. Vitha, V.M. Bryant, A. Zwa, A. Holzenburg, “3D Confocal imaging of pollen”, 15, 622-623, *Microscopy and Microanalysis* (2009).
- [111] T. Baldacchini, *Three-Dimensional Microfabrication Using Two-Photon Polymerization*, Elsevier (2016).
- [112] E. G. Gamaly, *Femtosecond laser-matter interactions: theory, experiments, and applications*, Pan Stanford Publishing (2011).
- [113] M. Malinauskas, P. Danilevičius, S. Juodkazis, „Three dimensional micro-/nano-structuring via direct write polymerization with picosecond laser pulses”, *Optics Express* 19, (6) 5602-5610 (2011).
- [114] M. Malinauskas, A. Zukauskas, G. Bickaускаite, R. Gadonas, S. Juodkazis, “Mechanisms of three-dimensional structuring of photo-polymers by tightly focussed femtosecond laser pulses”, *Opt. Express* 18, 10209-10221 (2010).
- [115] V. Purlys, D. Gailevicius, I. Stasevicius, V. Voiciuk, S. Vaisiunas, R. Gadonas, „Influence of Laser Wavelength for Direct Laser Writing Thresholds“, „CLEO“, Germany, Munich, 2017.
- [116] A. Stroh, *Optogenetics: A Roadmap*, Springer (2018).
- [117] J. Akerboom, T.W. Chen, T. J. Wardill et al., “Optimization of a GCaMP calcium indicator for neural activity imaging”, *the Journal of Neuroscience*, 32 (40), 13819-13840 (2012).
- [118] R. Prakash, O. Yizhar, B. Grewe et al. “Two-photon optogenetic toolbox for fast inhibition, excitation and bistable modulation”, *Nature Methods*, 9 (12), 1171-1183 (2012).
- [119] Christopher A. Baker, Yishai M. Elyada, Andres Parra, M. Mc Lean Bolton, „Cellular resolution circuit mapping with temporal-focused excitaton of soma-targeted channelrhodopsin“, *eLife*, 5, e14193 (2016).
- [120] W. Yang, L. C. Reid, Y. Bando, D. S. Peterka, R. Yuste, “Simultaneous two-photon imaging and two-photon optogenetics of cortical circuits in three dimensions”, *eLife*, e32617 (2018).

## References

- [121] T. R. Steele, D. C. Gerstenberger, A. Drobshoff, R. W. Wallace, “Broadly tunable high-power operation of an all-solid-state titanium-doped sapphire laser system”, *Optics Letters*, 16 (6), 399-401 (1991).
- [122] Packer, A.M., et al., Simultaneous all-optical manipulation and recording of neural circuit activity with cellular resolution in vivo. *Nat Methods*, 2015. 12(2): p. 140-6.
- [123] Carrillo-Reid, L., et al., Controlling Visually Guided Behavior by Holographic Recalling of Cortical Ensembles. *Cell*, 2019. 178(2): p. 447-457 e5.
- [124] Ting Fu, Isabelle Arnoux, Jan Döring, Hirofumi Watari, Ignas Stasevicius, Albrecht Stroh, „Navigating the translational roadblock: Towards highly specific and effective all-optical interrogations of neural circuits“, „FENS 2020 Virtual Forum“, online conference (2020).

## 11 List of publications

1) K. Stankevičiūtė, I. Pipinytė, I. Stasevičius, J. Vengelis, G. Valiulis, R. Grigonis, M. Vengris, M. Bardauskas, L. Giniunas, O. Balachninaite, R.C. Eckardt, V. Sirutkaitis, „Femtosecond optical parametric oscillators synchronously pumped by Yb:KGW oscillator“, Lithuanian Journal of Physics, Vol. 53, No. 1, 41–56 (2013).

2) J. Vengelis, I. Stasevičius, K. Stankevičiūtė, V. Jarutis, R. Grigonis, M. Vengris, V. Sirutkaitis, „Characteristics of optical parametric oscillators synchronously pumped by second harmonic of femtosecond Yb:KGW laser“, Optics Communications 338, 277–287 (2015).

3) K. Ivanauskiene, I. Stasevicius, M. Vengris, V. Sirutkaitis, “Pulse-to-pulse instabilities in synchronously pumped femtosecond optical parametric oscillator”, J. Opt. Soc. Am. B 36 (1), 131-139 (2019).

4). I. Stasevicius, G. Martynaitis, M. Vengris, “Cascaded nonlinearities in high-power femtosecond optical parametric oscillator”, J. Opt. Soc. Am. B 37 (3), 721-729 (2020).

5). I. Stasevicius, M. Vengris, „Exploiting optical nonlinearities for group delay dispersion compensation in femtosecond optical parametric oscillators“, Optics Express 28 (18), 26122-26136 (2020).

6). I. Stasevicius, M. Vengris, „Controlled soliton formation in femtosecond optical parametric oscillator with positive group delay dispersion“, J. Opt. Soc. Am. B 37 (10), 2956-2967 (2020).

7). I. Stasevicius, M. Vengris, „Cascaded nonlinearity induced spatial domain effects in high power femtosecond optical parametric oscillator“, to be published in Optics Express (2020).

## NOTES

Vilnius University Press

9 Saulėtekio Ave., Building III, LT-10222 Vilnius

Email: [info@leidykla.vu.lt](mailto:info@leidykla.vu.lt), [www.leidykla.vu.lt](http://www.leidykla.vu.lt)

Print run copies: 20